5-18-2015

Development and Characterization of a GaAs nipi Superlattice Solar Cell

Michael A. Slocum

Recommended Citation
Slocum, Michael A., "Development and Characterization of a GaAs nipi Superlattice Solar Cell" (2015). Thesis. Rochester Institute of Technology. Accessed from

R·I·T

Development and Characterization of a GaAs *nipi* Superlattice Solar Cell

by

Michael A. Slocum

A dissertation submitted in partial fulfillment of the requirements
for the degree of Doctorate of Philosophy in Microsystems Engineering

Microsystems Engineering Program
Kate Gleason College of Engineering

Rochester Institute of Technology
Rochester, New York
May 18, 2015

Development and Characterization of a GaAs *nipi* Superlattice Solar Cell
by
Michael A. Slocum

Committee Approval:

We, the undersigned committee members, certify that we have advised and/or supervised the candidate on the work described in this dissertation. We further certify that we have reviewed the dissertation manuscript and approve it in partial fulfillment of the requirements of the degree of Doctorate of Philosophy in Microsystems Engineering.

Dr. Seth M. Hubbard Date
Associate Professor, Physics
Deceased 01/2015

Dr. David V. Forbes Date
Assistant Research Professor, Sustainability

Dr. Stefan F. Preble Date
Associate Professor, Microsystems Engineering

Dr. James E. Moon Date
Associate Professor, Electrical and Microelectronic Engineering

Dr. Geoffrey A. Landis Date
Research Scientist, NASA Glenn Research Center

Certified by:

Dr. Stefan F. Preble Date
Director, Microsystems Engineering Program

Dr. Edward Hensel Date
Associate Dean, Graduate Studies and Research

ABSTRACT

Kate Gleason College of Engineering
Rochester Institute of Technology

Degree: Doctorate of Philosophy **Program:** Microsystems Engineering
Author's Name: Michael A. Slocum
Advisor's Name: Dr. Seth M. Hubbard
Dissertation Title: Development and Characterization of a GaAs *nipi* Superlattice Solar Cell

Doping superlattices have been explored theoretically and some historic work has used these superlattices to form *nipi* solar cells with alternating *n-type*, intrinsic, *p-type*, intrinsic layers. Multiple purposes exist for evaluating *nipi* solar cells, which include radiation hardness, an electronically adjustable absorption edge, use with nanostructures, and the possibility of an intermediate band solar cell (IBSC). The primary motivation for this work is to develop the *nipi* solar cell for evaluation as an IBSC, while also evaluating the radiation tolerance of the design for potential use in space applications. This has been completed through a theoretical and experimental analysis of *nipi* superlattice layers, and an extensive evaluation of the fabrication and growth processes required to achieve a high efficiency solar cell. As a part of this evaluation an improved model for *nipi* diodes and solar cells has been developed. Also a novel process for fabricating *nipi* solar cells through epitaxial regrowth and diffused junctions has been developed, where record efficiencies for *nipi* solar cells have been measured for devices fabricated via epitaxial regrowth at 12.5%. An understanding of the effect of adding quantum dots (QD) into a *nipi* superlattice has been obtained. Finally a greater understanding of the intrinsic radiation hardness of the *nipi* design has been achieved and possible methods to improve it have been evaluated. The techniques and processes developed here have the possibility to be used to further the understanding of *nipi* devices, and lead to the potential development of an IBSC with a QD-*nipi* design.

In memory of Dr. David Forbes, a great mentor, colleague, and friend.

You are tremendously missed Dave!

Acknowledgments

I would like to thank my advisor Dr. Seth Hubbard for his support and encouragement through the process of my PhD, and allowing me numerous opportunities to grow and develop my skills and abilities working as a part of his laboratory.

A special thanks is also required for my committee member David Forbes who had spent many hours talking with me about MOCVD growth and has taught me more than any other individual during this process, he will be greatly missed. I would also like to thank the remainder of my committee members, Stefan Preble, James Moon and Geoffrey Landis for their contributions and encouragement. Each of the classes I had taken with Drs. Preble and Moon has left an enduring mark.

I am entirely indebted to my wife Caroline who has continuously supported me through this process. She has been so understanding as I have continuously traveled to Cleveland for NASA trips, and a few conferences a year, happily taking on all the household and family responsibilities in my absence. I would also like to thank my children, Joy and Zeke, although they are too young to understand where I disappear to every day at 7:30 they are a constant source of optimism and hope.

I would also like to thank:

- My parents, Don and Gail for supporting me, even if they had no idea what I was doing
- <Dr. Steve Polly> for his ability to always entertain a question and provide viable input
- Zac Bittner for his constant enthusiasm to tackle any problem, even if it doesn't need to
- Staffan Hellström for his help and guidance with anything related to simulations
- Nichole Hoven for being a continual help with growth at NASA, and being willing to put up with my nonsense
- Dr. Christopher Bailey for being an inspiration and mentor as I started my PhD process
- The NASA crew who help and support the MOCVD reactor and keep life entertaining in Cleveland; Jay, Eric, Anna, Barb and Mike
- Members of the NanoPV Team past and present: Dr. Chris Kerestes, Yushuai Dai, Adam Podell, Chelsea Mackos, Michael Welch, Brittany Smith and George Nelson
- Jim Smith, the NPRL Lab Manager, and the entire RIT SMFL staff
- NASA for the NSTRF fellowship that has funded me for the past three years under NNX12AM59H
- AFRL and the University of Toledo for funding the work related to *nipi* solar cells under AFRL grant FA9453-08-C-0172

Contents

List of Tables

List of Figures

Chapter 1

Introduction

1.1 HISTORY AND THE NEED FOR SOLAR POWER

Looking to the sun as a power source for alternative energy is an obvious solution when the amount of energy delivered from the sun to the earth is considered. In 2007 the annual usage of energy was estimated to be 4.6×10^{20} joules, which is the amount of energy the sun delivers to the earth in one hour [1]. Translated into simpler terms, the sun provides approximately 8,760 times more energy to the earth than is currently used, and from a power perspective the sun continuously provides 1.2×10^{5} terawatts, while we consume 13 terawatts [1]. With such an abundant sustainable power source provided to us, it is clear that we should devote resources to harness this power.

When evaluating the optional power sources for outer space, solar power is the only viable source outside of nuclear power. The basis for this can be seen clearly when looking at the International Space Station, where the total power demand is on average 110 kW. This power is supplied by 250 kW solar wings, which weigh in at approximately 8000 pounds. If it is assumed that the wings will work for a total of 30 years the specific energy density of the solar panels is approximately 13 GJ/kg. When compared to hydrogen which is one of the most energy dense materials, hydrogen has an energy density of 141.9 MJ/kg [2] which would require 67 kg of hydrogen per day to power the space station. To compare to the thirty year lifetime of solar wings the deliveries of hydrogen would weigh 92 times that of the initial solar wings. This would not account for the equipment needed to generate power from hydrogen, the compressed gas tanks to deliver it, or the efficiency loss in power conversion.

In order to determine the amount of energy that could be extracted from sunlight a detailed balance calculation was developed by Shockley and Queisser in 1961 to determine the highest conversion efficiency that was attainable with a single junction solar cell. Detailed balance is based on the second law of thermodynamics, accounting for five main loss mechanisms. The losses include thermalization of photons with energies greater than the bandgap, transmission of photons with energies less than the bandgap, radiative recombination emission losses, Carnot losses due to the difference in temperature between the solar cell and the sun as well as Boltzmann losses due to a mismatch between absorption and emission angles. Thermallization and transmission contribute to approximately 75% of the efficiency losses in a device which are depicted in Figure 1.1, and can be limited by changing the material bandgap. The highest single junction efficiency can be achieved with a bandgap energy (E_g) of 1.2 eV, resulting in a conversion efficiency near 31% assuming one sun air-mass zero (AM0) illumination from outside the earth's atmosphere with the device operating at 300K [3]. With single junction devices operating at one sun the highest efficiency to date has been achieved with GaAs at 27.6% [4].

Conventional solar cells rely upon a diffusion dependent current collection process. The base of a single junction solar cell can be typically 2-3 μm to be able to be optically thick; however, the generated minority carriers are required to diffuse that distance prior to collection. Any loss due to non-radiative recombination, depicted in Figure 1.1 results in a loss of current. For most solar cells operating in ideal conditions the material quality is sufficient to minimize the non-radiative recombination prior to collection. Alternative designs can lead to a degraded material quality which would require a drift

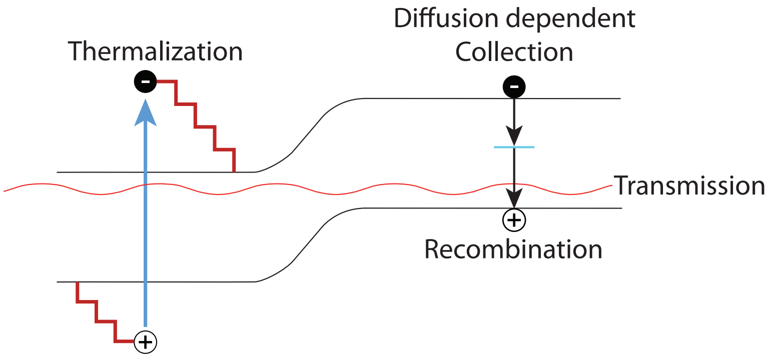

Figure 1.1: A depiction of thermalization and transmission losses, as well as recombination prior to collection.

dominated current collection process.

Some such alternative designs would include the use of low cost substrates, high radiation environments or the inclusion of nano-structures. All of these modifications to a conventional design will induce additional defects within the material, degrading the minority carrier lifetimes. As a result a drift depended current collections is required, which is provided by the *n-type*/intrinsic/*p-type*/intrinsic (*nipi*) superlattice (SL) solar cell.

1.2 PROPERTIES OF *NIPI* SUPERLATTICES

The *nipi* design allows the use of doped and intrinsic layers of any thickness, which translates directly into the electric field strength. As will be discussed in greater detail in Section 2.1 the electric field is dependent upon the thickness and doping of the doped and intrinsic layers. This allows a large design space where the current collection can be due completely to drift drift fields, or at a much lower percentage.

Doping or *nipi* superlattices (SLs) have been discussed in theory for a number of years since the introduction of the quantum well (QW) concept by Esaki [5]. Since that time very little progress has also been made in the fabrication of *nipi* solar cells. They inherently rely upon a drift dominated current collection process, providing benefits for solar cell applications include increased radiation tolerance [6]. Other benefits of the *nipi* SL is an increase in absorption into the infrared due to the inherent formation of QW in the SL [7], and the possibility of forming an intermediate band solar cell (IBSC) with the addition of quantum dots (QDs) [8].

Due to the limited prior research towards the development of a *nipi* solar cell, and the potential use of the device for multiple applications, there is significant need to explore it's use. As will be discussed, the design of a *nipi* solar cell is much more complex than a conventional single or multiple junction solar cell, requiring significant effort focused towards the development of the fabrication process. With an efficient and well characterized fabrication process the opportunities for a *nipi* solar cell are broad. The design is intrinsically radiation hardened, which is ideal for space applications. Also the *nipi* design results in an increased lifetime, which when combined with the possibility of placing quantum dot (QD) within each of the numerous junctions available good opportunity exists for its development as an IBSC. An important factor in an IBSC is controlling the electric field in which the QD are placed, and the *nipi* form factor allows for a much higher level of control and flexibility than a conventional design. Additionally QDs are formed due to strain in the epitaxial growth process, which will inherently cause defects and reduced diffusion lengths, the *nipi* will experience minimal current loss due to reduced diffusion lengths given the drift dominated collection.

The *nipi* solar cell is an alternative to the conventional single or multiple junction device, where multiple junctions are formed in parallel and contacted laterally as depicted in Figure 1.2. As photons generate electron-hole pairs in the active region, they are carried by drift currents into the nearest majority doped regions in the device. Once a carrier becomes a majority carrier, diffusion brings it laterally through the doped region to the carrier-selective contact where it is collected. As depicted in Figure 1.2 the contacts are alternating between *n-* and *p-type*, where the *n-type* contact would make an ohmic contact to the *n-type nipi* layers, and a rectifying barrier to the *p-type nipi* layers. The *p-type* contact

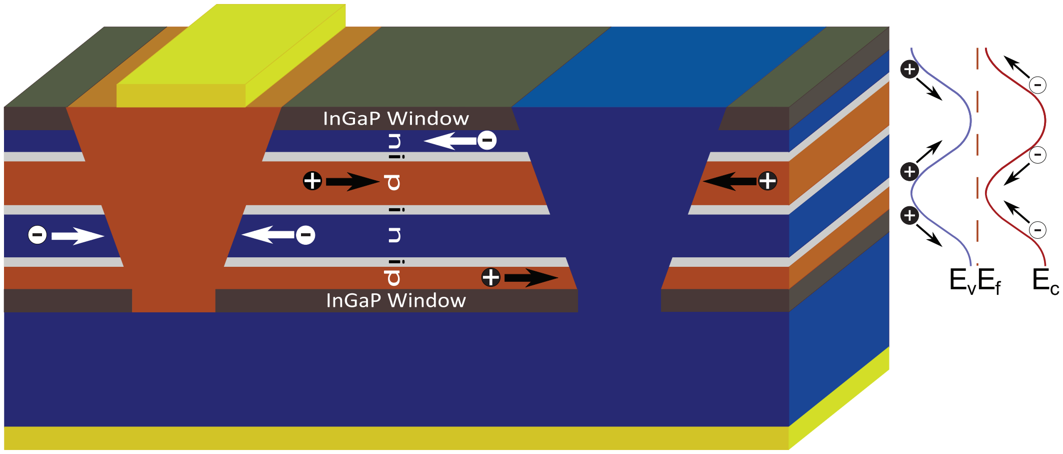

Figure 1.2: Cross sectional schematic of a *nipi* device with epitaxial regrown contacts. Lateral majority carrier current flow is depicted in the figure, with the band diagram shown on the right.

would make ohmic and rectifying contacts to the opposing layers, resulting in carrier selectivity at each contact. The carrier-selective contact can be formed through multiple means, which include epitaxial regrowth, ion implantation, and diffusion, which will be discussed in detail in Chapter 4.

The design allows for a large amount of flexibility, where each SL junction can be of any thickness, and there can be as many or as few junctions as desired. The total thickness of the layer structure could be described with the formula $m * (t_n + t_i + t_p + t_i) + t_n + t_i + t_p$, where m is the number of *nipi* period iterations which can be as low as one and has no set upper limit, t_n, t_i, and t_p are the thicknesses of each layer. The number of period iterations would be determined by the total thickness required for the SL and the thickness desired for each doped or intrinsic layer. The impact from varying the doping density and thickness for each layer will be discussed in Section 2.1. The top and bottom layers in the SL are always a larger bandgap window layer, which is $InGaP_2$ for a GaAs SL. The window layers form a barrier for the minority carriers to prohibit them from interacting with the surface, forcing them to diffuse to the metallurgical junction where they can be collected as current.

A schematic view of a *nipi* solar cell is shown in Figure 1.3 for a device with a *p-type* front and *n-type* back contacts through the substrate. The *p-type* metalization is placed in every other trench, where

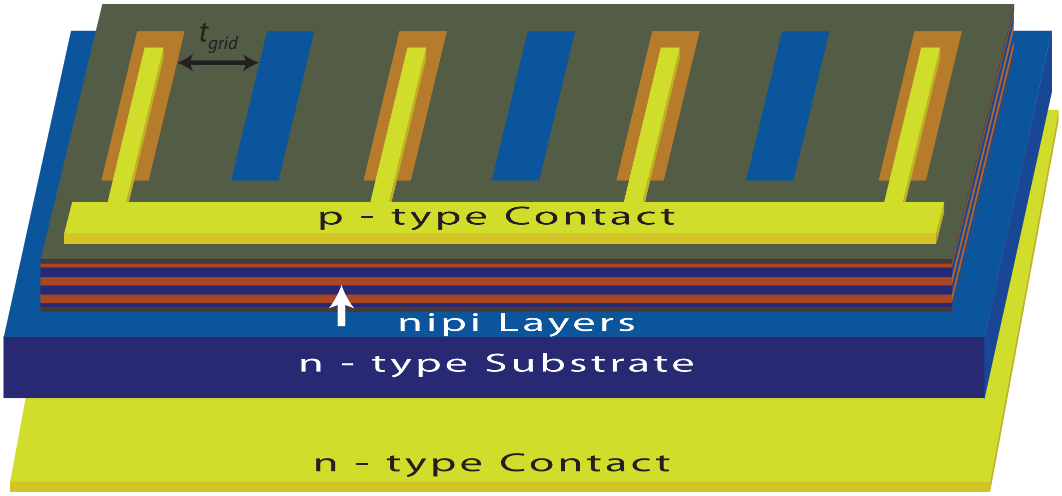

Figure 1.3: A perspective view of a *nipi* solar cell contacted with alternating *n-* and *p-type* regrowths, with front and back side metalization.

the *p-type* carrier-selective contact is formed. The alternating *n-type* carrier-selective contacts have a current path through the substrate which is also *n-type* doped. The grid finger spacing t_{grid} determines the distance the majority carriers must diffuse to reach the contacts, and can be varied through the mask design.

The potential of the *nipi* structure has led to significant theoretical work done by Dohler who developed much of the initial theory related to *nipi* SLs [9, 10, 11, 12], and limited experimental work by others [13, 14] where devices have been fabricated. The majority of the theoretical work has been focused on characterizing the confined states, and absorption within the structure, but additional theoretical work has focused on radiation tolerance [6, 15]. Some experimental work by Cress and Hasnain has focused on solar cells, while no previous work has been done to evaluate the IBSC potential for the structure.

Due to the limited prior research towards the development of a *nipi* solar cell, and the potential use of the device for multiple applications, there is significant need to explore it’s use. As will be discussed, the design of a *nipi* solar cell is much more complex than a conventional single or multiple junction solar cell, requiring significant effort focused towards the development of the fabrication process. With an efficient and well characterized fabrication process the opportunities for a *nipi* solar cell are broad. The design is intrinsically radiation hardened, which is ideal for space applications. Also the *nipi* design results in an increased lifetime, which when combined with the possibility of placing QD within each of the numerous junctions available good opportunity exists for its development as an IBSC. An important factor in an IBSC is controlling the electric field in which the QD are placed, and the *nipi* form factor allows for a much higher level of control and flexibility than a conventional design. The work proposed here will focus largely on developing the fabrication process for this complex device. This will provide platform from which to evaluate the *nipi* solar cell as an IBSC through the fabrication of quantum dot *nipi* (QD-*nipi*) devices. Additional work will also be focused on evaluating the inherent radiation tolerance of the device, proving its potential use for space applications.

1.2.1 Intermediate Band Solar Cell

Modern solar cells have surpassed the Shockley-Queisser single junction limit by employing techniques that limit the thermalization and transmission losses to reach current record efficiencies of 46.0% at 508 suns air-mass 1.5 (global) (AM1.5G) [16]. AM1.5G is a standard illumination spectrum for terrestrially operation with the sunlight passing through one and a half times the earth's atmosphere. Increases in efficiency are gained by monolithically stacking three or more junctions of materials with the largest bandgap on the top to the smallest on the bottom, which are series-connected through tunnel junctions. Each junction's bandgap is designed to absorb all wavelengths with a minimal energy difference between the photon absorbed and bandgap of the sub-cell. This minimizes the transmission losses by having a low bandgap InGaAs (E_g of 1.0 eV) bottom cell grown metamorphically that can absorb light further into the infrared. At the same time the top InGaP (E_g of 1.85 eV) and middle GaAs (E_g of 1.42 eV) cells can absorb the higher energy light with minimal thermalization losses.

Although multiple-junction devices have demonstrated significant gains, there are difficulties that

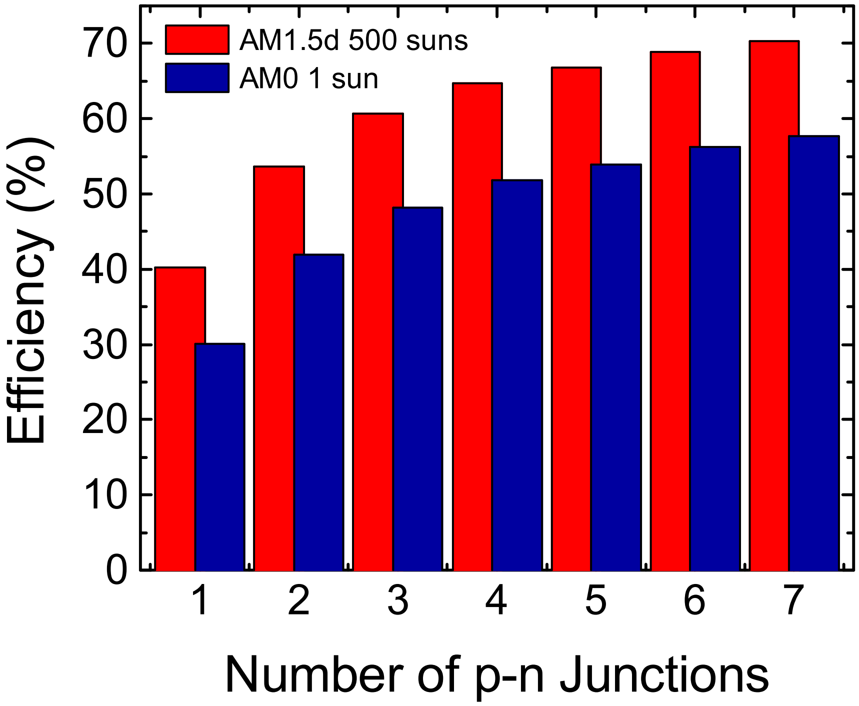

Figure 1.4: Theoretical and realized efficiencies for multiple junction devices for both 500x concentration and one sun.

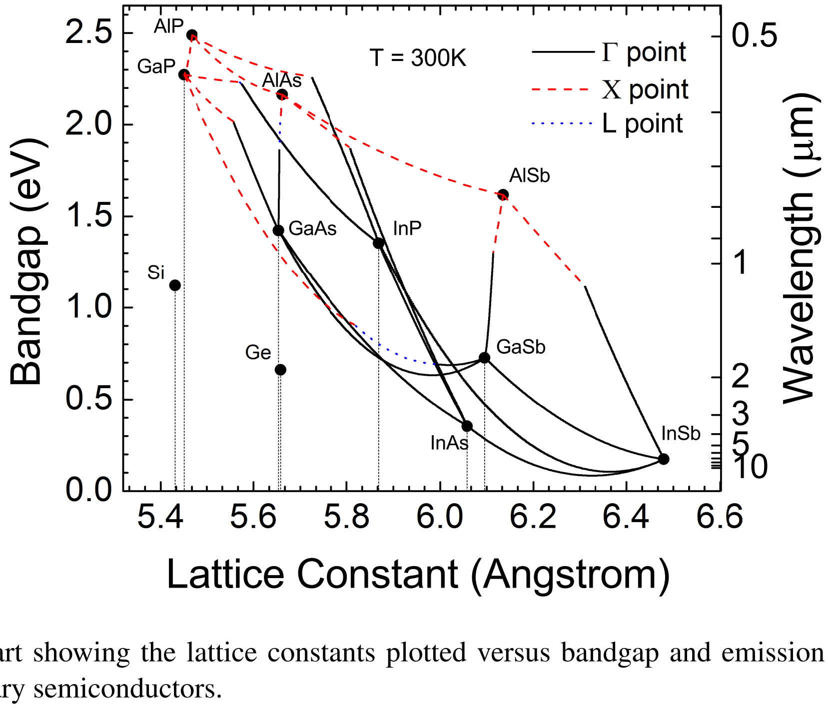

Figure 1.5: Chart showing the lattice constants plotted versus bandgap and emission wavelength for binary and ternary semiconductors.

restrict them from reaching significantly higher efficiencies. In order to further reduce transmission and thermalization losses, additional junctions are required. Increasing the number of junctions has diminishing returns as shown in Figure 1.4 where the maximum detailed balance efficiency for solar cells with one to seven junctions is shown, both under one sun and 500x AM1.5G concentration [17]. The figure shows that as the number of junctions is increased the percent increase in efficiency with respect to the number of junctions decreases. The current generated in a multiple junction device will equal the sub-cell with the lowest current due to Kirchoff's current law. When each of the sub-cells is current matched to the other sub-cells no excess current from an individual sub-cell is lost to heat and higher efficiencies can be achieved. Current matching is an increasingly difficult condition to meet as the number of sub-cells increases because the available semiconductors with a common lattice constant is limited as shown in Figure 1.5. Much recent work has demonstrated triple-junction devices with differing lattice constants grown through metamorphic buffer layers [18, 19, 20]; however, the efficiency is limited by defects formed due to strain [21]. As a result, much current work is focused towards the development of a next generation design, the IBSC [22, 23].

The approach most suited for the *nipi* design is the IBSC approach. The IBSC depends on the formation of an electrically isolated energy band located between the conduction band (CB) and valence band (VB), referred to as an intermediate band (IB) [22]. The band diagram in Figure 1.6 depicts the IB and the transitions allowed between bands. The bulk absorption path between VB and CB exists in parallel with a sequential absorption path. The sequential absorption requires two photons of lower energies than the bandgap of the material to promote one carrier to the CB through the intermediate level. The result is a voltage in the IBSC device equivalent to a bulk device, while collecting current from photons that would otherwise transmit through the semiconductor. This reduces the thermalization and transmission losses, similarly to a triple junction device without having to be concerned with stacking differing semiconducting materials, likely with different lattice constants.

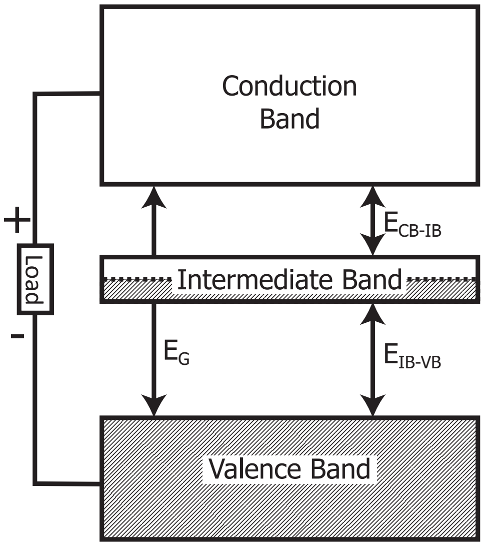

Figure 1.6: Band diagram depicting the absorbing region of an IBSC with each of the energy transitions shown.

The IBSC concept was initially proposed in the 1960 by Wolf [24]; however, it was rejected because the placement of intermediate states within the bandgap would have a net negative impact due to non-radiative recombination through the intermediate states. More recent work proposed by Luque and Marti in 1997 limited the non-radiative recombination by forming a delocalized band of states through which the sequential absorption occurred [22]. Additional requirements have been placed on the design of an IBSC that the IB be half filled with carriers, that the excitation of carriers from the IB be by photons instead of phonons, and that the carrier concentration in each band be defined by its own quasi-Fermi level [25].

To date, most of the work has been done with InAs QD within a GaAs matrix, where the IB is formed in the ground state QD confined levels that exist approximately 0.13 eV below the CB edge [23]. Ideally the bulk E_g would be 1.95 eV with the sub-bandgaps E_{CB-IB} and E_{IB-VB} equal to 0.71 eV and 1.24 eV, respectively, theoretically reaching an efficiency of 63.2% at 46,000 suns [22]. Alternatively, at one sun the sub-bandgaps E_{CB-IB} and E_{IB-VB} could be set at 0.9 and 1.5 eV for an efficiency of 46% [26]. These ideal energy gaps are not feasible with a GaAs bulk material given the E_g of 1.42 eV;

however, InAs QD in GaAs provides a platform within which IBSC concepts can be studied.

Quantum dots have been used in the IBSC solar cell largely because of the zero dimensional confinement that leads to a delta function in the density of states. Having a structure confined to zero spatial dimensions limits motion and changes in momentum in the x and y directions when the carrier is confined in z. By reducing the motion and momentum changes it is more difficult for a carrier to thermalize from IB to CB. A drawback from the QD approach is that epitaxially grown QDs have a density near 3x10^{10} /cm^2 and a diameter of 25 nm [27] which results in QD coverage of less than 15% of the surface. Absorption through the QD confined levels is reduced as a result of the small area that QD cover. Additionally InAs QD are formed by a strain mismatch with GaAs, which can be compensated by GaP [28]; however, slight imperfections in strain balancing will result in a build-up of strain in the SL and a loss in efficiency due to strain related defects [29].

Current limitations in QD materials of lower absorption and strain with increased number of layers result in a challenge for using QD in a conventional solar cells to form an IBSC. Recent results from QD solar cells have shown a peak in sub-bandgap absorption from a device with 40 QD layers having an external quantum efficiency (EQE) of 22% [30]. Accounting for reflectivity, the internal quantum efficiency (IQE) or percent of non-reflected light converted to current is 31%, which means that a minimum of 127 QD layers is required to have the peak in sub-bandgap absorption from a QD device reach 100% IQE, which has not been demonstrated experimentally. The conventional design places the QD within the intrinsic region, which would result in an intrinsic layer on the order of 1.5μm. This would result in a reduced drift field to collect carriers, further reducing current in the conventional design.

For the *nipi*-IBSC approach, the total QD volume can be increased by putting a few QD layers in each of the multiple *nipi* SL junctions. This can be done with minimal degradation due to strain if, for example, if the QD are placed in one layer per *nipi* repeat with the three remaining layers used as a buffer to mitigate the strain. The required 127 QD layers can be formed in a QD-*nipi* solar cell by placing 8 QD layers in each *n* region of a 16 repeat *nipi* stack with no intrinsic layers and repeat period thicknesses of 200 nm. This would allow 100 nm as a buffer layer between every 8 QD layers to mitigate the strain, while having enough QD layers to reach a peak IQE of 100%. Also the electric field the QDs are placed incan be accurately determined, ensuring efficient extraction.

1.2.2 Radiation Tolerance

Solar cells are also used in space environments where electron and proton radiation from the sun can damage and degrade the performance of a device over time. There are two main effects of radiation on a semiconductor. The first is a decrease in minority carrier diffusion length, and the second is an effective change in dopant concentration. As radiation enters the crystal structure, it causes ionizing and non-ionizing interactions with the atom. Greater than 99% of the energy loss in a charged particle is due to ionizing interactions, where an electron is scattered from the atoms in the material [31]. This causes no permanent damage to the crystal structure; however, non-ionizing interactions generate vacancies in the crystal structure which results in residual damage. As the crystalline structure loses the long range continuity of the structure, the diffusion length decreases due to carrier interaction with vacancies and interstitials formed by radiation. Additionally the effective carrier concentration is modified as trap states are introduced, which effectively dope the crystal with either acceptor or donor traps, which is referred to as carrier removal.

Although the effect of radiation on a crystalline material is not design dependent, the effect of the reduced diffusion length and carrier removal is heavily design dependent. A conventional GaAs solar cell will have a base thickness of approximately 2 to 2.5 μm and a total thickness near 2.5 μm to absorb approximately 95% of the incoming light. As radiation damages the lightly doped base the diffusion length will degrade and non-radiative recombination will result in a loss in current. The *nipi* design is flexible where the thickness of a *nipi* period can be easily made as thin as a few nanometers while the thickness of the solar cell can be held constant at the desired 2.5 μm by increasing the number of repeat periods. The *nipi* design can utilize multiple repeat periods of thin *nipi* layers to fully absorb the incoming light, while experiencing minimal loss in carrier collection due to the short diffusion length requirements. This equates to smaller losses in short-circuit current, even with high levels of radiation.

1.3 INTRODUCTION TO MOVPE GROWTH

All of the material development completed in this thesis will involve the use of metal-organic vapor phase epitaxy (MOVPE) growth. Although there are many growth techniques that can form either inorganic or organic materials with crystalline, poly-crystalline, or amorphouse structure, we will be evaluating the use of MOVPE towards the development of high quality single crystal semiconducting materials.

MOVPE growth is distinguished by the use metal-organic (MO) precursor materials for the group-III element, and hydride sources are generally used for the group-V element. The MO sources provide for the possible use of Al, Ga and In with the common MO sources of trimethylaluminum (TMAl), trimethylgallium (TMGa) and trimethylindium (TMIn) respectively. The conventional hydride sources of arsine (AsH_3) and phosphine (PH_3) provide group-V arsenic and phosphorous, with possible MO replacements for As and P, as well as MO possibilities for antimony. The precursors are carried into the reaction chamber in the vapor phase, typically with hydrogen as a carrier gas. The growth occurs on a heated substrate where many thermodynamic and kinetic processes are involved to decompose the precursor molecules and allow atomic reorganization into a single crystal material. A detailed analysis of MOVPE processes will not be completed here, but a general description can be obtained elsewhere [32, 33].

The growth of single crystal semiconductors by MOVPE has been used successfully to develop the highest efficiency solar cells grown to date that had been discussed already. It enables near complete control of material composition, dopant concentration to form *n-* and *p-type* layers, and much work has been done to characterize and minimize the formation of defects in many materials. With the use of the precursors detailed, there are a limited number of binary combinations of materials, however with modern process controls MOVPE can be use to reliably grow ternary, quaternary and higher order combinations of group-III and group-V elements.

The MOVPE growth completed for this thesis has been completed in partnership with National Aeronautics and Space Administration (NASA) Glenn Research Center (GRC) in Cleveland Ohio. The GRC has a Veeco D125LDM rotating disc MOVPE reactor that we use through Space Act agreement SAA3-844 with NASA.

1.4 ORGANIZATION OF THIS DISSERTATION

Chapter 2 gives an introduction to the theory of *nipi* solar cells. The band diagram calculation is developed for a *nipi* SL, and used as a basis to develop an understanding of the radiation tolerance of the design. Theory related to the enhancement in carrier lifetime is also presented, as well as calculations of the quantum confined states in the SL. Finally a simplified analysis of the ideal diode equation is used to evaluate the impact of connecting multiple diodes in parallel in the *nipi* solar cell.

Chapter 3 introduces the simulation methods used to provide a theoretical understanding of *nipi* solar cells. The simulation environment used was Synopsys *Sentaurus*, which is introduced with a single junction device and extended to evaluate a *nipi* solar cell. Trap states were added to the simulation to improve the match to experimental results. Finally the development of an enhanced diode model for a *nipi* solar cell with selective lateral contacts is developed, which is used in Section 5.1.4 to explain an improvement in efficiency with respect to solar concentration.

Chapter 4 discusses the development of the process used to fabricate *nipi* solar cells. Two developments are discussed, first with an epitaxial regrowth process and second with a diffused junction process.

Chapter 5 provides the experimental results achieved during the development of the *nipi* solar cell fabrication process. Multiple process iterations were discussed, with many of the lessons learned addressed in detail. Much of the work focused on the devices fabricated by epitaxial regrowth, including the development and characterization of the regrowth process. Additional work included the analysis of alternate high bandgap contact regrowth semiconductors, as well as the use of a diffused junction process.

Chapter 6 explored the inclusion of QD within the *nipi* SL. Multiple spectroscopic analysis tools were used to evaluate the QD-*nipi* test structures. Absorption, various photoluminescence techniques, and transient absorption techniques were used to characterize the effect of putting QD within the *nipi* structure.

Chapter 7 evaluates the improvement in radiation tolerance of a GaAs based solar cell when using the *nipi* design as opposed to a conventional design. This was initially completed by simulation, followed by experimental characterization. The experimental results were explained further by simulation, and a proposal was made for an alternate *nipi* SL design to improve radiation tolerance.

Chapter 8.1 is a general conclusion section that gives additional recommendations for future work.

Chapter 2

Theory and Device Operation in a Doping Superlattice Solar Cell

Superlattices have been discussed in theory since Esaki proposed them as a means to develop artificial semiconductors in 1970 [5]. A SL consists of a one-dimensional periodic potential that is shorter than the electron mean free path. Superlattices depend on quantum confinement to create allowed and forbidden bands within the wells formed by materials with differing bandgaps or doping levels.

The focus of this work is on doping SLs, which consist of layers of the same material with alternating *n-* and *p-type* doping that modulates the CB and VB, forming QW when the layers are spaced close enough. The benefits to this form of SL will be discussed in the subsequent sections, which include the reduction or elimination of strain in a SL, a type-II band alignment, enhanced carrier lifetime, tunability of the subbandgap states and a reduction in minority carrier recombination. Doping SLs can also be combined with material or compositional SLs to realize non-linear absorption effects and increased tunability in the confined states [34, 35, 36].

Over the past 40 years the majority of the theoretical and experimental work with SLs has consisted

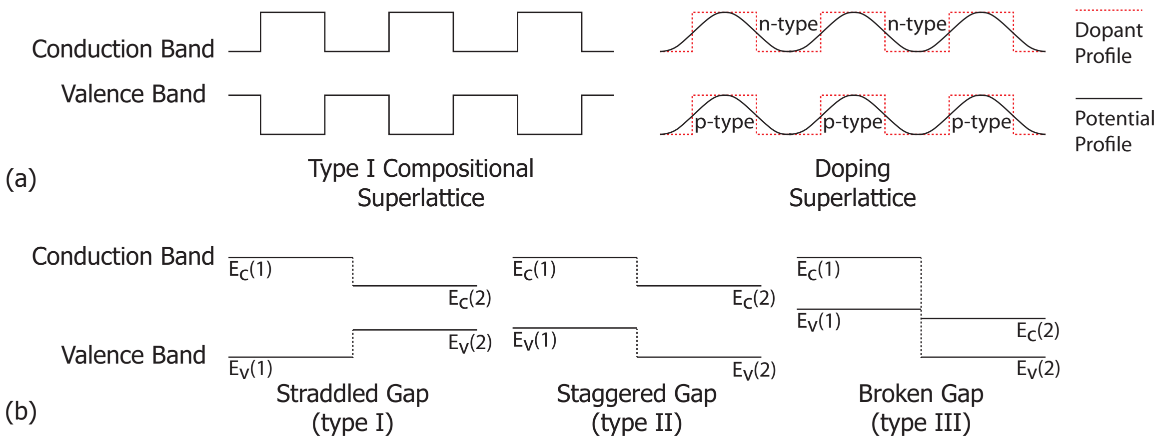

Figure 2.1: A band diagram depicting (a) compositional and doping Sls, in addition to (b) the alignment of type-I, II and III semiconductor heterojunctions.

of material or compositional SLs. Varying the material or composition can result in a significant amount of strain due to differing lattice constants as shown in Figure 1.5 where the bandgap is plotted versus lattice constant. Doping SLs are inherently strain free due to the use of homoepitaxial growth, where the SL potential is formed by varying doping while the material is typically held constant.

The band diagram of a doping SL also differs from a compositional SL, as shown in Figure 2.1 (a). When a doping SL is compared to a type I compositional SL, there are two main differences of note. The first difference is that there are no discontinuities at the junctions between different doping levels, as there are between differing materials in the compositional SL. The second difference is that the doping SL is more like a type II SL, where the bandgaps overlap, but the one bandgap is not contained within the other as depicted in the staggered gap illustration in Figure 2.1 (b). Most compositional SLs are type I, where one bandgap is contained within the second bandgap; however, depending on the materials used, type II and III SLs can also be formed. The theory developed here will show the benefits of using a *nipi* SL with a quasi-type II band alignment and near continuous electric field.

2.1 CALCULATION AND EFFECT OF BAND STRUCTURE IN *NIPI* DEVICES

Having a continuously varying band instead of a discontinuity at the interface affects the electric field in the structure. For a compositional SL with materials that have matched vacuum levels, there is no band bending in either material and zero electric field in the layer outside of the interface itself. The doping SL does have a varying electric field through the depleted regions of the doped layers, and through the entire intrinsic region. The effect of the electric field has already been briefly mentioned in Section 1.2.2, where it was observed that it helps more efficiently collect carriers.

Assuming that a *nipi* stack has constant doping in each layer, matched *n*- and *p-type* doping levels, fully depleted layers in the depletion region, and perfectly abrupt interfaces between each layer, the electric bands can be calculated with the following manipulation of Poisson's equation. To calculate the band diagram Poisson's equation must be solved along with the continuity equation for four distinct regions depicted in Figure 2.2.

Each region is given the following definition: N_D and N_A are the donor acceptor concentrations; d_n, d_p and d_i are the *n-type*, *p-type* and intrinsic layer thicknesses, respectively; d_n^+ and d_p^- are the depletion region thicknesses in the *n*- and *p-type* layers, while d_n^0 and d_p^0 are the *n*- and *p-type* quasi neutral region thicknesses; d is the entire *nipi* period thickness, ϵ is the relative permittivity, and q is the elemental charge. The calculation of the electric field as a function of position in the growth axis z is described in the following set of equations:

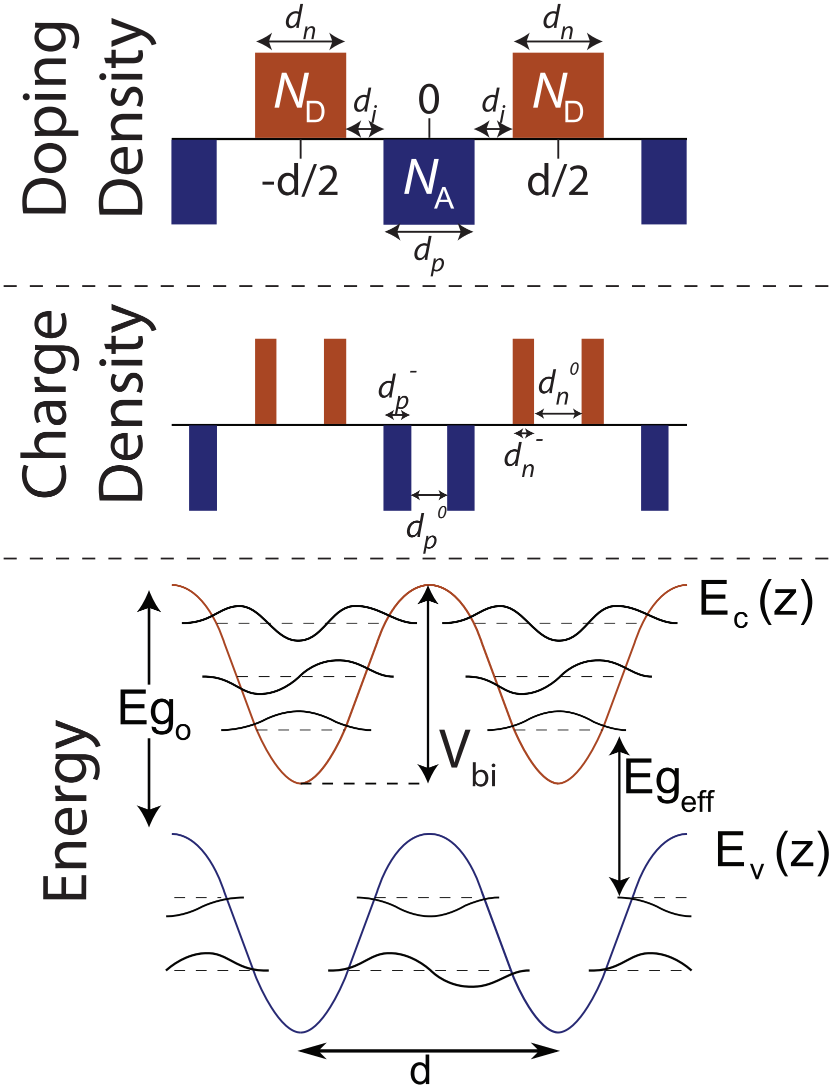

Figure 2.2: Charge density of a *nipi* stack is shown on top, with the calculated energy band diagram shown below with confined levels within the superlattice.

$$\varepsilon(z) = \frac{1}{\epsilon}\int \rho(z)dz = \begin{cases} 0 & \text{if } |z| < \frac{d_p^0}{2} \\ -\frac{qN_A}{\epsilon}\left(\frac{d_p^0}{2} - |z|\right) & \text{if } \frac{d_p^0}{2} < |z| < \frac{d_p}{2} \\ \frac{qN_A}{\epsilon}\frac{d_p - d_p^0}{2} & \text{if } \frac{d_p}{2} < |z| < \frac{d-d_n}{2} \\ \frac{qN_D}{\epsilon}\left(|z| - \frac{d-d_n^0}{2}\right) & \text{if } \frac{d-d_n}{2} < |z| < \frac{d-d_n^0}{2} \\ 0 & \text{if } \frac{d-d_n^0}{2} < |z| < \frac{d}{2} \end{cases} \tag{2.1}$$

The electric field can then be used to calculate the potential φ, which is shown in (2.2).

$$\varphi(z) = -\int \varepsilon(z)dz = \begin{cases} 0 & \text{if } |z| < \frac{d_p^0}{0} \\ -\frac{qN_A}{2\epsilon}\left(|z| - \frac{d_p^0}{2}\right)^2 & \text{if } \frac{d_p^0}{2} < |z| < \frac{d_p}{2} \\ -\frac{qN_A(d_p - d_p^0)}{2\epsilon}\left(|z| - \frac{d_p + d_p^0}{4}\right) & \text{if } \frac{d_p}{2} < |z| < \frac{d-d_n}{2} \\ \frac{qN_D}{2\epsilon}\left(|z| - \frac{d-d_n^0}{2}\right)^2 - V_{bi} & \text{if } \frac{d-d_n}{2} < |z| < \frac{d-d_n^0}{2} \\ -V_{bi} & \text{if } \frac{d-d_n^0}{2} < |z| < \frac{d}{2} \end{cases} \tag{2.2}$$

where V_{bi} is the build-in potential between the doped layers, which is calculated by (2.3) when a quasi-neutral region exists in the doped layers, or by (2.4) when the entire doping SL is depleted.

$$V_{bi} = \frac{kT}{q} * ln\left(\frac{N_A N_D}{n_i^2}\right) \tag{2.3}$$

$$V_{bi} = \frac{q}{2\epsilon}\left(\frac{N_D(d_n^+)^2}{2} + \frac{N_A(d_p^-)^2}{2} + N_D d_n d_i\right) \tag{2.4}$$

For the calculation within the depleted SL, it is necessary to be able to calculate the depletion region thicknesses within the *n-* and *p-type* layers, which are shown in (2.5) and (2.6), respectively. For devices with the quasi-neutral region in the doped layers no calculation is required to determine the depletion region thickness since $d_n^+ = \frac{d_n}{2}$ and $d_p^- = \frac{d_p}{2}$.

$$d_n^+ = \frac{\left(d_i^2 + \frac{2\epsilon*(N_D+N_A)*V_{bi}}{qN_DN_A}\right)^{1/2} - d_i}{1+\frac{N_D}{N_A}} \tag{2.5}$$

$$d_p^- = \frac{\left(d_i^2 + \frac{2\epsilon*(N_D+N_A)*V_{bi}}{qN_DN_A}\right)^{1/2} - d_i}{1+\frac{N_A}{N_D}} \tag{2.6}$$

The electric field within each of the doped and intrinsic layers results in rapid carrier collection with minimal recombination, as can be shown from the calculation in (2.1). With a doping of 1x10^{18} /cm^3 and each layer having a thickness of 50 nm (200 nm period) the electric field reaches a maximum of 2.18x10^7 V/m, while 55% of the doped region is depleted by an electric field indicating that the longest required diffusion length is 22.5 nm. A representation of a band diagram is shown in Figure 2.3 which shows how having thin *nipi* layers allows the electric field to collect nearly all of the generated carriers rapidly due to the minimization of the quasi-neutral region by design.

The theory presented here utilized Poisson's equations, which provide accurate calculations for most applications. As the thickness of the layers is decreased the accuracy of Poisson's equations decreases due to quantum size effects. In order to improve the calculation a periodic boundary condition could be applied to find a Bloch solution.

2.1.1 Enhanced Radiation Tolerance

A specific application where the high electric fields and tunable diffusion length requirements are beneficial is for high radiation applications. Such an environment would be in the earth's orbit where protons and beta particles radiated from the sun are captured in the earth's magnetic field. Solar panels used

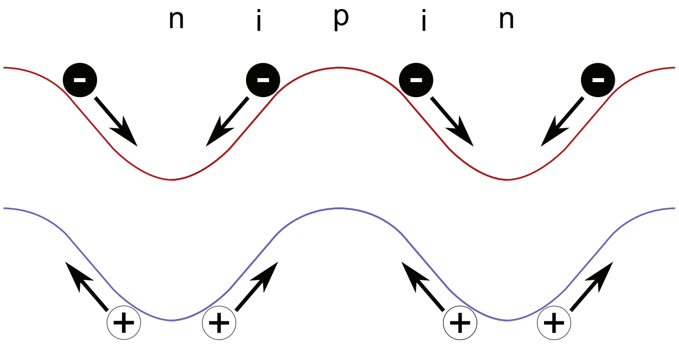

Figure 2.3: A band diagram of a *nipi* superlattice, depicting minority carrier collection via drift

to power satellites are particularly vulnerable to radiation which can reach 1 MeV electron fluxes exceeding 10^7 cm^{-2}s^{-1} in the worst-case environments, which would reach a fluence of 1x10^{15} /cm^2 in slightly over three years [37]. As protons and electrons interact with a semiconductor crystal the non-ionizing radiation displaces atoms from the crystal lattice, which leaves voids and interstitial atoms in the lattice. This degrades the minority carrier diffusion length, and a empirical formula shown in (2.7) has been developed to describe the degradation where L_ϕ is the diffusion length following a radiation fluence ϕ, L_o is the beginning-of-life (BOL) diffusion length, and K_L is a damage coefficient [38].

$$\frac{1}{L_\phi^2} = \frac{1}{L_o^2} + K_L\phi \tag{2.7}$$

The current collection in the quasi-neutral regions of a solar cell will degrade as the diffusion length is reduced to the length scale of that region. For a conventional GaAs *nip* solar cell design the base is typically 2 to 3 μm that is approximately 1x10^{17} /cm^3 *p-type* doped with a BOL diffusion length approximately 10 μm [39]. Alternately the BOL diffusion length for a *nipi* device with doped layers at 1x10^{18} /cm^3 and *nipi* period thickness of 200 nm is between 1 and 2 μm in the *n-type* layers [39]. The limit for the end-of-life (EOL) diffusion length can be approximated by the physical base width in the conventional design and d_n^0 for the *nipi* design. The limiting EOL diffusion length would be 2 μm and 22.5 nm, for the single junction and *nipi* devices, respectively. As a result the *nipi* device will withstand four orders of magnitude higher fluence than the single juction solar cell. The relative diffusion length enhancement can be either increased or decreased in *nipi* devices by varying the thickness of the doped layers, which increases flexibility.

A second reason for an increased radiation tolerance is due to an effect called carrier removal [40]. As radiation damage occurs, a semiconductor can be type converted from one dopant type to the other due to radiation induced traps compensating the intentional dopants. Radiation preferentially induces *n-type* compensating traps in GaAs according to (2.8) where p_o is the initial carrier concentration, p_ϕ is the carrier concentration after radiation dose ϕ, and R_c is the damage coefficient [38]. For a *nipi* structure, it is desirable to dope each of the layers with high dopant concentrations to decrease the resistivity in the doped layers, which also results in a high tolerance to carrier removal effects. In a conventional solar cell the base is often doped in the range of 1x10^{17} cm^{-3} to increase the minority carrier diffusion length. If the base is *p-type*, type conversion effects will set on at a lower dose than in the highly doped *nipi* devices.

$$p_o - p_\phi = R_c\phi \tag{2.8}$$

2.2 CARRIER LIFETIME ENHANCEMENT

The second difference between a type I compositional SL and a doping SL is the move from a type I to a type II junction, which impacts the carrier dynamics at the interface. In a type I SL, recombination from CB confined levels to VB levels does not require a change in spatial location. However, the doping SL, or quasi-type-II SL has CB and VB confined levels in different spatial locations. Confined states exist in the CB of the *n-type* material, and in the VB of the *p-type* material, which requires a spatially indirect transition to absorb or recombine through the confined states. Although the absorption coefficient is decreased due to the decreased likelihood of a spatially indirect transition, the benefit is that minority carrier lifetimes are dramatically increased. Increases in lifetime are essential in order to efficiently collect carriers that are absorbed prior to recombination.

The overlap integral between the electron and hole wave functions has been calculated to determine the theoretical increase in lifetime within a *nipi* SL [41]. The overlap is calculated between the lowest conduction and uppermost valence confined subbands within each doped layer. It is assumed that both *n-* and *p-type* layers are fully depleted, have constant doping and no intrinsic region. Given this assumption, the band structure can be approximated by a harmonic oscillator to find the ground state energy where the wavefunction $\psi_{i,0}$ is given by

$$\psi_{i,0}(z) = \left(\frac{1}{\sqrt{\pi}}\alpha_i\right)^{1/2} e^{\left(\frac{-z^2}{2\alpha_i^2}\right)} \tag{2.9}$$

where α_i is given by (2.11) and (2.12), and z is position in the growth direction. The carrier wavefunction is used to determine the overlap factor

$$< e,0|hh,lh,0 > \begin{cases} \backsimeq \sqrt{\dfrac{1}{\sqrt{\pi}\alpha_e\alpha_{hh,lh}}} \displaystyle\int e^{\left(\frac{-z^2}{2\alpha_e^2}\right)} e^{\left(\frac{-(d/2-z)^2}{2\alpha_{hh,lh}^2}\right)} dz \\ = \sqrt{\dfrac{2\alpha_e\alpha_{hh,lh}}{\alpha_c^2+\alpha_{hh,lh}^2}} e^{\left(\frac{-(d/2)^2}{2(a_e^2+a_{hh,lh}^2)}\right)} \end{cases} \tag{2.10}$$

where

$$\alpha_e = \sqrt{\frac{\hbar}{m_e^*\omega_e}} \tag{2.11}$$

and

$$\alpha_{hh,lh} = \sqrt{\frac{\hbar}{m_{hh,lh}^*\omega_{hh,lh}}} \tag{2.12}$$

are the decay lengths, where $\hbar$ is the Plank constant, m_e and $m_{hh,lh}$ are the electron and hole effective masses, and the bulk plasmon frequencies for electrons and holes are given by

$$\omega_e = \sqrt{\frac{qN_D}{\epsilon m_e}^{*}} \tag{2.13}$$

$$\omega_{hh,lh} = \sqrt{\frac{qN_A}{\epsilon m^*_{hh,lh}}} \tag{2.14}$$

The enhancement in lifetime with respect to bulk values can be calculated by squaring the inverse of the overlap matrix shown in (2.10), which is

$$\frac{\tau^{nipi,0}}{\tau^{bulk}} \backsimeq \begin{cases} \dfrac{\alpha_e^2 + \alpha_{hh,lh}^2}{2\alpha_e \alpha_{hh,lh}} e^{\frac{(d/2)^2}{\alpha_e^2 + \alpha_{hh,lh}^2}} \\ \dfrac{\omega_e + \omega_{hh,lh}}{2(\omega_e \omega_{hh,lh})^{1/2}} e^{\frac{4V_{bi}}{\hbar(\omega_e + \omega_{hh,lh})}} \end{cases} \tag{2.15}$$

where $\tau^{nipi,0}$ is the electron or hole lifetime in the *nipi* SL, while τ^{bulk} is the lifetime in the bulk. A lifetime enhancement factor of 10^{13} is calculated from (2.15) for a SL with $d = 80$ nm and doping of 1x10^{18} /cm^3 over a typical nanosecond range lifetime in GaAs. Some experimental work has demonstrated extended lifetimes in *nipi* SLs into the microsecond range in GaAs [42], which is significantly less than theoretical predictions; however, still demonstrating significant enhancements.

2.3 SUB-BANDGAP ABSORPTION

The *nipi* SL forms potential wells in the CB between two *p-type* layers, and in the VB between two *n-type* layers. When the spacing of the potential well is on the same length scale as the DeBroglie wavelength, quantum confined levels will exist within the potential well. Given the shape of the potential well, the harmonic oscillator solution is a relatively good approximation for the lower energy levels. Assuming the doped layers have equivalent doping levels and there is no intrinsic layer, the quantized

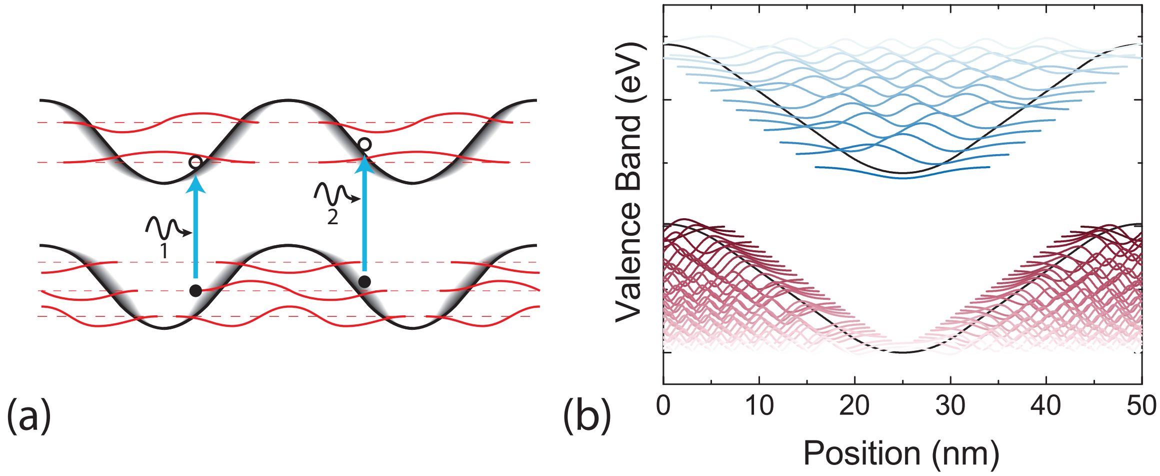

Figure 2.4: (a)Band diagram depicting the two mechanisms of absorption, with collection through the confined states shown as mechanism 1, and via the F-K effect as mechanism 2, and (b) energy levels calculated for a superlattice with 50 nm periods and 6x10^{18} /cm^3 doping.

energy levels can be calculated with the following equation:

$$\varepsilon_{e,hh,lh} = \hbar \left(\frac{q^2 N_D}{\epsilon m^*_{e,hh,lh}} \right)^{1/2} \left(n + \frac{1}{2} \right) \tag{2.16}$$

where ϵ is the relative permittivity, m^* is the effective mass, and n is the confined level index. A representation of the confined levels is shown in Figure 2.4 (a) with each energy level depicted in red. Due to the harmonic oscillator solution, the energy levels will be nearly equally spaced within the potential well. Energy levels calculated by the effective-mass approximation (EMA) are shown in Figure 2.4 (b) for a SL with period of 50 nm and doping of 5x10^{18} /cm^3.

The sub-bandgap absorption from the confined energy levels depends on the interband matrix element, which contributes a relatively small amount to the total absorption for most SL designs that have been used for solar cells where the layer thickness is on the range of 50 nm or more. A second component that contributes to sub-bandgap absorption is due to the Franz-Keldysh (F-K) effect which comes about from the strong homogeneous electric field through the SL. Both effects will contribute to absorption, and the SL design will determine the sub-bandgap absorption that each effect contributes.

Since the absorption coefficient is a function of the location within the SL, where the F-K effect will be strong in the high field regions and negligible in the quasi-neutral regions, it is appropriate to integrate the absorption as a function of electric field [43]. Bulk and field-generated absorption can be added to the absorption due to the overlap between the CB and VB states, for which the theory has been developed elsewhere [12] and described in the following equation:

$$\alpha^{nipi}(\omega) \approx \frac{1}{d}\int_0^d \alpha^b(\omega;\varepsilon(z))dz + \alpha_{confined}(\omega) \tag{2.17}$$

where d is the *nipi* period thickness, α^b is the bulk spectral absorption, ω is the frequency of the incoming light, $\varepsilon(z)$ is the varying electric field described in (2.1), and $\alpha_{confined}$ is the absorption component from the overlap between CB and VB states. The electric field increases and decreases linearly, which results in the integral expanding to

$$\begin{aligned}\alpha^{nipi}(\omega) \approx \frac{1}{d}\left[d_n^0\alpha_n^b(\omega) + d_p^0\alpha_p^b(\omega) + 2d_i\alpha^b(\omega;\varepsilon_{max}) + 2(d_n^+ + d_p^-)\varepsilon_{max}\int_0^{\varepsilon_{max}}\alpha^b(\omega;\varepsilon)d\varepsilon\right] \\ + \alpha_{confined}(\omega)\end{aligned} \tag{2.18}$$

The values of $\alpha_n^b(\omega)$ and $\alpha_p^b(\omega)$ are the bulk absorption values for the *n*- and *p-type* doped regions which are not modified by the electric field. Equation 2.18 can be broken up into two parts. The first part is a function of electric field resultant from the F-K effect and the second part is $\alpha_{confined}(\omega)$ which will be dealt with later. Absorption is directly proportional to the dielectric function, where

$$\alpha(\omega) = \frac{\omega}{n(\omega)c}\epsilon_2(\omega;\varepsilon) \tag{2.19}$$

when $n(\omega)$ is the refractive index and c is the speed of light. The dielectric function of a material existing within an electric field can be calculated from the following equation:

$$\epsilon_2(\omega;\varepsilon) = C\sum_i \mu_i^{3/2}(\hbar\Omega_i)^{1/2}\int_0^\infty x^{1/2}Ai\left(x+\frac{E_{g_o}-\hbar\omega}{\hbar\Omega_i}\right) \tag{2.20}$$

where C is a constant, Ai is the Airy function, E_{g_o} is the bulk semiconductor bandgap, and $\hbar\Omega_i$ is the characteristic energy for the electric field, given by

$$\hbar\Omega_i = 2^{-2/3}\left[\frac{\hbar}{2}\frac{q^2\varepsilon^2}{\mu_i}\right]^{1/3} \tag{2.21}$$

The term $1/\mu_i$ is the reduced effective mass for transitions from the ith VB level into the CB, which is given by

$$\frac{1}{\mu_i} = \frac{1}{m_e} + \frac{1}{m_{hi}} \tag{2.22}$$

The function of $\alpha(\omega)$ reduces exponentially as $\hbar\omega$ is reduced below the bandgap, and only exists for values close to the bandgap. The dielectric function $\epsilon_2(\omega;\epsilon)$ oscillates around $\epsilon_2(\omega;0)$ with a period on the order of $\hbar\Omega_i$, which corresponds to the overlap between the CB and VB envelope functions. The oscillations are damped as $\hbar\omega$ becomes greater than the semiconductor bandgap until they approach $\epsilon_2(\omega;0)$. The absorption coefficient is increased as the electric field and size of the depleted d_n^+ and d_p^- regions are increased.

From the preceding equations the absorption as a function of electric field can be calculated; however, the absorption due to overlap of the confined states requires additional development. The dielectric function with respect to the confined levels can be determined via the EMA from the following equation:

$$\epsilon(\omega) = 2\frac{q}{m_o^2\omega^2 d}\sum_{h=hh,lh}\sum_{n,m}|<e,n|p|h,m>|^2 N^{(2)}_{hn,em}(\hbar\omega) \tag{2.23}$$

where n and m are the CB and VB confined state indices, respectively, and the joint density of states is given by

$$N^{(2)}_{hn,em}(\omega) = \left[\pi\hbar^2\left(\frac{1}{m_e} + \frac{1}{m_h}\right)\right]^{-1} \theta(\omega - (E_{g_o} - V_{bi} + \varepsilon_{en} + \varepsilon_{(hh,lh)m})) \tag{2.24}$$

when V_{bi} is calculated from (2.3) or (2.4) depending on the conditions; also, ε_{en} and $\varepsilon_{(hh,lh)m}$ are described by (2.16). The function $\theta(x)$ is a unity step function where $\theta(x > 0) = 1$ and $\theta(x < 0) = 0$ which ensures that frequencies below the energy difference between confined states are not absorbed. The calculation of the joint density of states can be further improved by accounting for the effects of temperature broadening the absorption edge from a step function at temperatures above absolute zero. This can be completed by modifying Θ with an effective Fermi function according to the following equation

$$\Theta(\omega - (E_{g_o} - V_{bi} + \varepsilon_{en} + \varepsilon_{(hh,lh)m})) = \frac{1}{e^{[(E_{g_o} - V_{bi} + \varepsilon_{en} + \varepsilon_{(hh,lh)m}) - \omega]/kT} + 1} \tag{2.25}$$

Photons with energies near the semiconductor band edge are the only photons that will be absorbed by the overlap between confined states. The sub-bands that will have the strongest overlap and absorption are the lowest conduction sub-band and the highest valence sub-band. If these sub-bands are evaluated the square of the interband matrix element can be given by

$$| < e, n|p|h, m > |^2 \simeq \left(\rho^{bulk}_{h,e}\right)^2 e^{\frac{-(d/2)^2}{\alpha_e^2 + \alpha_{lh,hh}^2}} \tag{2.26}$$

where $\rho^{bulk}_{h,e}$ is the bulk interband matrix element of momentum at the Γ point, α_e is given in (2.11) and $\alpha_{lh,hh}$ is given in (2.12).

As a result of (2.23) and (2.24) it is apparent that the absorption coefficient increases as a step function with respect to frequency. Additionally as the electric field is increased in the SL the overlap

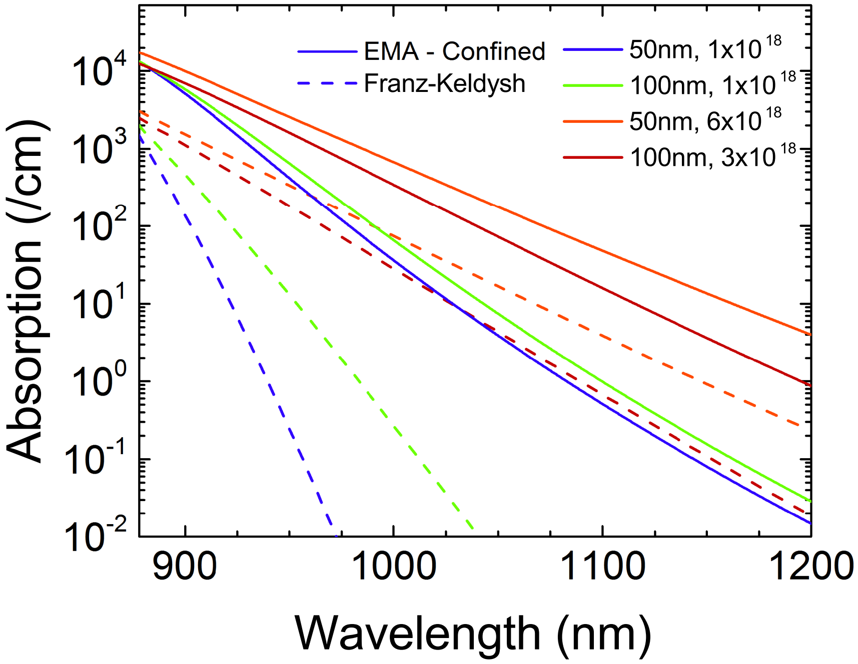

Figure 2.5: Sub-bandgap absorption due to overlap of the confined levels and the F-K effect. Absorption was calculated for four different superlattice layers with doping of 1x10^{18} and 6x10^{18} /cm^3 and *nipi* periods of 50 and 100 nm.

integral is correspondingly increased due to an increasingly steep potential barrier being created. Thus the absorption due to the F-K effect and overlap of the confined energy states is driven by the strength of the electric field in the SL.

Sub-bandgap absorption from both the confined levels and the F-K effect have been calculated and are shown in Figure 2.5. The step-wise nature of absorption from the confined levels is lost when broadening of the states at 300K is accounted for, resulting in a smooth absorption profile with respect to wavelength. Absorption from both effects is increased as the average electric field in the SL is increased. These results and comparisons to experimental measurements will be discussed in greater detail in Section 6.2.1.

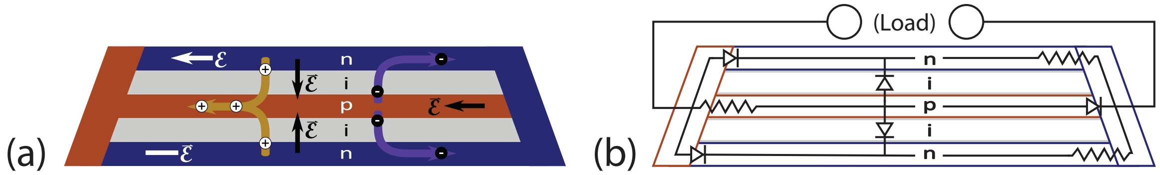

Figure 2.6: A cross-section of a laterally connected *nipi* superlattice (a) with an equivalent circuit drawing of the same structure (b)

2.4 CHARACTERISTICS OF A *NIPI* SUPERLATTICE SOLAR CELL

In a doping SL the electric field switches direction as a function of position along the growth axis. This prohibits the use of top and bottom contacts to a solar cell as would be used in a conventional *pin* solar cell. Carriers generated in the middle *nipi* layers would be trapped by the potential wells formed around them. As a result a lateral contact design must be used as depicted in Figure 1.2.

The material used to contact the sidewalls of the *nipi* SL layers must be able to form both an ohmic and rectifying contact to the SL as depicted in the equivalent circuit in Figure 2.6. As can be seen in the schematic, the left contact forms an ohmic contact to the *p-type* layer while also forming a rectifying barrier to the *n-type* layer and the right contact has an inverse relationship with the doped layers. The methodology of forming this contact will be detailed in Chapter 4 but, in short, *n-* and *p-type* doped layers work well to fulfill this function.

The simplified schematic shown in Figure 2.6 only has five SL layers and two diodes in the growth direction, but it is easy to imagine a significant increase in the number of layers. Given a SL with 50 nm n, i and p layers and a total thickness of 2.5 μm, a total of 25 diodes would be formed vertically. Since each of the SL diodes is in parallel, they would all be at the same voltage and contributing equally to the dark current. The dark current is described by (2.27) where J_o is the dark saturation current, R_s is series resistance, R_{shunt} is shunt resistance, n is the ideality factor, and k is the Boltzman constant. For the *nipi* device the ideal diode equation is modified by a factor $2m + 1$ as shown in (2.28) where m is the number of *nipi* repeat periods assuming a layer structure of $m * (n + i + p + i) + n + i + p$ is used.

$$J = J_o e^{\frac{q(V - JR_s)}{nkT}} + \frac{V - JR_s}{R_{shunt}} \tag{2.27}$$

$$J = (2m + 1) \left[J_o e^{\frac{q(V - JR_s)}{nkT}} + \frac{V - JR_s}{R_{shunt}} \right] \tag{2.28}$$

The ideal diode equation can be rearranged to estimate the open-circuit voltage (V_{OC}) of a solar cell at a specific current level. This can be used to estimate the loss in V_{OC} incurred by adding multiple junctions in parallel. A single junction diode with J_o of 10^{-10} A/cm^2, n of 2, R_s of zero, R_{shunt} of infinity, temperature of 300K, current of 20 mA/cm^2 operating at one sun will have a V_{OC} of 0.988 V. When 25 diodes are connected in parallel the V_{OC} calculated by (2.28) is 0.8218 V or 83.2% of the single junction design.

Such a loss in V_{OC} is a drawback to the *nipi* design; however, the loss can be mitigated. Many of the III-V solar cells in production are designed to operate under concentration, where the intensity of the sun is magnified via lenses or mirrors. A logarithmic relationship between current and voltage is demonstrated in (2.27), so as the current increases the voltage increases as the log of the current. This presents a significant advantage for devices under concentration where the current increases proportionally to the multiplicative factor of suns. For the single junction example the result would be a 32.5% increase in efficiency at a concentration of 500 suns assuming no series resistance losses. This benefit is even more exaggerated in the *nipi* solar cell where the dark current levels are higher. Moving to the same concentration of 500 suns results in a 39.1% increase in efficiency over the one sun level, and is only 12.7% lower efficiency than the single junction design. The relative efficiency loss is even less for the *nipi* design if current collection is improved due to the minimization of non-radiative recombination

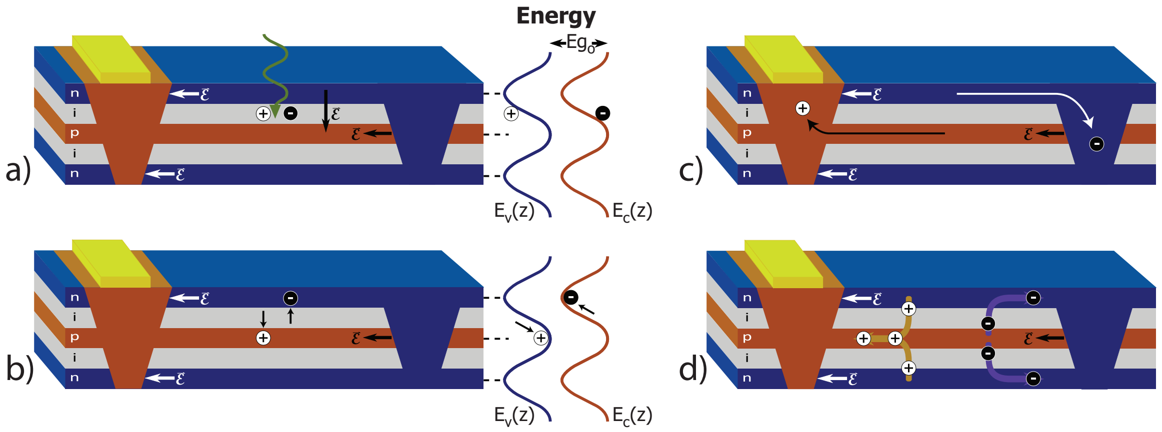

Figure 2.7: A schematic demonstrating the current flow in a *nipi* solar cell where a) a photon is absorbed, generating an EHP, b) the charges are separated by an electric field, c) and finally the charges diffuse to the epitaxially regrown contacts, where d) is an illustration of the carrier flows and electric fields

prior to collection, or due to the increase in sub-bandgap current as discussed in Section 2.3.

In the previous example series resistance was ignored; however, it is a factor in all solar cell devices. The current paths for a *nipi* solar cell are shown in Figure 2.7, where Figure 2.7 a) shows the absorption of a photon and generation of electron-hole pair (EHP), followed by the separation of carriers by drift in Figure 2.7 b), after which the carriers diffuse to the contacts as shown in Figure 2.7 c). The drift collection has already been discussed in Section 2.1; however, the lateral diffusion through the *nipi* layers has not been discussed.

Given the reduction in quasi-neutral region thickness the undepleted conducting layer in the top *p-type* layer is only 22.5 nm thick. In a conventional *pin* design the thickness of the emitter will be in the range of 500 nm, and will carry the current from the entire device. A comparison of resistances between the two devices shows that the resistance in the top *nipi* layer would be approximately 22 times greater assuming equivalent doping and grid finger spacing. For the example of 50 nm *nipi* layers, 2.5 μm thick device, with a 50 nm InGaP window the percent of light that will be absorbed in the top junction (125 nm) is 43.7% of the total light, which translates to 43.7% of the total current. Power is lost proportionally to I^2R, which results in a 4.2 times greater power loss in the *nipi* design than the conventional solar cell.

This power loss can be compensated for by increasing the doping in the SL layers. The effect would be a decrease in series resistance, improvement in V_{OC}, an increase in the conducting layer width due to a decrease in depletion width, and a minimal trade-off with respect to recombination given the decreased diffusion length requirement. Another way to mitigate the loss would be to increase the doped layer thickness; however, this would also increase the current carried in each layer reducing the benefit in power loss. Alternatively it would be possible to have *n-* and *p-doped* layers with differing thicknesses due to the order of magnitude higher resistivity in *p-type* GaAs.

2.5 CONCLUSION

In this chapter the theory of the *nipi* SL has been developed. The band diagram was calculated using Poisson's equation. The existence of a high electric field through the entire active region of the device was then used to explain the possible increases in radiation tolerance for the design. The effects of the band diagram were further discussed by evaluating the change in lifetime by forming an effective type-II superlattice where the electrons and holes are separated. The result is a possible increase in lifetime by a factor of 10^{13} with certain SL designs.

Theory on the *nipi* structure has been further developed to include the calculation of confined energy states in the parabolic potential wells formed by the *nipi* SL. The confined levels were calculated by EMA and the overlap of the bands was used to calculate the expected absorption in the SL. This was added to absorption that was expected from F-K absorption, from high electric field resulting in an effective broadening of the bandedge. Absorption from both effects was calculated and the absorption from the confined levels was expected to be approximately an order of magnitude greater than F-K absorption.

Chapter 3

Simulation of Carrier Transport in a *nipi* Superlattice

Simulation is an essential tool for simplifying the development process for a *nipi* solar cell that has a number of potential design variables. Numerous design iterations can be completed simply and with little cost via simulation to gain a general understanding of the interaction between design and device efficiency.

Sentaurus by Synopsys was used as the simulation environment for this characterization. The device can be constructed in a two-dimensional environment where the Poisson and continuity equations are solved self consistently with a finite-element based method. Photon absorption is calculated by a transfer matrix method solver from a user-defined light spectrum and the material's refractive indexes. The drift and diffusion currents are calculated from dark and photo-generated carriers, which can provide a current-voltage (I-V) or EQE curve as an output [44].

Table 3.1: Layer parameters used for the simulation of a baseline *pin* solar cell

	Thickness (nm)	Doping (/cm^3)	Doping Type
Top Window	50	2x10^{18}	*p-type*
Emitter	500	2x10^{18}	*p-type*
Intrinsic	100	5x10^{15}	*n-type*
Base	2000	1x10^{17}	*n-type*
Back Window	500	2x10^{18}	*n-type*

3.1 SIMULATION ENVIRONMENT & BASELINE

Initial simulations were completed comparing a baseline single-junction device against simulation in order to validate the design approach. The baseline structure used is a *pin* solar cell design that has been well characterized experimentally. The structure has been grown and fabricated numerous times, with similar results, making it an excellent benchmark for evaluating the simulation approach[27, 28].

The device simulated consists of five $InGaP_2$ and GaAs layers, a GaAs emitter, intrinsic and base regions as well as $InGaP_2$ top and bottom windows. The doping and layer thickness used in the simulation are shown in Table 3.1. The intrinsic layer is unintentionally doped (UID), which has been measured experimentally at 5x10^{15} /cm^3 *n-type*. No anti-reflection coating (ARC) layer was used on the experimental solar cell or the simulation.

Light bias can be applied to photo-excite carriers and achieve light I-V curves for a given spectrum. A monochromatic light source can be used to determine the spectral response of a solar cell and calculate the EQE. The physical parameters of the semiconductors used in the simulation can be modified to fit the experimental data. Data taken from texts provided the starting point for the GaAs and $InGaP_2$ material parameters [45], which were allowed to float to have the simulated curves fit the experimental results. The refractive index (n) and extinction coefficients (k) were measured on a Woolam variable angle spectroscopic ellipsometer, and entered into the parameter file. The n and k data for GaAs matched

Table 3.2: Material parameters for GaAs and InGaP used in the *Sentaurus* simulation environment

Parameter	GaAs	InGaP	Units
Bandgap	1.42248	1.85	eV
Bandgap Narrowing Parameters	Levinshtein [45]	Levinshtein [45]	
Radiative Recombination Coefficient	1x10^{-10}	1.77x10^{-9}	cm^3/s
SRH Model	$\tau = \dfrac{\tau_{max}}{1 + N/N_{ref}}$		s
SRH Recombination minority electron τ_{max}	5x10^{-9}	5.3x10-8	s
SRH Recombination minority hole τ_{max}	2x10^{-7}	1.96x10^{-6}	s
SRH N$_{ref}$	1x10^{16}	1x10^{16}	/cm^3
Relative Permittivity	12.91	11.772	
Mobility Model	$\mu = \dfrac{\mu_{max} - \mu_{min}}{1 + (N/N_{ref})^{exp}}$	$\mu = \mu_{max}$	cm^2/(Vs)
n-type Max Mobility	9.4x10^3	2.722x10^3	cm^2/(Vs)
p-type Max Mobility	4.915x10^2	1.74x10^2	cm^2/(Vs)
n-type Min Mobility	5x10^2	n/a	cm^2/(Vs)
p-type Min Mobility	20	n/a	cm^2/(Vs)
n-type Mobility N$_{ref}$	6x10^{16}	n/a	/cm^3
p-type Mobility N$_{ref}$	1.48x10^{17}	n/a	/cm^3
n-type Mobility exp	0.394	n/a	
p-type Mobility exp	0.38	n/a	
Recombination velocity GaAs/InGaP$_2$	1x10^4		cm/s

literature values very closely; however, the InGaP$_2$ values did diverge from literature because of changes in the ordering of the ternary semiconductor which can modify the bandgap [46].

The material parameters that resulted in a good fit to experimental one-sun AM0 I-V and EQE results are shown in Table 3.2. Since the Shockley-Read-Hall (SRH) and radiative recombination coefficients are highly dependent upon material quality, they are the most likely parameters to deviate from textbook values. The GaAs SRH lifetime component was modified to have a minority carrier electron lifetime of 5x10^{-9} s, while the hole minority carrier lifetime was fit at 2x10^{-7} s, both of which are within an order of magnitude of literature values [45]. Radiative recombination coefficients from literature fit the experimental results well, so the coefficient of 1x10^{10} cm^3/s was used [45]. An interface recombination velocity of 1x10^4 cm/s was added between the InGaP and GaAs layers to simulate the effect of trap states at the interface which is reasonable according to literature [47]. Additionally the carrier generation

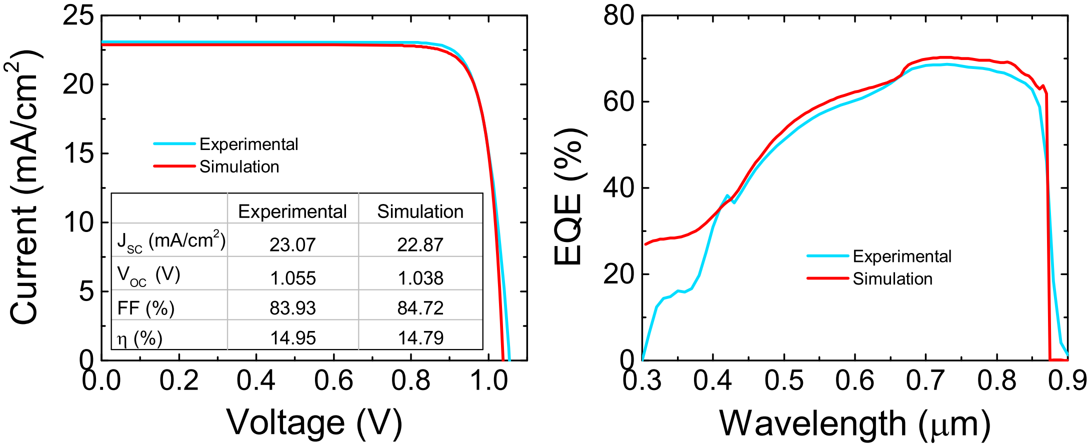

	Experimental	Simulation
J_{SC} (mA/cm^2)	23.07	22.87
V_{OC} (V)	1.055	1.038
FF (%)	83.93	84.72
η (%)	14.95	14.79

Figure 3.1: Experimental and simulated (a) current-voltage and (b) external quantum efficiency curves for a baseline *pin* design.

efficiency was reduced to 50% in the top window layer to simulate the surface recombination loss at the top of the InGaP window layer.

The resultant one-sun AM0 I-V and EQE curves are plotted in Figure 3.1, which shows a very close fit for each curve. The percent error for each metric is 0.87%, 1.61%, 0.94% and 1.07% for short-circuit current density (J_{SC}), V_{OC}, fill factor (FF) and efficiency, respectively. The error in the fit between experimental and simulation is in the range of the experimental error of the solar simulator. Additionally, the experimental EQE curve shows a lower spectral response between 300 and 400 nm than the simulated curve, which is due to error in the measured quantum efficiency at those wavelengths due to low light intensity of the measurement tool. The V_{OC} of the simulated solar cell is slightly lower than the experimental measurement. This could be modified by adjusting the bandgap narrowing parameter, or further fine-tuning the SRH and radiative recombination values.

3.2 SIMULATION OF *NIPI* SOLAR CELLS

The *Sentaurus* simulation environment was used to predict the efficiency of a *nipi* device fabricated with epitaxial regrowth contacts. The corresponding experimental devices are described in Section 4.1. The

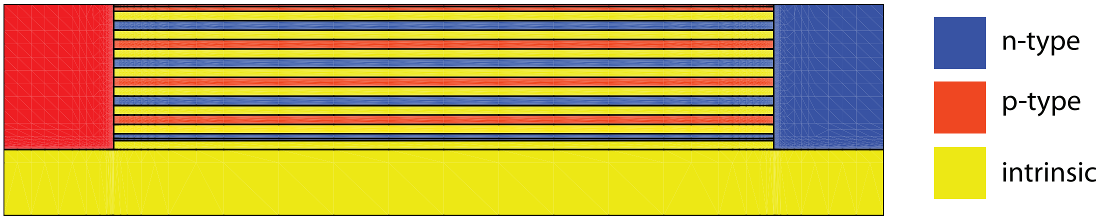

Figure 3.2: The device structure generated by *Sentaurus* used for the simulation of a *nipi* device

solar cells have epitaxially grown SL layers that are etched to expose the side-walls of the SL. Doped GaAs is regrown into the etched trenches with *n-type* GaAs on one side and *p-type* GaAs on the opposite side of the SL and depicted in Figure 3.2. No ARC was applied to the solar cell since the intent was to gain greater understanding of the effect of design changes, ARC would be applied to increase the absolute efficiency of the device after the design has been optimized.

The parameter files used to fit the single-junction device were then used in a *nipi* SL device that was also constructed in *Sentaurus*. The SL was formed on an intrinsic substrate, surrounded top and bottom by InGaP windows, and contacted on either side by regions of *n-* and *p-type* GaAs for the contacts. A representation of the solar cell that was built using *Sentaurus* is depicted in Figure 3.2, where the colors designate the different doping types and densities. The simulated design used vertical sidewalls for the carrier-selective contacts instead of sloped sidewalls from the v-groove etch. Simulations showed that switching to vertical sidewalls had a negligible effect on the output while considerably decreasing the simulation time. The baseline *nipi* solar cell that was used in the simulation had a doping SL with 12 *nipi* repeats consisting of 50 nm doped or intrinsic layers with intentional doping of 1x10^{18} /cm^3 and unintentional doping of 1x10^{15} /cm^3. Shadowed contact regions were 20 μm wide, with the active region being 180 μm wide. The I-V and EQE curves were simulated using the same method that was used for the single-junction device, with the top window's carrier generation efficiency reduced to 50%.

As with the single-junction device, the simulated one-sun AM0 I-V and EQE are compared against the fabricated device results, which are shown in Figure 3.3. The simulated EQE curve shows a relatively

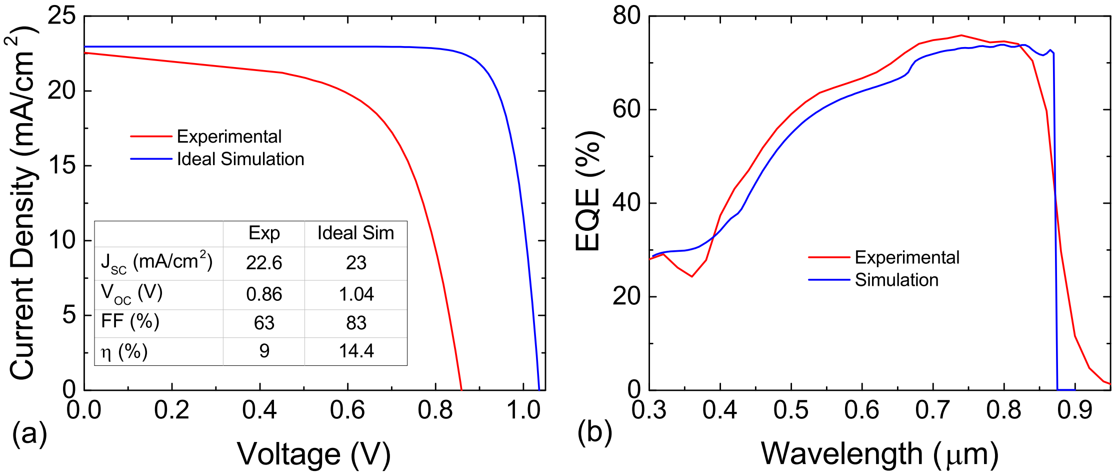

	Exp	Ideal Sim
J_{SC} (mA/cm^2)	22.6	23
V_{OC} (V)	0.86	1.04
FF (%)	63	83
η (%)	9	14.4

Figure 3.3: Experimental and simulated (a) current-voltage and (b) external quantum efficiency curves for a baseline *nipi* design. The I-V curve has both ideal and degraded simulation results.

close match to the experimental result through the entire wavelength range. The simulated curve does have a higher band edge response, and a lower response at wavelengths below 800 nm. It is likely that the shadowing factor is too high in the simulated EQE curve, which would reduce the EQE throughout the spectrum. The simulation does not take into account thermal broadening at the band edge, which results in a cut-off in the EQE curve at the band edge, and the absorption due to the Franz-Keldysk effect and confined level overlap discussed in Section 2.3 was not accounted for in the simulation. To make a comparison, the EQE at 600 nm for the *pin* experimental and simulated measurements are 60.3% and 62.2%, respectively, while the *nipi* experimental and simulated EQE were 66.7% and 63.9%. A significant increase is seen in the *nipi* EQE when compared to the *pin* EQE in both the simulation and experimental results due to reduced diffusion length requirements in the *nipi* device discussed in Section 2.1.

Although the simulated EQE was not a perfect match to experimental results, the one-sun J_{SC} simulation is only 1.8% increase when compared to experimental. The larger concern comes when comparing the FF and V_{OC}, for which the simulation is 20.9% and 31.7% high respectively when compared to experiment. The reason for this will be discussed in greater detail in Section 4.1, and evaluated via simulation in the following section. In general the lower V_{OC} is caused by trap states at the interface between the regrown contact and the doping SL. The simulation has a much higher shunt resistance of 2.7 MΩ than the experimental measurement of 3.3 kΩ, which has a direct impact on FF. The simulated FF is reduced in the simulation with interface traps; however, the simulated shunt path is still too small. It seems that interface traps are not the best means by which to simulate the shunt in a *nipi* device, and better fitting is still required.

The simulation design was also modified to simulate the diffused junction contact solar cell described in Section 4.2. For this device the carrier-selective contacts are formed by diffusing dopants into the sidewalls of the v-groove edges to compensate the *nipi* SL. The simulation of these structures was completed by removing the lateral GaAs contacts described above and overlaying either an *n-* or *p-type* profile that extends into the device from the edge of the v-groove edge. A Gaussian profile was placed with the center of the profile on the edge of the v-groove/air interface, with the peak concentration, decayed concentration, and position of decayed concentration set to 10^{20} /cm^3, 10^{17} /cm^3 and 0.75 μm for the zinc profile and 10^{19} /cm^3, 10^{17} /cm^3 and 1.0 μm for the tin profile to approximate the diffusion profile shown in Figure 4.11. Additional simulation results for the diffused junction design will be presented in Section 5.2.

3.2.1 Simulation of Trap States in *nipi* Solar Cells

Experimental one sun AM0 measurements are shown in Figure 3.4, where they are compared to simulations of an identical device design. Simulations with an ideal regrowth interface show a V_{OC} that is 177 mV higher than the experimental measurement. The reduction in voltage in the experimental device is believed to be due to interface traps that form between the epitaxial regrown contacts and the doping SL at the edge of the etched v-groove. Traps at the rectifying contacts result in charge generation centers, increasing the dark current sources in the device.

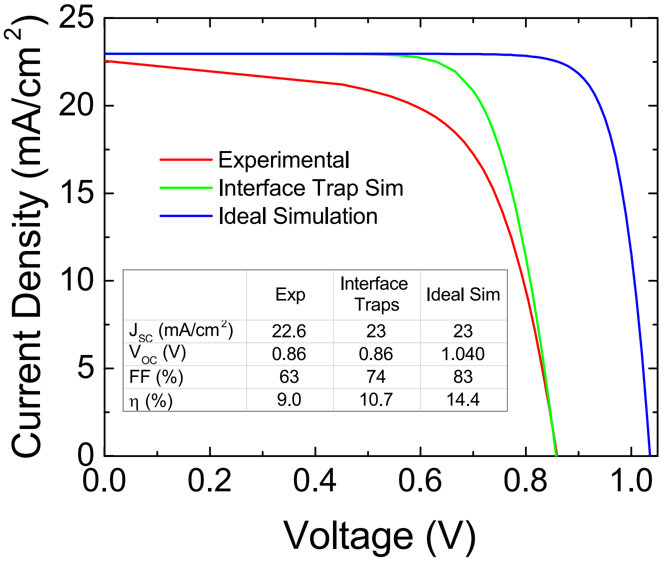

	Exp	Interface Traps	Ideal Sim
J_{SC} (mA/cm^2)	22.6	23	23
V_{OC} (V)	0.86	0.86	1.040
FF (%)	63	74	83
η (%)	9.0	10.7	14.4

Figure 3.4: Current-voltage plot of the highest efficiency *nipi* device compared to simulations with both an ideal interface and traps located at the regrowth interface.

Mid-gap trap states were introduced into the device simulation between the SL and contact semiconductor. The capture cross-section was 7.3x10^{-13} /cm^2 [48], and the trap density was varied to simulate I-V curves. The best fit for V_{OC} was found at a trap density of 1.3x10^{13} /cm^2 with a matched voltage of 0.86 V. Short-circuit current was closely matched between both simulations at 22.96 mA/cm^2 and the experimental result at 22.58 mA/cm^2 due to the efficient and complete collection of carriers in the solar cell. The largest loss in current is due to grid finger shadowing, which was able to be matched between the experimental and simulation results; however, the bus bar shadowing was not accounted for in the simulation which would explain the slight difference.

The simulated FF is higher than the experimental measurements, and the simulation with interface traps does not significantly improve the fit with respect to FF which is 10% higher than experimental measurements. The experimental I-V curve has a reduced current at low voltage, which is indicative of a low resistance shunt path. The experimental devices' shunt resistance was measured at 1345 Ω, while the simulated shunt resistance was 7.16 MΩ with traps, which is less than a factor of two difference from the ideal case of 15.4 MΩ. A possible explanation for the decreased shunt resistance in the experimental

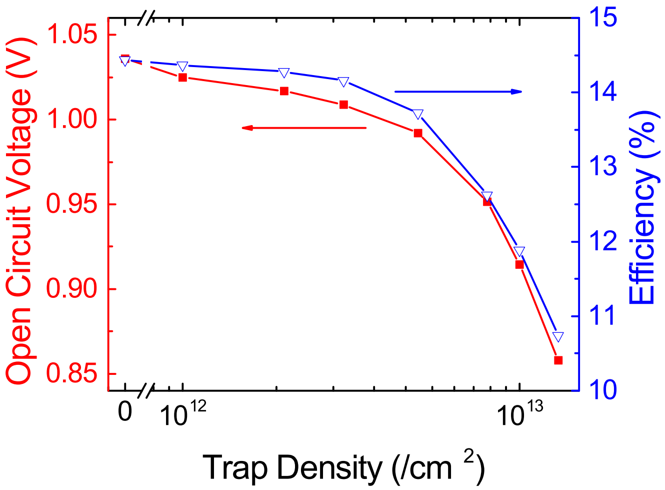

Figure 3.5: Plot of V_{OC} and efficiency versus interface trap density for a *nipi* solar cell.

device is unpassivated bonds on the perimeter of the device. This would results in a lower resistance shunt path in the *nipi* device than a conventional solar cell due to the short distance between each of the 25 parallel diodes in the *nipi* device. Further characterization of the shunt path will be discussed in Section 5.1.3.

In an effort to evaluate the interface trap levels in a *nipi* solar cell, simulations were completed with interface trap densities between 1x10^{12} and the experimental fit of 1.3x10^{13} /cm^2. Efficiency and V_{OC} were measured from the simulations and are plotted in Figure 3.5. A decrease in V_{OC} was the main factor in decreasing efficiency as the trap density was increased while there was a slight reduction in FF and no change in J_{SC}. A maximum efficiency of 14.44% was simulated for an ideal device, which is a 60.4% increase from the 9.0% efficient device that has been experimentally realized. An ideal interface is not necessarily achievable or required as simulations with a trap density of 1x10^{12} /cm^2 have a negligible decrease in efficiency of 0.07% absolute from simulations with ideal interfaces. This demonstrates the ability to significantly improve efficiency by reducing the interface trap density by an order of magnitude.

3.3 A MODIFIED *NIPI* DIODE MODEL

In order to model a doping SL solar cell a modification to the conventional single and multi junction solar cell theory must be made. The *nipi* solar cell has multiple homojunctions formed in a parallel arrangement, where the total current is the sum of each parallel-connected diode (PCD). The conventional single diode model in (3.1) can be modified to be a sum of each PCD, n as shown in (3.2). In addition to the two diode terms a third term that accounts for the regrowth interface is added, as depicted in Figure 2.6 (b). The terms $I_{0_{int}}$ and n_{int} describe the dark saturation and ideality for the regrowth interface. Since the diode equation accounts for the entire planar surface of the solar cell a modifier term CDr is multiplied to the regrowth interface terms, which is the ratio of the total planar diode area to the total regrowth interface area.

$$I = i_0 * e^{\left(\frac{V - I*R_s}{nkT} - 1\right)} \tag{3.1}$$

$$\begin{aligned} I = \sum_{i=1}^{n} i_{01} * e^{\left(\frac{V - I_n*R_s}{n_1 kT} - 1\right)} + i_{02} * e^{\left(\frac{V - I_n*R_s}{n_2 kT} - 1\right)} + CDr * I_{0_{int}} * e^{\left(\frac{v - I_n R_s}{n_{int} kT} - 1\right)} \\ + \frac{v - I_n R_s}{R_{sh} + CDr * R_{sh_{int}}} - I_{gen_n} \end{aligned} \tag{3.2}$$

The regrowth interface is populated by trap states, which can be filled as the excess carriers at the interface are increased. In order to properly characterize the interface, the dark saturation current has to be calculated as a function of excess carrier concentration. Theory developed by Sah [49] creates the link between dark saturation current and lifetime

$$i_0 = \frac{q n_i W_d}{\sqrt{\tau_p \tau_n}} * f(b) \tag{3.3}$$

where n_i is the intrinsic carrier concentration, W_d is the depletion width and

$$f(b) = \int_{z1}^{z2} \frac{dz}{z^2 + 2bz + 1} \tag{3.4}$$

and

$$b = e^{\left(-\dfrac{(\phi_p - \phi_n)q}{2kT}\right)} cosh\left[\frac{E_t - E_i}{kT} + \frac{1}{2} ln\left(\frac{\tau_{po}}{\tau_{no}}\right)\right] \tag{3.5}$$

and

$$z = \sqrt{\frac{\tau_p}{\tau_n}} * e^{\left(\dfrac{(\Psi_D(x) - \phi_p + \phi_n)q}{2kT}\right)}; \quad z_1 = z(-x_1); \quad z_2 = z(x_2) \tag{3.6}$$

when $\phi_p - \phi_n$ is assumed to be the junction voltage and $\psi_n - \psi_p = \psi_D - V_j$ where V_j is the junction voltage and ψ_D is the built-in potential [50]. The limits can also be assumed to extend to zero and infinity. Further, E_t is the energy level of the trap state, and E_i is the intrinsic Fermi level.

The minority carrier lifetimes τ_n and τ_p can be calculated by solving (3.7) following the calculation of excess carrier concentration Δn and Δp in (3.8). This theory was initially developed by Shockley [51] and further refined by Blakemore [52] and Brancus [53] to allow for both high trap density and high excess carrier concentration which was not allowed in the development by Shockley.

$$\begin{aligned} \tau_n &= \frac{\tau_{po}(n_o + n_1 + \Delta n) + \tau_{no}(p_o + p_1 + \Delta p) + \tau_{no} N_t \left[\dfrac{p_1}{p_o + p_1} + \dfrac{\Delta p - \Delta n}{N_t}\right]}{(n_o + p_o + \Delta n) + N_t\left[\dfrac{p_o(n_o + \Delta n)}{(n_o + n_1 \Delta n)(p_o + p_1)}\right]} \\ \tau_p &= \frac{\tau_{po}(n_o + n_1 + \Delta n) + \tau_{no}(p_o + p_1 + \Delta p) + \tau_{po} N_t \left[\dfrac{n_1}{n_o + n_1} + \dfrac{\Delta n - \Delta p}{N_t}\right]}{(n_o + p_o + \Delta p) + N_t\left[\dfrac{n_o(p_o + \Delta p)}{(p_o + p_1 \Delta p)(n_o + n_1)}\right]} \end{aligned} \tag{3.7}$$

The calculation of minority carrier lifetime is dependent upon the density of electrons n_o and holes p_o in an unmodulated sample in the conduction and valence bands; respectively, and also upon the electron n_1 and hole p_1 populations if the trap energy E_f is equivalent to the Fermi level E_i. If the energies are separate the density can be calculated by $n_1 = n_i * exp[(E_t - E_i)/kT]$ and $p_1 = n_i * exp[(E_i - E_t)/kT]$. Additionally τ_{no} and τ_{po} are the unmodulated lifetimes in the *n-* and *p-type* doped regions and N_t is the trap density for the material. In order to calculate lifetimes the excess carrier concentration must be solved according to the following equation:

$$\Delta n = \sqrt{\frac{1}{4}\left[A + \Delta p(k+1)\right]^2 - \Delta p * N_t\left(\frac{p_o - kp_1}{p_o + p_1}\right)} - \frac{1}{2}\left[A + \Delta p(k+1)\right] \tag{3.8}$$

where k is defined as τ_{no}/τ_{po} and

$$A = \frac{N_t p_o}{p_o + p_1} + k(p_o + p_1) + n_o + n_1 \tag{3.9}$$

Given the calculation of excess carrier concentration and lifetime, the generated carriers can be solved for in (3.10). In order to determine a lifetime based upon a carrier generation rate due to solar flux an initial Δp must be assumed to calculate Δn which can then be used to calculate both τ_n and g_e. The initial Δp assumption must be modified until the calculated g_e matches carrier generation expected from the incident solar flux.

$$\begin{aligned} g_e &= \frac{\Delta n}{\tau_n} = \frac{1}{\tau_{no}}\left[\frac{(n_o + n_1 + \Delta n) * (\Delta n - \Delta p)}{N_t} + \frac{\Delta n * n_1}{n_o + n_1}\right] \\ &= \frac{\Delta p}{\tau_p} = \frac{1}{\tau_{po}}\left[\frac{(p_o + p_1 + \Delta p) * (\Delta p - \Delta n)}{N_t} + \frac{\Delta p * p_1}{p_o + p_1}\right] \end{aligned} \tag{3.10}$$

The integration of the lifetime calculation with respect to solar flux allows a lifetime to be calculated as a function of *nipi* repeat period n. Lifetime and dark saturation currents are calculated for each PCD

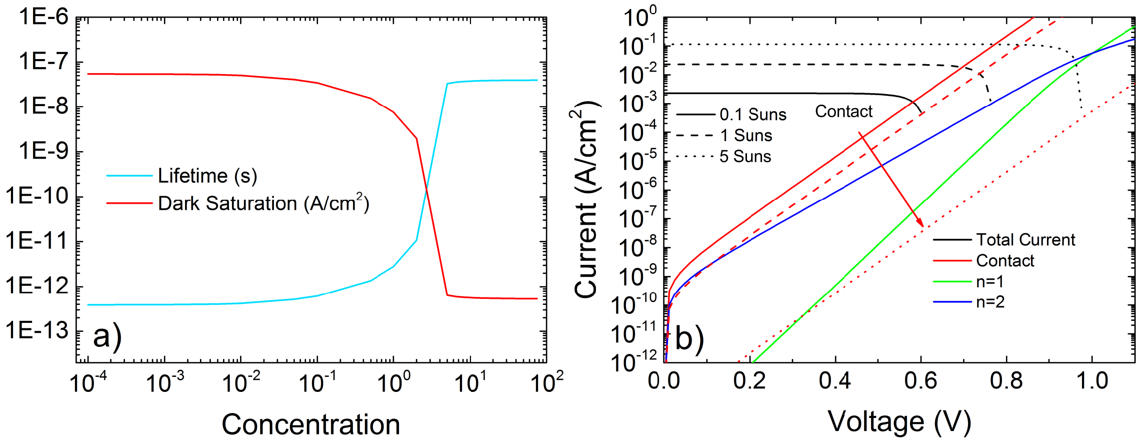

Figure 3.6: Graph of the (a) relationship between solar concentration, lifetime and dark saturation current for a 25 repeat *nipi* solar cell and (b) the contributions from each current component (contact, n=1, and n=2) and the total current for three concentration levels.

as a function of flux, and then each of the separate diode terms is summed as described in (3.2). The result is an increase in lifetime and a decrease in dark saturation current for the PCD closer to the top of the device as the solar flux is increased. Concentration is the multiplier of AM1.5G flux needed to determine the total flux, and the average lifetime and I_o for all of the PCD layers as a function of concentration is plotted in Figure 3.6 (a).

Applying the calculation of dark saturation current to the summed triple diode (3.2) we would expect to see a reduction in dark current and an improvement in V_{OC} as the concentration is increased past the point in which recovery in lifetime is seen. Figure 3.6 (b) shows the calculation of the current components described in (3.2). The $n = 1$ and $n = 2$ terms remain constant for the different concentration levels because no traps were assumed in the bulk. The contact term shows a significant reduction in dark current as the concentration is increased from 0.1 to 5 suns, which results in a corresponding improvement in V_{OC} greater than the expected logarithmic trend. Although the total regrowth interface area is smaller than the surface area of the cell, the current is plotted relative to the surface area of the solar cell by multiplying it by the CDr factor to make the currents comparable.

For the calculations shown the fitting terms were modified to fit experimental results from a *nipi* solar cell measured under concentration. The initial lifetimes were found to be 3x10^{-12} seconds for τ_{po} and 1x10^{-6} for τ_{no}. The trap density N_t was found to be 4x10^{14} /cm^3 and the trap energy E_t was matched to the Fermi level at half the GaAs bandgap of 0.72 eV.

Evaluating the calculation of dark saturation current it is seen that a significant improvement is seen at concentrations between 0.1 and 10 suns, improving the dark saturation current multiple orders of magnitude. The improvement is due to the filling of trap states which allows the lifetime to return to a state similar to that of no traps. The results of this modeling will be discussed in greater detail and compared to experimental measurements in Section 5.1.4.

3.4 CONCLUSIONS

This chapter evaluated the methods for simulating and modeling *nipi* solar cells. Initial characterization was completed by comparing conventional *pin* devices to simulation, where a fit with only 1.07% error in efficiency was achieved. The material parameters developed were then used for was used to develop a simulation routine in *Sentaurus* to evaluate a *nipi* solar cell. The simulation showed an expected efficiency of 14.4% without ARC, however this is an error of 60% when compared to the experimental measurement of 9.0% efficiency. Simulated J_{SC} was closely matched to experimental, however V_{OC} and FF were simulated to be higher than the experimental results. Improvements in V_{OC} were achieved by including trap states at the epitaxial regrowth interface, which eliminated the error in V_{OC}.

A model was also developed to characterize the effect of carrier concentration in the *nipi* solar cell at the regrowth interface on carrier lifetime. The ideal diode equation was modified by calculating the i_o term by calculating lifetime at the regrown interface. Lifetime is determined as a function of carrier concentration, which in turn is related to solar concentration. The end result is a model that relates a modeled I-V curve with solar concentration. With specific trap densities and energies assumed at the regrowth interface an improvement in lifetime and V_{OC} was calculated to occur at concentrations between 1 and 10 suns. After the improvement in lifetime the regrowth interface term which dominates the dark current at low concentrations becomes insignificant at higher concentrations.

Chapter 4

The Development of a Fabrication Process for *nipi* Solar Cells

The fabrication process required to realize an experimental *nipi* solar cell is more complex and challenging than for a conventional design, requiring a significant effort to optimize. Schematic depictions of the device structure for conventional devices, and four different *nipi* designs are shown in Figure 4.1. The schematic representation of *nipi* solar cells demonstrate the increased complexity of the fabrication process with the additional interfaces and layers in the design, which translates to an increased need to fine tune the fabrication process.

A summary of the fabrication process, processing characterization, and device test results will be discussed in this chapter. The work entailed within these sections is a significant portion of the work done in this thesis.

Five distinct methods have been proposed to fabricate a doping SL *nipi* solar cell. Each method requires the growth of the initial doping SL, with alternating *n-* and *p-type* doping, with or without an intrinsic layer between the doped layers. The device cannot be contacted with the traditional front and

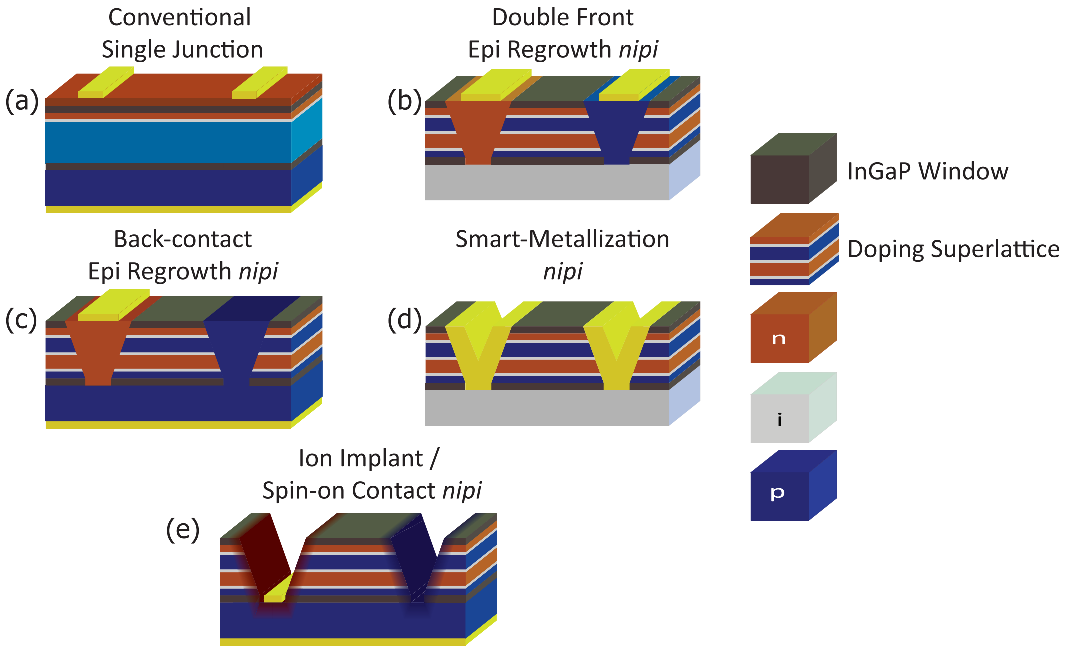

Figure 4.1: Schematic diagram of multiple solar cell designs, with (a) conventional single-junction, (b) double front contact nipi, (c) single front contact *nipi* (back contact), (d) smart metalization *nipi*, and (e) ion implanted or diffused junction *nipi* designs all depicted. Colors signify dopant and material type as shown in the key on the right, darker colors signify higher dopant incorporation.

back-side contacts of a solar cell because charge would become trapped in the potential wells that are formed in the SL shown in Figure 2.3. Due to this restriction, a novel contacting mechanism is required in which current is collected laterally. In order to achieve this, a contacting method that is selectively ohmic and rectifying to the opposing sides of each doped layer is required.

The first method consists of the epitaxial regrowth of doped GaAs into v-grooves etched in the doping SL as shown in Figure 4.1 (b). Regrown material contacts the *nipi* layers, and naturally forms ohmic and rectifying contacts. This method can be done with the same material as the initial SL, or with a higher bandgap material to improve the rectifying junction. Another method is a smart metalization approach that forms Schottky tunnel contact and Schottky barriers on opposing sides of the doped layers as depicted in Figure 4.1(d). Prior work completed with this method used a Ge/Au/Ni/Au metalization for the *n-type* ohmic (*p-type* rectifying) contact, and an Au/Zn/Au stack for the opposing *p-type* ohmic (*n-type* rectifying) contact [14] although other metalizations are possible. The third method is to form *n*-

and *p-type* regions in the doping SL through ion implantation. This process can be done with implants at multiple energies to compensate the entire thickness of the active *nipi* layers [54], or with a low energy implant into an etched v-groove as shown in Figure 4.1 (e). Low energy implants of *n-* and *p-type* dopants would form alternating ohmic contacts and rectifying barriers to the dopant layers. Another method depicted in Figure 4.1 (e) is similar to ion implantation, but uses a diffusion source to form the carrier-selective contacts along the sidewalls of an etched v-groove. This can be done by using a spin-on glass (SOG) dopant source that is annealed to drive in the dopant. Lastly, a shadow mask technique has been used for molecular beam epitaxy (MBE) grown devices [55]. This is an in-situ process that uses the off-axis orientation of dopant sources in an MBE chamber to selectively block either the *n-* or *p-type* dopant from a region of the SL. This results in selectively *p-* and *n-type* regions near the end of each *nipi* region which can be contacted with the appropriate metalization. Each of the methods proposed can be contacted with both contacts on the front side of the device. Alternatively all of the designs except for smart metalization can be contacted on the back side as shown in Figure 4.1 (c).

Although the smart metalization, shadow mask technique and ion implantation devices are simpler to fabricate, the epitaxial regrowth method has been predominantly used to form the contacts for this work. Epitaxial regrown contacts allow a tremendous amount of flexibility and control of the carrier-selective interface with formation of a step function interface where the regrowth can have the doping and composition tailored to optimize the device. We have investigated the use of ion implantation and diffused junctions contacts, and it is believed there is potential for both designs. Ion implantation presents the possibility that doses high enough to counter-dope the GaAs SL will amorphize the semiconductor. However, work has been done to reach high dopant concentrations with minimal lasting crystal damage [56]. Diffused junctions are challenging to use to counter-dope the SL, and very little literature exists on *n-type* diffused junctions in GaAs. Both ion implantation and diffused junctions present a benefit when compared to epitaxial regrowth because they do not have an interface that is exposed to the environment as in the regrown process. The shadow mask technique will not be studied due to the use of a MOVPE reactor instead of an MBE reactor for this growth. Finally the smart metalization process will not be evaluated due to the decreased likelihood of finding a two-metalization scheme that forms the required carrier-selective contacts. Work completed previously by Cress *et. al.* showed that the work functions of the metalizations used resulted in a Schottky ohmic and a poor Schottky rectifying contact that allowed leakage currents at the selective barrier [14].

4.1 FORMATION OF CONTACTS BY EPITAXIAL REGROWTH

The base doping SL structures for this work were grown in a Veeco D125LDM rotating disk MOVPE reactor. The *nipi* layers were grown with TMGa and AsH_3 precursors, and doping was achieved with disilane (Si_2H_6) or diethylzinc (DEZn) for the *n-* or *p-type* doped layers, respectively, at a concentration of approximately 1×10^{18} /cm^3. The intrinsic layers were unintentionally doped with a background doping level of 1×10^{15} /cm^3 as determined by capacitance-voltage measurements on unintentionally doped test structures. $InGaP_2$ windows were grown as front and back surface fields for the SL to reduce surface recombination. All the growths completed were on (100) oriented substrates offcut 2° to the $<110>$ direction, this offcut was selected to improve the ordering of the $InGaP_2$ layers [46]. The growth parameters for the reactor are given in Table 4.1.

Lateral contacts are formed by initially growing a 200 nm SiO_2 film using tetraethylorthosilicate (TEOS) plasma enhanced chemical vapor deposition at 390°C. The grid finger layout with grid finger spacings of 50, 100, 200 and 500 μm is then patterned in Shipley 1813 photoresist with a mask aligner. The oxide is then patterned by etching in a 10:1 buffered hydrofluoric acid (BOE) to water mixture, shown in Fig 4.2 (b), forming a hard mask for the crystallographic GaAs v-groove etch, as well as providing a self-aligned selective epitaxial regrowth mask for the first contact. The crystallographic

Table 4.1: Growth parameters for the OMVPE growth of the *nipi* superlattice

Parameter	Value
Temperature	620°C
Chamber Pressure	60 Torr
Rotational Speed	1000 RPM
V/III	35.4
GaAs Growth Rate	2 μm/hr
TMGa Partial Pressure	6.54 mTorr
AsH_3 Partial Pressure	230 mTorr
Si_2H_6 Partial Pressure	924 μTorr
DEZn Partial Pressure	166 μTorr

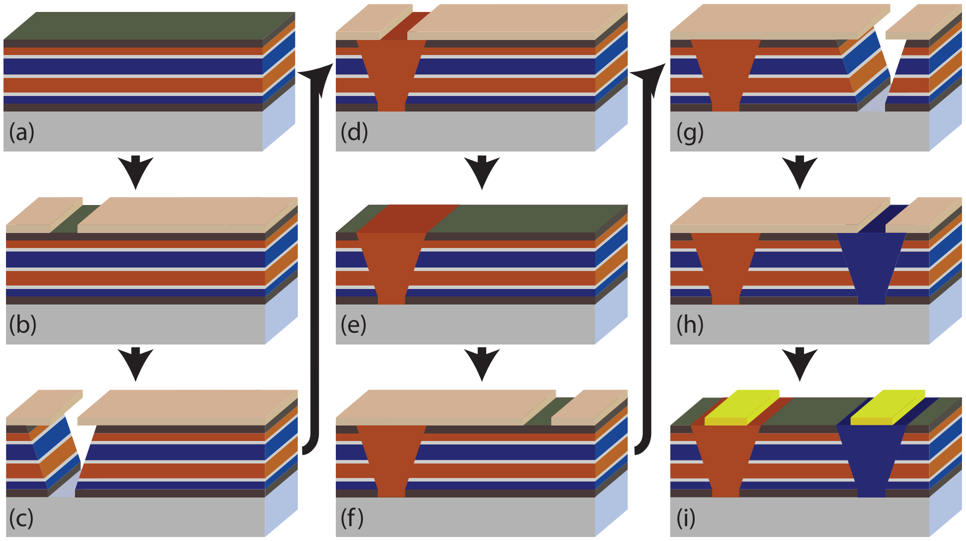

Figure 4.2: Depiction of process flow for the *nipi* device. (a) shows the initial SL growth, (b) is following deposition of SiO_2 and lithographic patterning, (c) depicts the crystallographic etch in the *nipi* layers, (d) is following the first regrowth, (e,f,g, and h) are repeating the same steps for the second regrowth, and (i) shows the device after metalization.

Figure 4.3: SEM image of an etched v-groove , demonstrating the crystallographic etch performed with a nitride hard mask

v-groove etch in concentrated sulfuric acid (95%) and hydrogen peroxide (30%) and water (4:1:5) [57] is completed as depicted in Fig. 4.2 (c). The etch preferentially etches the As-terminated (100) plane instead of the Ga-terminated (111)A and $(1\bar{1}\ \bar{1})$A planes. This crystallographic selectivity results in an etch that exposes the (111)A and $(1\bar{1}\ \bar{1})$A planes along the v-groove edge, when the (100) plane is the surface of the wafer being etched. The angle between the crystal planes is 54.7° as shown in Figure 4.3, which provides an adequate surface upon which to regrow GaAs. The backside $InGaP_2$ window provides an etch stop for this process, and is then removed in HCl to expose the GaAs surface from which the growth is seeded.

Figure 4.2 (d) shows GaAs regrown in the etched trenches, where it forms ohmic and rectifying junctions with the respective *nipi* layers. The growth conditions matched that of Table 4.1 except for the Si_2H_6 and DEZn partial pressures, which were varied up to 4.15 μTorr for Si_2H_6 and 2.93 mTorr for DEZn to adjust the dopant concentration to a maximum of $6x10^{18}$ $/cm^3$ for both dopants. The regrowth had a nominal thickness of 100 to 150 nm doped GaAs, which results in an increased total thickness in the v-groove trench due to growth-rate enhancement (GRE). The enhancement occurs because the sticking coefficient of the group-III elements is lower on the SiO_2 than GaAs [58]. As the group-III elements adsorb onto the surface of the wafer, they cannot adhere to the SiO_2, so they diffuse until they

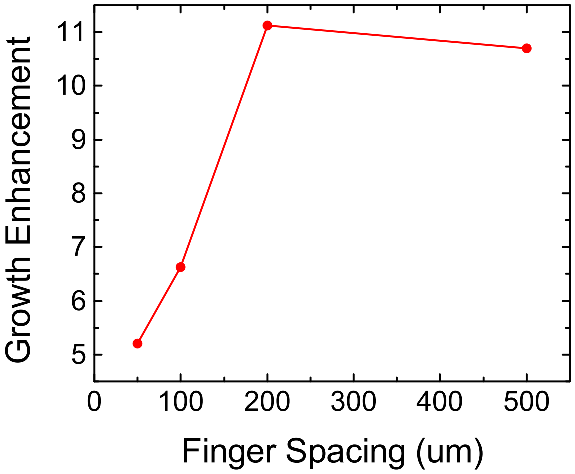

Figure 4.4: Plot of GRE versus grid v-groove spacing, calculated for both the growth along the v-groove edge and in the center of the trench

reach a nucleation site. If the v-groove exists within one diffusion length of the group-III element, it will likely diffuse to that location and thereby increase the growth rate in the v-groove. GRE was evaluated by measuring the actual growth thickness in a v-groove by scanning electron microscope (SEM) and dividing it by the nominal thickness that is calculated from the growth time and nominal growth rate. GRE was calculated as a function of grid finger spacing and is shown in Figure 4.4. The enhancement saturates at wider spacings since adatom diffusion length is less than the widest spacing.

The original SiO_2 layer is removed in BOE following regrowth, another SiO_2 layer is deposited, and the process is repeated to form the second contact with opposite doping as diagramed in Fig. 4.2 (e-h). The *p-type* metalization is completed on the front side by patterning Shipley 1827 resist on top of Microchem LOR-10A lift-off resist prior to evaporating an Au/Zn/Au stack, which is lifted off in Microchem remover PG. After an anneal at 407°C for six minutes the same lift-off process is completed with a Au/Ge/Ni/Au metalization for the *n-type* contact.

The final step is to perform a mesa isolation etch to define the device active areas of 0.125, 0.25, 0.5 and 1 cm^2, where the mask layout is shown in Figure 4.5. Both *n-* and *p-type* probe pads are on the top surface of the device, with the pads on opposing sides of the device as shown in Figure 4.6.

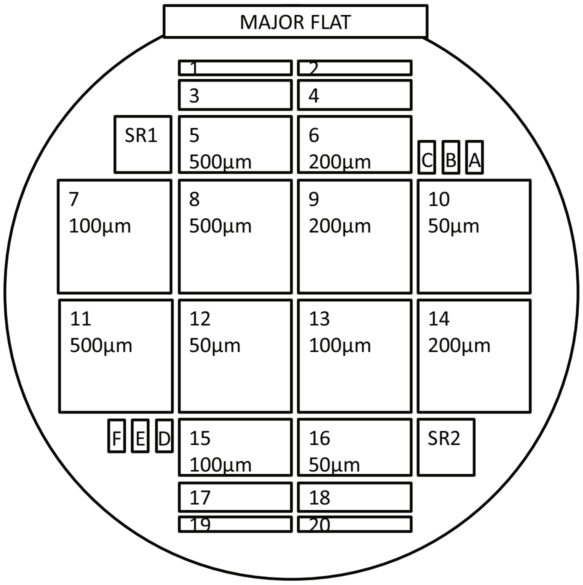

Figure 4.5: A depiction of the mask layout used for the fabrication of *nipi* solar cells. Each rectangle represents a solar cell, with the identifying cell number and the grid finger spacing in each cell. For the smaller area cells the nearest cells in the same column have identical grid finger spacings. Additional devices for measuring quantum efficiency without shadowing (SR1, SR2) and contact resistance (A,B,etc) were included.

Interdigitated v-grooves span the distance between the probe pads, and the width of each groove defined by the mask is 16 μm, which increases to greater than 20 μm during the v-groove etch. No ARC was applied on the device following processing.

4.1.1 Characterization of Fabrication Process Steps for Epitaxial Regrowth

To complete the fabrication process for a device, a number of the steps in the process required characterization. The etch used to achieve the v-groove has been characterized by others, and is well known [57]. The etch chemistry selected was H_2SO_4:H_2O_2:H_2O (4:1:5), which exposes the (111)A and $(1\bar{1}\ \bar{1})$A planes along the v-groove edge, when the (100) plane is the surface of the wafer being etched. The angle between the crystals is 54.7° as shown in Figure 4.3, which provides an adequate surface upon which to regrow GaAs.

In literature the etch rate for the 4:1:5 etch has been found to be 5μm/min, which has also been

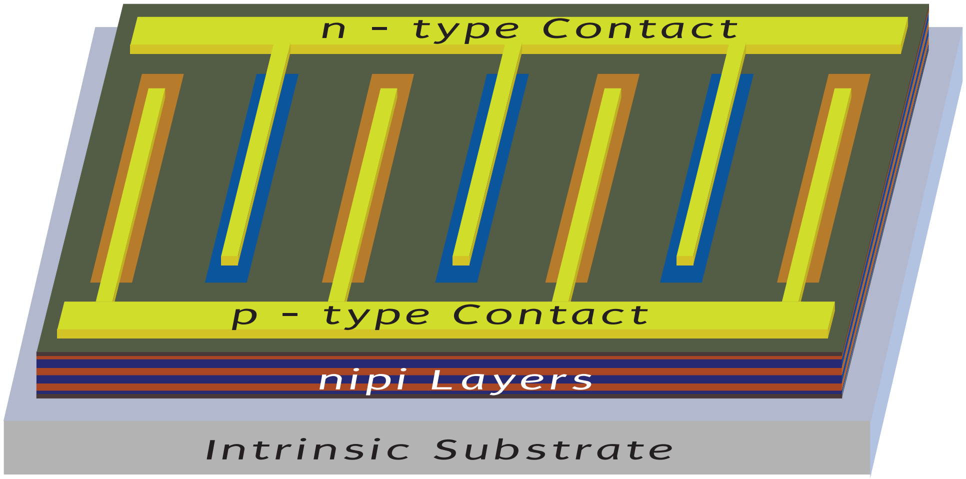

Figure 4.6: A perspective view of a *nipi* solar cell contacted with both *n*- and *p-type* contacts on the front side of the device

characterized in preliminary testing. Since the concentration of H_2O_2 can change with time in the original storage container and in the solution after mixing, it has been noted that the etch rate does vary significantly. Due to variations from as low as 2μm/min to 5μm/min, it is required that the etch rate be characterized prior to any processing with this etchant. However, most devices are designed with an $InGaP_2$ lower window that acts as an etch stop for this process as previously mentioned, minimizing the effects of any over etch.

The subsequent step in the process after the v-groove etch is the epitaxial regrowth completed by MOVPE. Testing was completed to evaluate the regrowth process, characterize the growth rate, and GRE due to the selective nature of the growth. The SiO_2 layer that is deposited on the surface of the wafer does not allow the nucleation of adatoms in the CVD process due to the sticking coefficient of reactant species being much lower on SiO_2 than GaAs [58]. As the group-III elements adsorb onto the surface of the wafer, they cannot adhere to the SiO_2, so they diffuse until they reach a nucleation site. If the v-groove exists within one diffusion length of the group-III element, it will likely diffuse to that location and thereby increase the growth rate in the v-groove. This increase in growth rate within the v-groove is dependent upon the width of the SiO_2 mask, and the v-groove opening. As the mask width

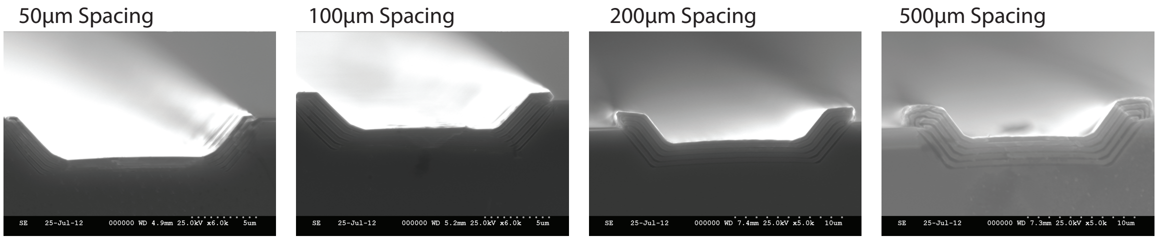

Figure 4.7: SEM micrographs of epitaxial regrowth within the v-grooves that are spaced 50, 100, 200 and 500 μm apart, demonstrating the variation in GRE.

increases, the number of reactants that cannot nucleate on the SiO_2 surface increases, increasing the growth rate in the v-groove . Correspondingly, the narrower the v-groove the same amount of reactants diffuse into a smaller area, which again will increase the growth rate [59].

To be able to target the growth thickness properly, the GRE has to be characterized in order to achieve the desired thickness within the v-groove . Test structures were patterned with SiO_2, which was etched in HF to expose the regrowth areas, and then etched with the 4:1:5 etch prior to regrowth. The pattern that was used had varying spacing between v-grooves of 50, 100, 200 and 500 μm, with the v-groove mask defined width being 16 μm which widens to approximately 20 μm after the v-groove etch. The samples were returned to the MOVPE reactor, where a GaAs/InGaP SL was grown with a nominal growth rate of 2 μm/min. Following regrowth, the total growth was measured for each v-grooves spacing, of which Figure 4.7 displays a SEM micrograph from each v-groove spacing to show the increase in growth rate as the spacing increases. From the actual growth in each v-groove , and the nominal thickness based upon growth time and nominal growth rate, the GRE was calculated and is shown in Figure 4.4. Growth rate enhancement was calculated both along the v-groove edge, and from the center of the trench. For closer finger spacing the enhancement is greater on the v-groove sidewall, but switches for wider spacing. The enhancement also saturates at wider spacings since adatom diffusion length is less than the widest spacing.

In addition to characterization of the GRE, additional testing was required to improve the epitaxial

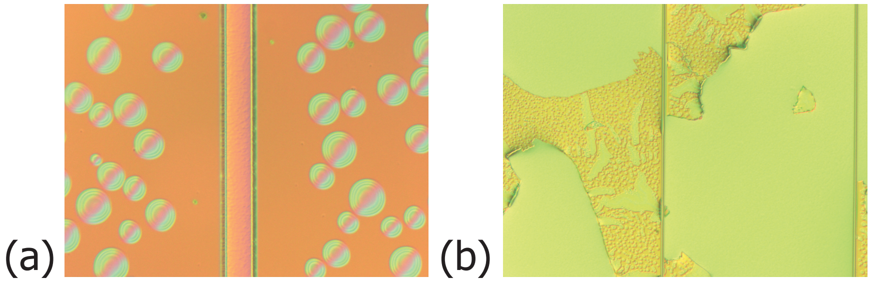

Figure 4.8: Microscope images showing (a) bubbles, and (b) peeling of SiN_x films following epitaxial regrowth testing.

regrowth process. Initial regrowth tests used a SiN_x layer, instead of the SiO_2 layer to promote the selective growth within the v-grooves. Silicon nitride was initially chosen because prior work had been done by a colleague, Dr. David Forbes, which indicated that SiN_x left a smoother GaAs surface following regrowth than a wafer coated with SiO_2 that underwent the same process [60]. A number of the tests completed with SiN_x selective films resulting in bubbling and peeling of the film following regrowth, as shown in Figure 4.8. It is unclear what caused the lifting of the film, although work was done to deposit stress-free films by PECVD. The result was lifting of the SiN_x layer that led to undesired GaAs growth on the surface of the substrate. As a result of these difficulties, the selective film was changed to SiO_2, which has not encountered problems with lifting and peeling.

4.1.2 Process Characterization Related to Fabricated Devices

During initial regrowth testing and the fabrication of the first devices, difficulties were encountered with the nucleation of GaAs on the SiO_2 surface as depicted in Figure 4.9. As discussed previously, the sticking coefficient of the reactants is much lower on SiO_2, but it is not impossible for the reactants to nucleate on the oxide surface. If GaAs nucleates on the oxide surface during a device's first regrowth, it cannot be etched off without removing the regrown GaAs in the v-groove trenches. The result is 1-5 μm tall GaAs islands on the wafer surface as shown in Figure 4.9 (b). When the SiO_2 layer is then deposited for the selective mask of the subsequent regrowth the GaAs islands are not conformally coated, leaving

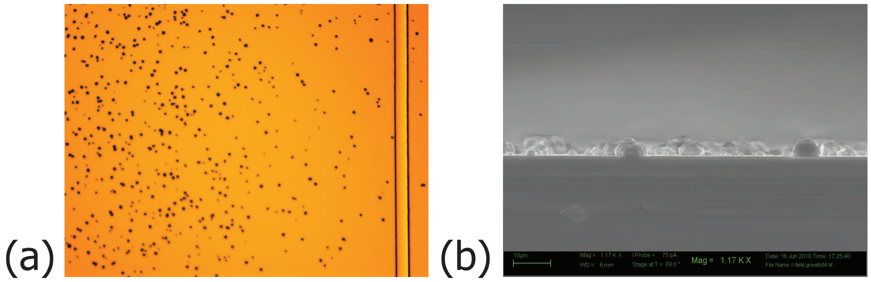

Figure 4.9: Images of GaAs nucleation on the SiO_2 surface, shown in a (a) top down microscope image, and (b) a cross-sectional SEM micrograph.

voids at the bottom through which the 4:1:5 etchant etches the underlying layers and further regrowth occurs.

Due to the problems encountered with GaAs nucleation on the SiO_2 layers, work was done to eliminate this problem. It was found that as long as the growth in the v-grooves does not grow higher than the surface of the v-groove etch, the nucleation on the SiO_2 surface is negligible. When the regrowth fills the v-groove and exceeds the edge, the diffusion of reactants into the v-groove is hindered because of the formation of a barrier, thus making the growth on the oxide surface preferential. As a result, care is taken to ensure that the total growth including GRE is no greater than half the depth of the v-groove etch.

As was shown in Figure 4.1 (c & d) the contacts can be made on either the front side or on both front and back sides of the device. For the devices fabricated with the double top side contact scheme the potential for a short between the contact pads is significantly increased. The mask design used for processing places both probe pads on the top $InGaP_2$ window layer, which provides a resistive shunt path across the device. As a result, an additional processing step and mask layer would be required to isolate the metal probe pads from the $InGaP_2$ window. This could be done by depositing a 100 nm SiO_2 film on the surface after both regrowth processes are complete. The film is lithographically patterned and etched with BOE to leave SiO_2 pads beneath where the metal bus bars will be deposited.

Alternately to the use of an SiO_2 film to isolate the metalization, a revised process has been developed to contact the back side of the device. By switching the substrate from unintentionally doped to *n-type* it is possible to contact the back side of the device and only have one contact on the front side. The *n-type* regrowth forms an ohmic contact to the substrate, while the *p-type* regrowth results in a rectifying contact with the substrate. The *p-type* contacts are made in the same manner described above with the lift-off process. The *n-type* Au/Ge/Ni/Au contacts are then evaporated on the back side of the device while the front side is coated with Shipley 1827 photoresist for protection. A depiction of a solar cell fabricated with this alternate process is shown in Figure 1.3.

4.2 CONTACTS BY DIFFUSED JUNCTION

An alternate method for contacting *nipi* devices is via a diffused junction. The dopant source is a SOG with either zinc or tin as the dopant element for *p-* and *n-type* dopants, respectively. The SOG sources were manufactured by Emulsitone, and the compositional details are confidential; however, they are typically composed of a film source, usually silicic acid ester, dopant salts of stannous chloride for tin, or zinc chloride for zinc, and a solvent. Both dopant sources have been documented extensively for their relatively high diffusivity in GaAs at lower temperatures [61, 62]. Since arsenic becomes mobile in GaAs at temperatures over 570°C it is important to keep the temperature of the diffusion as low as possible.

Devices are fabricated in a very similar manner to the process described previously, the modified process is depicted in Figure 4.10. The only change is that instead of an epitaxial regrowth after the v-groove etch, the SOG is coated onto the surface and a high temperature anneal and drive-in is completed.

To fabricate the devices with diffused contacts the same process described in Section 4.1 was followed for the PECVD growth of the oxide hard mask and the v-groove etch. The tin source can damage

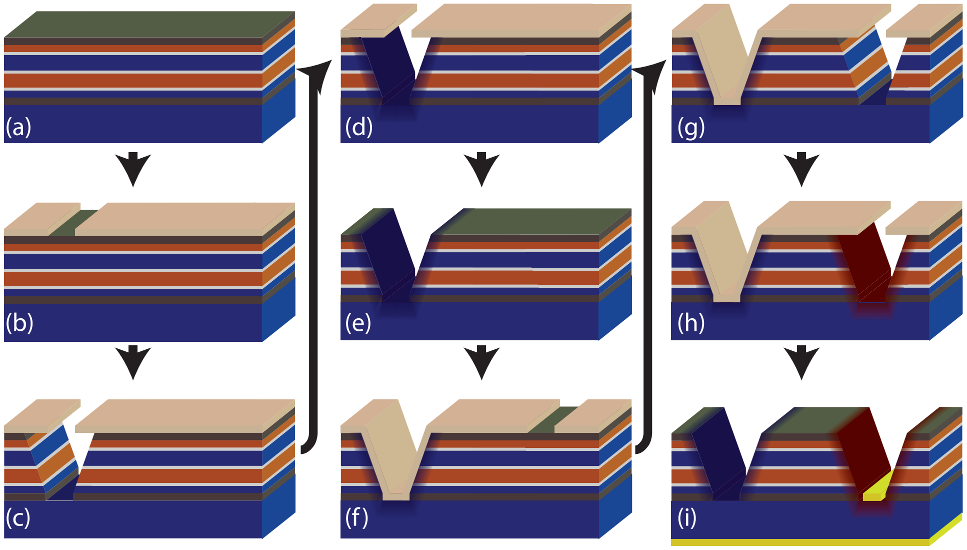

Figure 4.10: Depiction of process flow for the diffused junction *nipi* device. (a) shows the initial SL growth, (b) is following deposition of SiO_2 and lithographic patterning, (c) depicts the crystallographic etch in the *nipi* layers, (d) is following the diffusion process, (e,f,g, and h) are repeating the same steps for the second regrowth, and (i) shows the device after metalization.

the crystal structure at the surface if it is coated directly onto the semiconductor, so a 70 nm PECVD SiO_2 barrier is grown on the sample after the v-groove etch as recommended by the vendor. Additionally a 500 nm PECVD SiO_2 is deposited on the backside of the wafer to keep any SOG from contaminating the backside, and block the out diffusion of arsenic from the GaAs surface at the high anneal temperatures. The SOG is then drop cast onto the wafer through a 2 μm filter prior to a 500 RPM spin for 10 s to conformally coat the wafer, which is then ramped to 4000 RPM for 40 s to thin the film prior to the final spin step at 5000 RPM for 5 s which helps to improve thickness uniformity with an average thickness of 300 nm. Following spin coating the film is baked on a 100°C and 200°C hot plate for five minutes each to slowly drive off the solvents from the dopant source. This is followed by a 45 minute furnace bake at 450°C to evaporate any solvents that could remain. A 500 nm PECVD SiO_2 is then grown on top of the hardened dopant source which has been found to be helpful in allowing the oxide stack to be etched

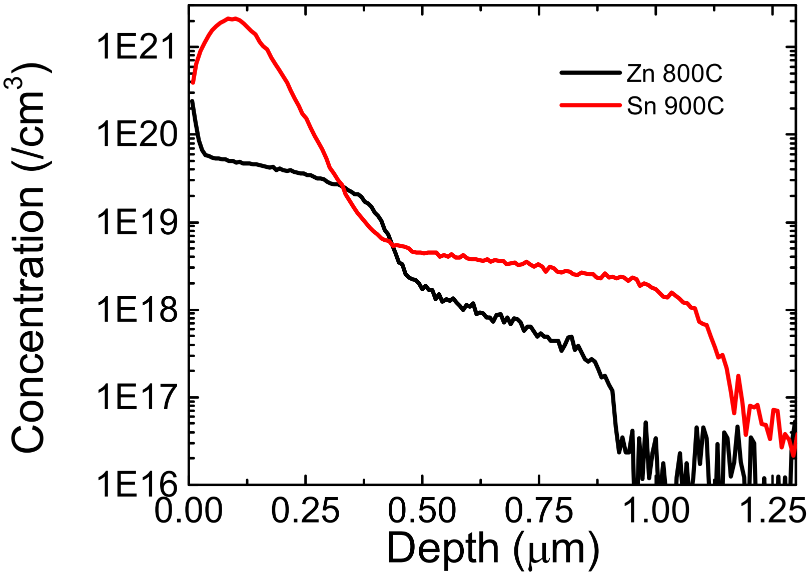

Figure 4.11: SIMS profile of both tin and zinc dopants following the high temperature anneal

following anneal. The wafer is then annealed at the desired temperature for the required time, and the oxide and dopant source is stripped in BOE. The metalization and mesa process are the same as what was described in Section 4.1, and no ARC was applied.

Test anneals have been completed over a temperature range of 700 to 900°C for a soak time of 45 minutes, and secondary ion mass spectrometry (SIMS) was done on a selection of the samples to evaluate the dopant concentration and junction depth. Intrinsically doped substrates were used to minimize any background doping in the SIMS results, with a (100) surface offcut 2° towards the (110) to match the device wafers. Anneals were completed in a 4" tube furnace which was ramped from 400°C to 700°C over 45 minutes, followed by a ramp to the final temperature at a rate of 3.3°C per minute. The profiles are shown for a tin diffusion completed at 900°C, and a zinc diffusion at 800°C for 45 minutes each. Although literature regarding tin diffused junctions provides the expectation that the peak concentration should be approximately 5x10^{18} /cm^3, the SIMS data shown in Figure 4.11 shows a maximum concentration that exceeds 10^{21} /cm^3. It is assumed that most of the dopant is inactive at such high concentrations, although this assumption has not been able to be tested since active dopant profiling

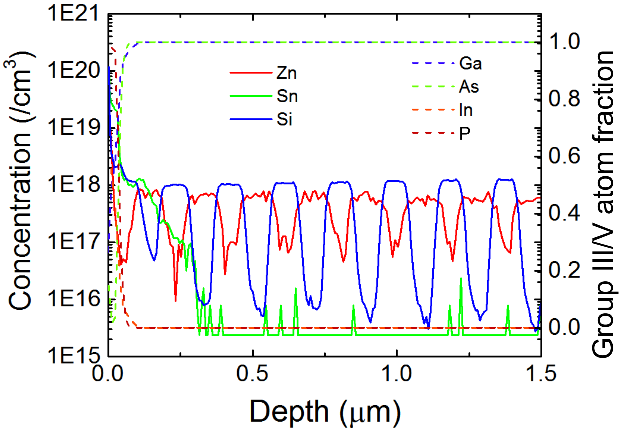

Figure 4.12: SIMS profile of both tin and zinc dopants following the high temperature anneal

techniques such as electrochemical capacitance-voltage measurements have difficulty measuring concentrations greater than 10^{19} /cm^3. The results from the zinc diffusions do closely match the expected dopant concentration and profile depth from literature [61, 63].

When a GaAs wafer is raised to a temperature in excess of 570°C the arsenic will out-diffuse from the surface of the wafer, leaving behind a gallium metal layer [64]. The surface Ga layer is metallic and will shunt the SL layers that are exposed in the v-groove. An oxide layer can act as a diffusion barrier, trapping the mobile arsenic within the semiconductor. As the temperature is decreased, the arsenic will move back into a lattice site maintaining the integrity of the crystalline structure. This was tested by coating a 500 nm thick SiO_2 layer on the front and back sides of a *p-type* doped substrate with dopant concentration of 1×10^{19} /cm^3 and annealing it at 900°C for 45 minutes in a tube furnace. After the anneal the oxide was stripped and it was seen that the surface maintained high reflectivity, which would not be the case if the arsenic had desorbed from the surface. Indium contacts were then applied to the surface of the wafer to perform Hall measurements. The dopant and mobility measurements of the annealed substrate matched the measurements of the substrate prior to anneal, ensuring that the oxide cap prevents the surface degradation expected in GaAs wafers at high temperatures.

A second concern is the mobility of zinc and silicon dopants making up the *nipi* SL. Since the 800°C zinc drive-in results in dopant concentrations greater than 1x10^{17} /cm^3 at a depth of 0.9 μm, the stability of the zinc in the *nipi* layers during high temperature diffusions is a concern. The diffusivity of silicon is significantly less than that of zinc, so it is not much of a concern that the silicon-doped layers would be diffusing [65]. To test this, an 200 nm SiO_2 layer was grown on a *nipi* SL with initial doping levels of 1x10^{18} and *n*, *i* & *p* layer thicknesses of 50 nm, and tin SOG was coated on top of the barrier. The sample was then annealed at 900°C for 45 minutes, and SIMS analysis was completed to detect zinc, tin, silicon and the matrix elements of the device. The data shown in Figure 4.12 shows that the peak concentration of zinc decreases to approximately 5x10^{17} /cm^3, and concentration in the mid 10^{16} /cm^3 are measured in the UID and *n-type* regions. Although this is not ideal, the modification to the dopant profile can be tolerated in a device since the *n-type* layers are not fully compensated. Simulations in *Sentaurus* were completed with the post diffusion dopant concentrations, and it was seen that J_{SC} and V_{OC} were not changed, while a 0.5% increase in FF resulted in a corresponding increase in efficiency. The FF likely increased because the resistance in the *p-type* layer was reduced by widening the quasi-neutral *p-type* region. A way to alleviate the concern with dopant mobility would be to switch from zinc to carbon as the *p-type* dopant source for the *nipi* layers, which has orders of magnitude lower mobility than zinc [66]. This study; however, was not completed due to time limitations but could be completed as a part of the future work.

4.3 CONCLUSIONS

In this chapter we evaluated the process required to fabricate the carrier selective contacts of a *nipi* solar cell. The possible methods for fabrication have been evaluated, including epitaxial regrowth, smart metalization, ion implantation, diffused junction, or MBE shadow masking. It is possible to fabricate all methods except for smart metalization by either two front-side or front and back-side contacting.

An evaluation of the specific steps required to fabricate the device was also completed. This included the crystallographic v-groove etch which exposes the Ga terminated (111)A plane on the sloped sidewall. The regrowth process was also characterized, evaluating GRE as a function of grid finger spacing and determining the proper selective dielectric mask to use for the regrowth.

Finally an analysis was completed on the different process steps required to complete a diffused junction fabrication process to achieve the carrier selective contacts. The diffusion process was characterized by SIMS to determine the dopant concentration and junction depth. Also simulations were completed to evaluate the mobility of the SL dopants when elevated to the temperatures required for driving in the dopant.

Chapter 5

An Evaluation of *nipi* Superlattice Solar Cell Device Results

Multiple device structures have been grown for this work. However, one design has been chosen as a baseline for comparison. The baseline design consists of 12 *nipi* repeats, with each repeat unit being 200 nm, consisting of equivalent doped and undoped layer thicknesses of 50 nm. The doping concentration for the *n*- and *p-type* layers is targeted to be 1x10^{18} cm $^{-3}$, and as discussed previously the unintentionally doped region has a *n-type* dopant concentration of approximately 1x10^{15} cm $^{-3}$. Regrown contact solar cells were fabricated according to the procedure described in Section 4.1, and diffused junction devices according to the procedure described in Section 4.2.

Current-voltage (I-V) measurements were taken both in the dark, and under one-sun AMO illumination on the devices under test. One-sun measurements were taken with a TS Space Systems dual zone solar simulator with a close match to the ASTM E-490 AM0 solar spectrum, while I-V measurements were taken with a Keithley 2400 SMU. The match between the spectrum generated with the mercury arc lamp and quartz-tungsten-halogen dual zone simulator and the ASTM AM0 and AM1.5G spectrums is

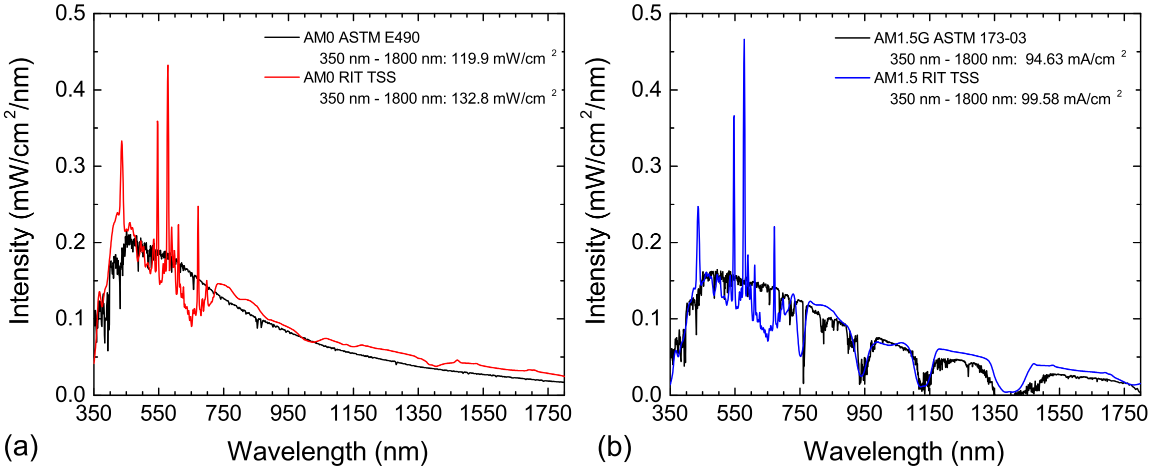

Figure 5.1: Graph of the ASTM standard compared to the spectrum measured from the RIT TS Space Systems dual zone solar simulator for both spectrums (a) AM0 and (b) AM1.5g.

shown in Figure 5.1. Dark I-V measurements were taken in a darkened enclosure with a Keithley 2400 SMU, which was also used to take J_{SC}/V_{OC} curves by gradually increasing the intensity of four tungsten halogen lightbulbs to up to 2.5 suns using a Sorenson DLM 80-7.5 power supply and measuring both J_{SC} and V_{OC} on the Keithley 2400 SMU. The structure was also simulated using the program *Sentaurus* by Synopsis, using the same technique described previously in Section 3.2.

5.1 EPITAXIALLY REGROWN DEVICE RESULTS

Multiple experiments have been completed with epitaxially regrown devices, each of which will be presented in their own section. The experiments detailed consist of an evaluation of the cell size and grid finger spacing of a solar cell contacted with the front contacting method. From this experiment it was determined that it was necessary to move to the back contact method to increase the shunt resistance. This is followed by the experiment where the regrowth processing steps for the back contact device was evaluated. Devices from that study were evaluated under elevated solar concentration levels to study the trap states at the regrowth interface. A final epitaxial regrowth experiment evaluated the use of InGaP and AlGaAs for higher bandgap regrown contact materials.

Table 5.1: Summary of dark and light current metrics for initial fabricated devices, compared to simulation results.

	Series Resistance (Ω)	Shunt Resistance (Ω)	n	J_o (A/cm^2)	J_{SC} (mA/cm^2)	V_{OC} (V)	Fill Factor (%)	Efficiency (%)
Experimental	0.46	11.1 k	2.70	1.1x10^{-6}	16.2	0.64	45	3.4
Simulation	0.1	10 G	1.55	1.97x10^{-13}	20.6	0.98	82	12.2

5.1.1 Characterization of Grid Finger Spacing and Cell Size in *nipi* Solar Cells

Solar cells were fabricated using the epitaxial regrowth process where there was a multiple day delay between the v-groove etch and the epitaxial regrowth process. The v-groove etch was completed at RIT and then taken to Cleveland, Ohio where the regrowth was done in the MOVPE at GRC. The regrowth was completed with a nominal zinc doping of 6x10^{18} /cm^3 and silicon doping of 2x10^{18} /cm^3 with a nominal thickness of 150 nm. The devices were fabricated according to the process described in Section 4.1.

Measured dark J-V curves for the best performing device with 100μm grid finger spacing and 1 cm^2 area are shown in Figure 5.2(a). Dark saturation currents, ideality factors, series and shunt resistances were extracted by fitting the *J-V* curves with the ideal diode equation by least squares regression [67]. Results from the fits are shown in Table 5.1, which show the dark saturation currents are significantly higher for the experimental results than what was expected from simulation. This increase is largely due to the two regrown junctions connected in series to the *nipi* layers. Trap states at the regrown junction interface form from growth defects and contamination of the surface following the v-groove etch, prior to regrowth [68]. It is believed that the trap states increase the carrier generation in the device, which increases the dark current and the experimental J_o values. Further increases in dark current come from the twenty-five parallel connected diodes in the doping SL, all of which contribute to dark current. This contributes to the increased dark current in the simulation from what would be expected for a conventional single junction diode.

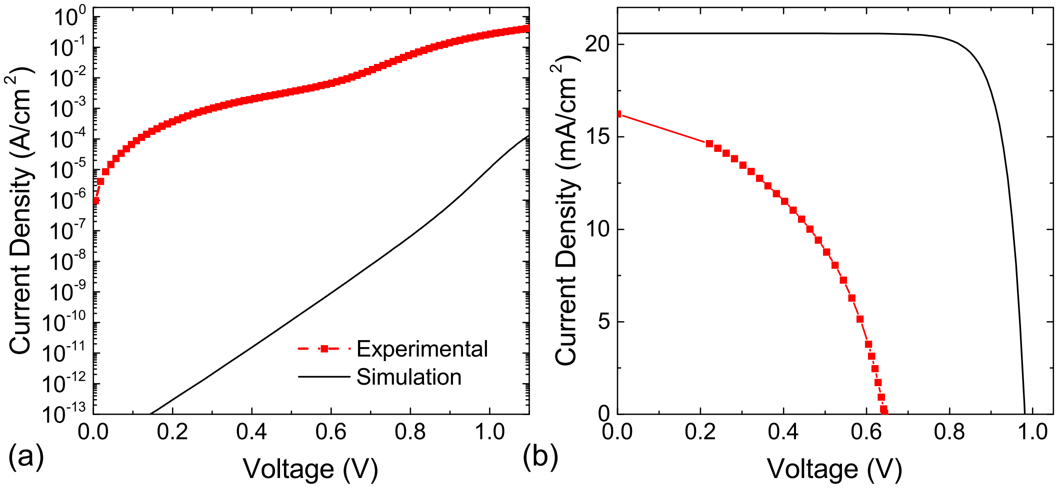

Figure 5.2: (a)Dark and (b) one sun *J*-*V* curves for both the fabricated device and simulation

Results from one-sun *J*-*V* curves are displayed in Figure 5.2(b), and compiled in Table 5.1. Measured J_{SC} is lower than the 24 mA/cm^2 that would be expected in a conventional GaAs cell without anti-reflective coating. The reduction in J_{SC} is due to grid finger shadowing, which was accounted for in the simulation. Figure 5.3 shows that gold covers less than half the grid finger area due to lithographic overlay limitations. In this device with grid finger spacing of 100 μm the shadowing fraction is 23%, which significantly reduces J_{SC}. Voltages are reduced from that of a typical GaAs single-junction V_{OC} of 1.05 V. This is explained primarily by the increased dark current. *J*-*V* curves show a much lower FF for the experimental case, which is due to the dual effect of increased series resistance and reduced shunt resistance, both of which will be addressed below. All of these effects lead to the relatively low efficiency of 3.42%; however, a reasonable initial attempt at a difficult fabrication process.

Additional information was gained about the series and shunt resistances of the device structure by evaluating them with respect to grid finger length and cell area, as shown in Figure 5.4 (a) & (b). The top plot showing series resistance demonstrates that the predominant factor determining series resistance is the grid finger spacing. The limiting resistance in the *nipi* design is the thin doped layers through which current must travel to reach the metal grid fingers. The series resistance is reduced as the grid finger

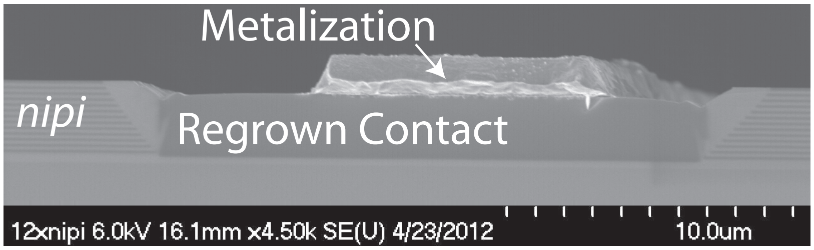

Figure 5.3: SEM micrograph showing the cross section of a *nipi* device, with the *nipi* layers on the left and right, and the regrown contact in the center with the gold metal stack above it

spacing is reduced because this shortens the resistive path that current must travel through the *nipi* layers. As the cell area increases the length of the grid finger also increases, which results in higher series resistance due to current crowding in the undersized grid finger.

The area-specific shunt resistance shown in Figure 5.4 (b) shows the two effects of decreasing shunt resistance with decreasing grid finger spacing, and cell area. As the grid finger spacing decreases the total number of regrown contacts increases which increases the total regrown interface area. This brings about a reduction in the shunt resistance because the total volume of interface traps is increased. This result continues to demonstrate the need to improve the interface quality of the regrown material. If high shunt resistance can be achieved with smaller grid finger spacing, a device can be made to minimize the effects of both series and shunt resistances. The decrease in shunt resistance with cell area can be explained by a shunt that occurs between the *n-* and *p-type* probe pads that are both on the InGaP window as shown in Figure 4.6. As the cell area is decreased, the distance between the bus bars is correspondingly decreased resulting in a lower shunt resistance. This effect can be eliminated by depositing an insulator layer beneath the probe pads, or by using a back side contacting scheme.

5.1.2 Evaluation of Front and Backside Contacting Methods

Devices were fabricated with the metal contacts placed on the front and opposing sides of the device. An image of the fabricated solar cells for both front and back-side contacting methods is shown in

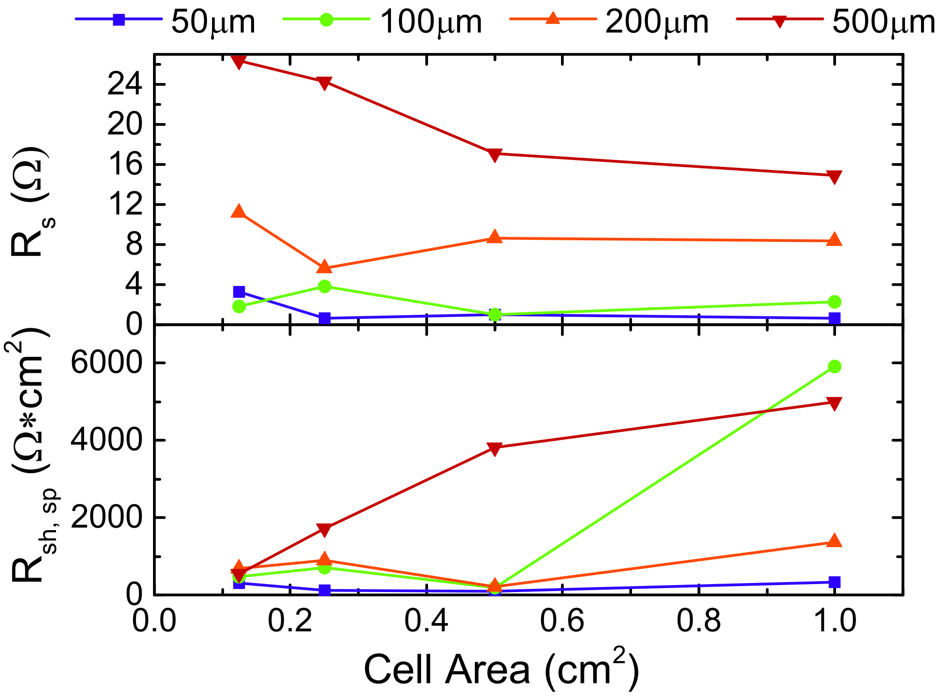

Figure 5.4: (a) Series and (b) area specific shunt resistances plotted verses cell area as a function of the grid finger spacing. The legend indicates the different grid finger spacings for each device.

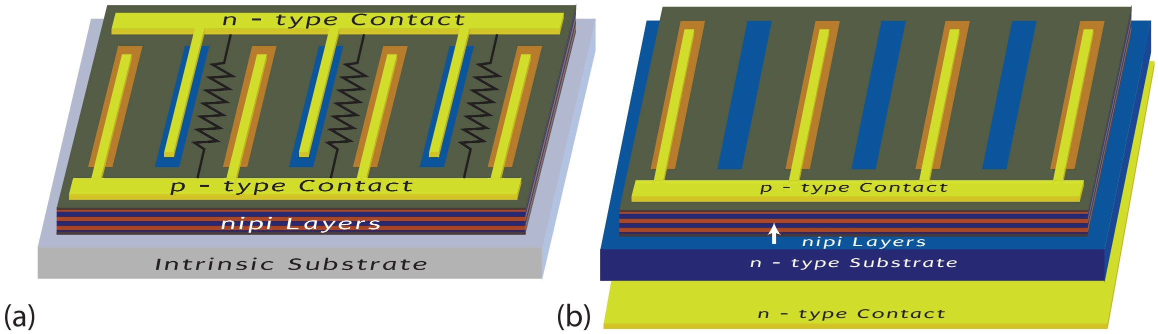

Figure 5.5: Depiction of a *nipi* device fabricated with (a) double front-side contacts and (b) front and back-side contacts.

Figure 5.5. Forming contacts on opposing sides was expected to eliminate the shunt path through the top InGaP window, where the shunt path is depicted in Figure 5.5(a). To minimize the potential of spiking the regrown junction with the highly mobile Au/Ge n-type contact it was made on the backside of the solar cell while the p-type contact was made on the front side. For these solar cells the v-groove etch and epitaxial regrowth were both completed at the NASA GRC with less than ten minutes between the etch and loading the wafer into the reactor. The nominal zinc and silicon dopings were kept the same as described in the previous experiment, while the nominal growth thickness was reduced to 100 nm. The devices were fabricated according to the process described in Section 4.1, with one device contacted by the front contacting method and the other contacted by the back contacting method. A new mask design was used for the back contacting method that reduced shadowing to 17% for the 100 μm grid finger spacing as opposed to 23% for the front contact solar cell.

By reducing the time between the v-groove etch and epitaxial regrowth as much as possible the environmental contamination at the interface is reduced, thus improving the interface. Additionally the reduction in nominal thickness from 150 nm to 100 nm is a reduction of growth in the v-groove of up to 0.5 μm given the highest GRE of 10 discussed in Section 4.1. As the growth in the v-groove approaches and exceeds the depth of the trench the selectivity of the growth reduces, resulting in more growth on the oxide above the active region.

When anode and cathode are formed on the same side of the device, a shunt path is formed through the InGaP window, seen largely in a reduction in FF as shown in Figure 5.6 (a). Both epitaxial regrowth devices compared here were regrown at the same time, so it is assumed that the regrown interface is identical. The only difference is in the use of a doped wafer through which the backside contact is formed. The separation of contacts results in over an order of magnitude increase in shunt resistance, and nearly three orders of magnitude decrease in dark saturation current as shown in Table 5.2. Corresponding to the improvement in shunt resistance and dark saturation current is also an increase in V_{OC}

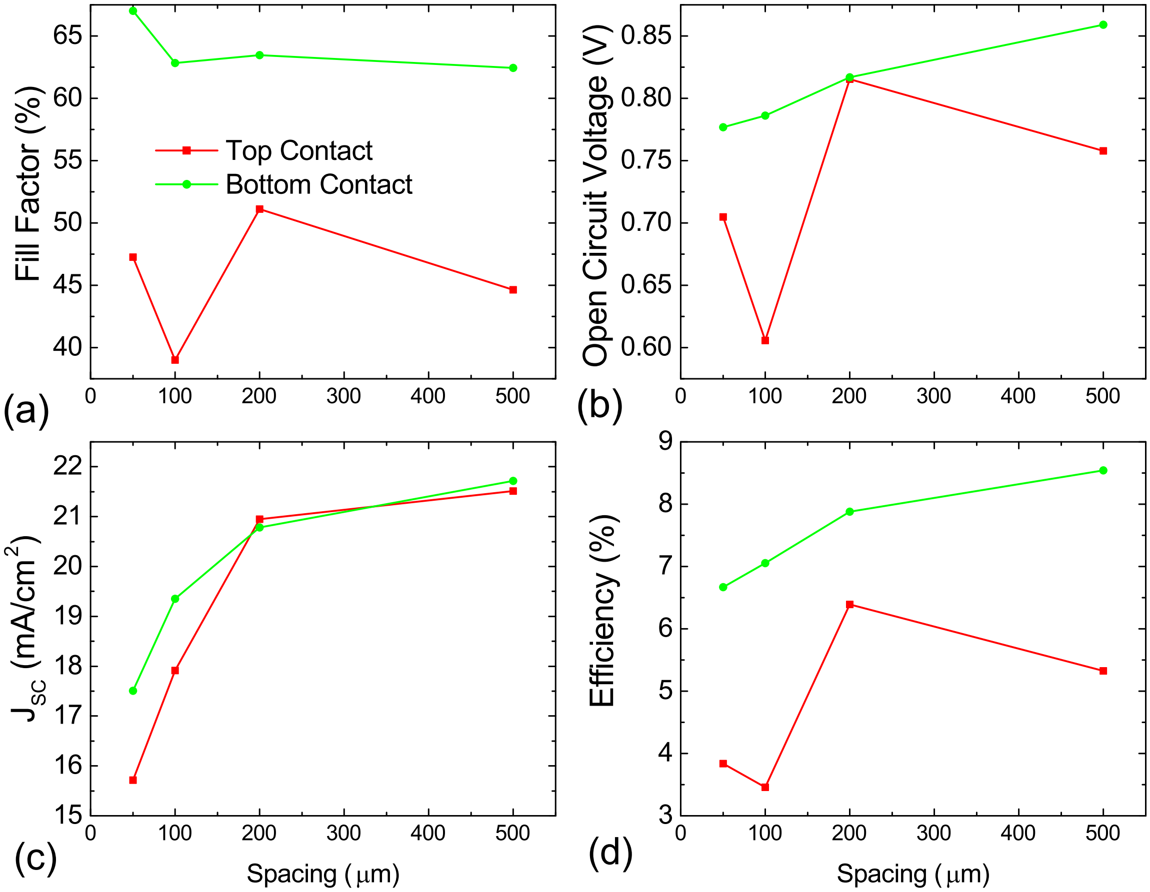

Figure 5.6: Averages of multiple devices contacted by the double top side contact and the back side contact, showing (a) J_{SC}, (b) V_{OC}, (c) FF, and (d) efficiency

Table 5.2: Summary of one sun and dark I-V metrics for devices contacted by front and back-side epitaxial regrowth.

Contact Method	J_{SC} (mA/cm^2)	V_{OC} (V)	FF (%)	η (%)	R_s (Ω)	R_{sh} (Ω)	n	J_o (A/cm^2)
Regrow - Back Contact	22.6	0.86	63	9.0	3.81	32.8 k	2.43	$5.0\text{x}10^{-8}$
Regrow - Front Contact	20.6	0.80	51	6.1	1.38	2.01 k	4.33	$1.35\text{x}10^{-5}$
Back Contact Simulation	22.21	0.9427	80	12.31	1.08	605 M	1.712	$1.68\text{x}10^{-11}$

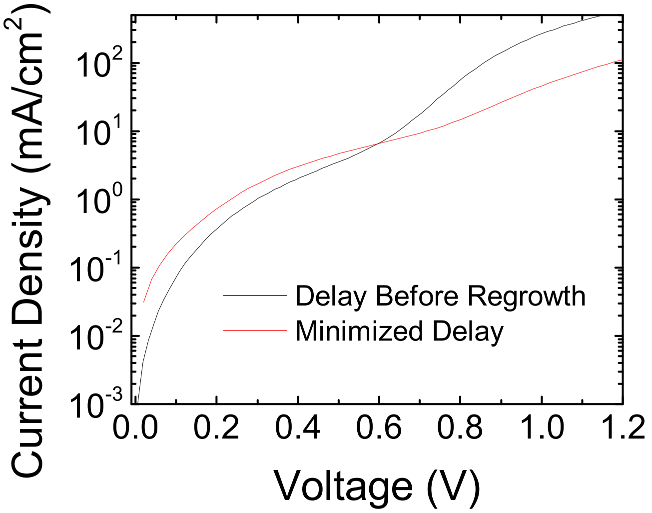

Figure 5.7: Dark IV measurements of devices contacted by the front contact method with an extended and minimized time span between the v-groove etch and epitaxial regrowth.

as shown in Figure 5.6 (b). Each of these improved metrics can be attributed to the elimination of a resistive path through the InGaP window which in effect added a resistor in parallel to the solar cell for the front contact device. Moving from front contacts to back contacts also resulted in an increase in current due to the elimination of a second bus bar, this decreased shadowing losses in the back contact device. This is seen most clearly J_{SC} plotted in Figure 5.6 (c) for the smaller grid finger spacing, where the total shadowing is increased. The result is an improved efficiency of 9.0% which is much closer to the efficiency found via simulation.

The improvement gained by reducing the time between the v-groove etch and the epitaxial regrowth can be seen by comparing the front contact device in this experiment to the best device from the previous experiment. The metrics are shown in Tables 5.1 and 5.2. However, the dark current can be compared more directly in Figure 5.7. The device with minimized delay has a lower shunt resistance resulting in higher low voltage currents; however, the higher ideality factor of 4.33 results in lower dark current at higher voltages and a lower V_{OC}. Simulated dark I-V curves give an ideality factor of 1.84, which is in line with the depletion-region-dominated generation. However, it is unclear why the ideality factor was increased by over a factor of two. The ideality of 2.43 for the back contact device was closer to simulated value, and other solar cells on the same wafer as the device presented here had lower ideality factors as well. Variability did exist in the process and across wafers for these experiments. This variability has been reduced in later results, which are discussed in Section 5.1.3.

Devices fabricated with a minimal time between etch and regrowth also showed a increased J_{SC} of 20.6 mA/cm^2 as opposed to 16.24 mA/cm^2 for the previous result. Part of the improvement came from a changed mask design which reduced shadowing by about 1%. The reduction in the nominal regrowth thickness from 150 to 100 nm accounts for some of the improvement as well. As the thickness in the trenches reaches the surface of the selective mask the growth selectivity decreases. The result is more growth on the active region of the solar cell which absorbs light that is not collected as current.

5.1.3 Detailed Study of Regrowth Processing Conditions

A more detailed analysis of the fabrication process prior to regrowth was completed in two parts. Initially test structures were made to evaluate the regrowth interface where a single *p-n* junction is formed during the regrowth depicted in Figure 5.8. This is followed by the fabrication of a solar cell with the best regrowth conditions determined from the test structures.

Since the epitaxial regrowth contact formation entails multiple photolithography and etch steps prior to placing the wafer back into the MOCVD reactor for regrowth. Each of these processes presents the opportunity for contamination at the interface, requiring additional cleaning steps prior to regrowth.

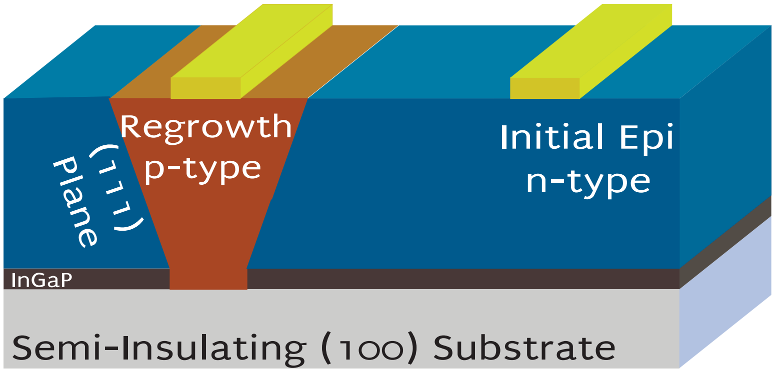

Figure 5.8: Depiction of lateral diode formed for the regrowth test structure used to characterize the regrowth prep and growth.

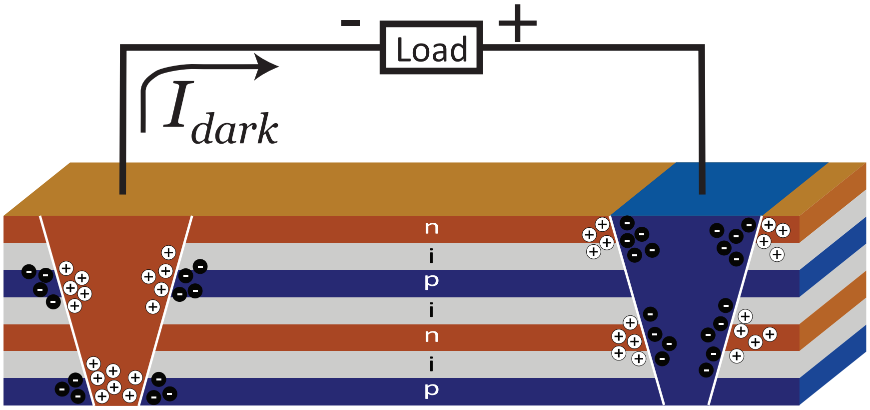

Figure 5.9: A cross-section of a *nipi* solar cell with the generated carriers from trap states depicted as contributing to dark current.

Multiple studies have evaluated the effect of using a sulfur based solution of NH_4S_x or H_2SO_4 to passivate the surface states prior to regrowth with demonstrated success [69, 70]. Further cleaning steps such as heated acetone and isopropyl can be used to decontaminate the surface from any organic residue, which have also demonstrated improvements in other work [71].

Additional modifications to the process can be evaluated during epitaxial regrowth. A reduction in growth rate has been shown to reduce the interface trap density [72]. The process of record utilized a crystallographic v-groove which exposes the (111)A plane of the *nipi* layers upon which the regrowth occurs as shown in figure 5.9. The process window for 2D layer by layer growth on (111)A GaAs surfaces is smaller than on either (100) or (111)B surfaces [73], and it could be advantageous to depart from the (111)A surface. This is possible by utilizing an isotropic etch that would not expose any particular crystal plane. Additionally the sensitivity of the regrown interface can be evaluated by rotating the mask pattern 90° for the etch. This results in a dovetail etch with the H_2SO_4:H_2O_2 etchant, also exposing the (111)A plane. Such modifications allow further characterization of processing on the regrown interface quality. Changing the exposed growth plane can change the formation of facets, or intersections of growth planes during the growth process. Increasing the number of growth facets increase the likelihood of dislocations and various other growth defects as the facets collide and during growth, this could be minimized by changing the initial orientation.

Test structures were grown to evaluate the epitaxial regrowth interface by MOVPE. An initial 2×10^{17} cm^{-3} doped *n-type* layer was grown above a lattice matched $InGaP_2$ layer that acts as an etch stop for GaAs. Growth was completed on 2 inch (100) UID GaAs wafers offcut 2° towards <110> direction. To form a single diode a selective regrowth process was used to regrow a *p-type* region to contact the sidewall of an etch in the initial *n-type* layer using a similar process to that described in Section 4.1. Both *n-* and *p-type* metal contacts are made to the top of the test structure, where the *n-type* contact is made initial growth, and the *p-type* metalization contacts the *p-type* regrown regions.

The effect of regrowth preparation on the interface was studied by varying three factors: sulfur passivation, solvent cleaning, and etch conditions. Three etch levels were evaluated: H_2SO_4:H_2O_2:H_2O (4:1:5) perpendicular to the $(01\bar{1})$ cleave plane to form a v-groove etch, H_2SO_4:H_2O_2:H_2O (4:1:5) perpendicular to the (011) cleave plane to form a dovetail etch, and a proprietary H_2SO_4:H_2O_2:H_2O by Transene, GA Etch-100 to etch an isotropic profile. Each etch profile is shown in Figure 5.10 with a SEM micrograph of the cross section after both etch and regrowth. Four levels were used to evaluate sulfur passivation which include: no sulfur treatment, thirty minutes in room temperature $(NH_4)_2S$, thirty minutes in $(NH_4)_2S$ heated to 60°C, and five minutes in H_2SO_4:H_2O (1:80). Solvent cleaning

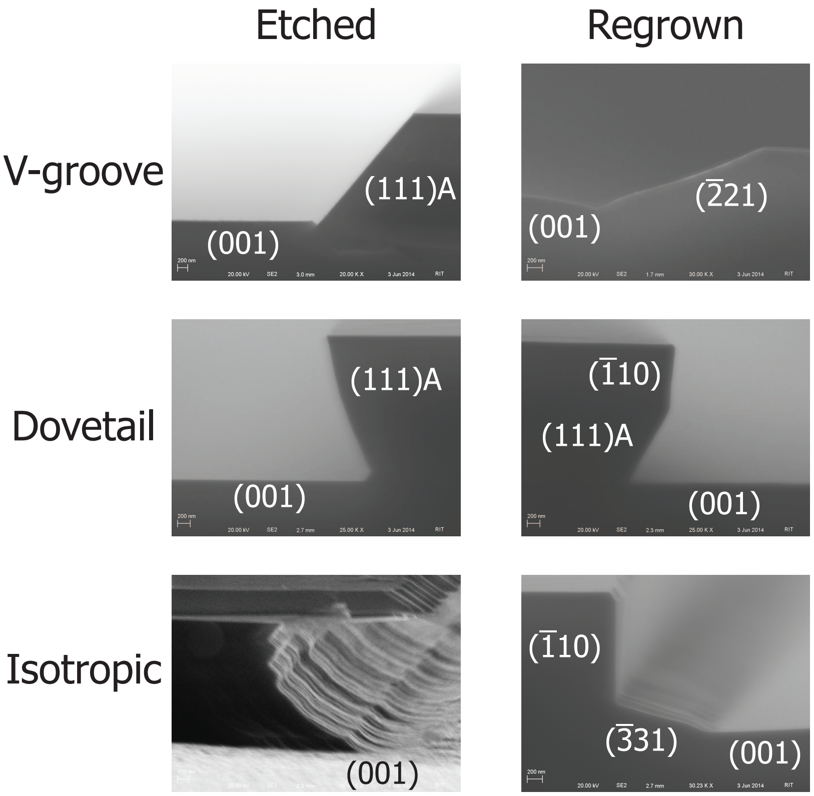

Figure 5.10: SEM micrograph of the v-groove, dovetail and isotropic etches following etch and after regrowth.

was evaluated with two levels, no solvent clean and five minutes in acetone followed with five minutes in isopropyl alcohol both heated to 50°C.

In addition to the etch and sample cleaning study a smaller experiment was conducted to evaluate regrowth conditions. The preparation conditions of room temperature $(NH_4)_2S$, no solvent clean, and v-groove etch were chosen while interactions between preparation and regrowth conditions were not evaluated. Two conditions were used for the GaAs regrowth, one with a 2μm/hour nominal growth rate, 620°C growth temperature, and a V/III of 35.4, and another with growth rate of 0.2μm/hour and V/III to 354. Two pre-growth in-situ processes were also evaluated. The first pre-growth process was a 20 second CCl_4 step at 550°C to etch approximately 2nm of GaAs prior to growth with 0.2μm/hour growth rate and V/III of 354. The second pre-growth process was a 700°C five minute anneal prior to growth with the 2μm/hour growth rate and V/III of 35.4.

Dark current measurements were taken on each test structure fabricated with the conditions described. Each I-V measurement was fit with a single diode model including shunt and series resistance to extract dark saturation current, ideality, shunt and series resistance.

Following characterization of the etch, cleaning and growth conditions the best treatment conditions were used to fabricate *nipi* solar cells. The baseline *nipi* solar cell design was used and fabricated according to the process described in Section 4.1. One-sun AM0 I-V testing was completed, and dark I-V and J_{SC}/V_{OC} measurements were taken. Dark I-V and J_{SC}/V_{OC} were fitted to extract dark current parameters with a single diode model because a two diode model was not appropriate.

A statistical analysis of the regrowth test structures was completed to determine the effect of each process condition on the dark diode measurements. For analysis the shunt resistance has been evaluated because the fitting error was lower than for dark saturation current, making it a more reliable indicator of diode quality. Similar trends were also seen in the dark saturation current.

The most significant effect was seen from changing the sulfur passivation process as is shown in Figure 5.11 (a). When averaging each of the sulfur passivation conditions the no-sulfur passivation had a shunt resistance of 2.0 MΩ, which reduced to 1.2 MΩ for the H_2SO_4:H_2O process, dropping further to 550 kΩ and 290 kΩ for the room temperature and 60C $(NH_4)_2S$ processes, respectively. The variance in the average does indicate that the H_2SO_4:H_2O process is statistically the same as the no-sulfur process; however, the averages are taken across all the other process conditions which increases the variance.

Since the experimental $(NH_4)_2S$ treatment samples contradicted other published work by degrading with the $(NH_4)_2S$ treatment [69, 70] an explanation is required. For this experiment the etch and clean processes were completed in as short a time as possible prior to placing the sample inside the MOVPE reactor for regrowth. The reduced time limits the growth of a native oxide that would contaminate the regrowth interface. If a negligible native oxide is formed in the no-sulfur treatment case, any additional

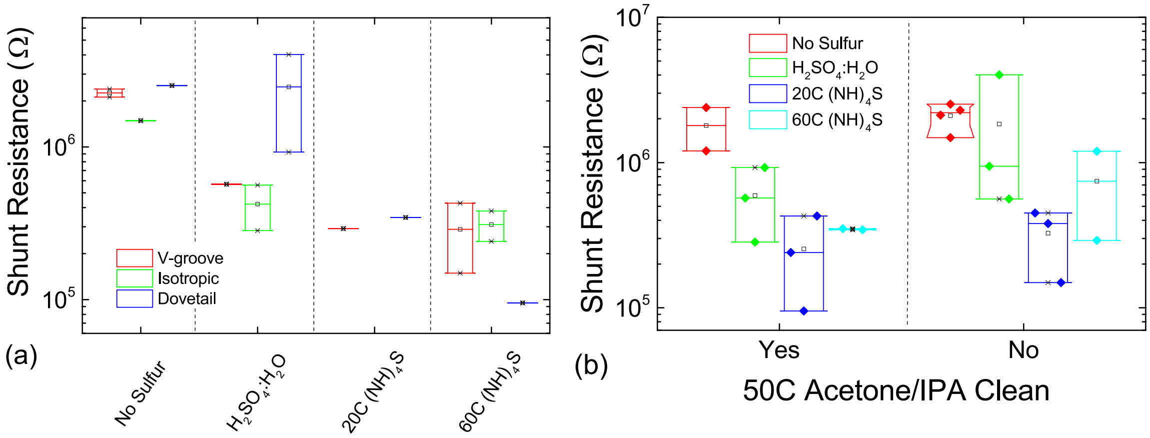

Figure 5.11: Fitted shunt resistance plotted versus (a) the four sulfur passivation conditions and the four etch levels, as well as (b) solvent cleaning and the four sulfur passivation levels.

processing of the sample can lead to contamination of the surface and a degradation of the interface. Additionally it had been noted that $(NH_4)_2S$ surface treatment can roughen the surface, which could lead to a degraded regrowth interface [74].

An evaluation of etch chemistries is seen in Figure 5.11 (a), where it can be seen that the effect of etch process is not as significant as the sulfur treatment. An analysis of the etch conditions shows there is no statistical difference between any of the processes. On average the dovetail etch has the highest shunt resistance of 1.58 MΩ, dropping to 992 kΩ for the v-groove etch, followed lastly by the isotropic etch with an average shunt resistance of 590 kΩ.

The SEM images in Figure 5.10 show the crystal planes that are formed after regrowth. Each etch profile provides different surfaces that terminate into growth facets that differ from the initial planes exposed in the etch. The (111)A plane leaves Ga on the surface and is known to be a slow growth plane, which allows numerous facets growing from the (011), (001) and other faster growing planes to propagate the growth for both the v-groove and dovetail etches [75]. The result is a departure from a 2D step-wise growth with numerous faceted interfaces that can result in growth defects and traps. It was hoped that an isotropic etch would reduce the number of growth facets by moving away from the

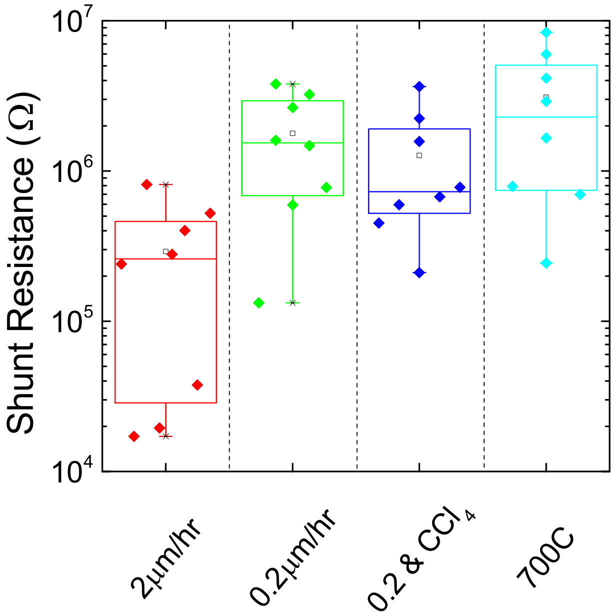

Figure 5.12: Shunt resistance plotted for both the v-groove and dovetail etches for each of the regrowth conditions.

(111)A slow growth plane; however, it is apparent that multiple growth facets are formed to terminate the growth in the $(\bar{1}10)$ and $(\bar{3}31)$ planes.

No improvement was seen by adding a heated 50°C acetone/IPA solvent clean prior to growth as shown in Figure 5.11 (b). Adding the clean resulted in an average shunt resistance of 683 kΩ, as compared to 1.37 MΩ without the clean. The rationale for this decrease in shunt resistance follows from the degradation seen from sulfur processing. Any additional processing after etch degrades the quality of the interface as long as the time between etch and regrowth is minimized.

Evaluation of growth conditions demonstrated that for the v-groove etch an improvement in diode characteristics was achieved by modifying the regrowth conditions as shown in Figure 5.12. Average shunt resistance increased from 281 kΩ with the 2μm/hour conditions to 1.78 MΩ with the reduced growth rate, 1.27 MΩ when the CCl_4 etch was included and finally 3.10 MΩ following the 700°C anneal step. The 2 μm/hour growth rate results in an actual growth rate between 8 and 20 μm/hour in the etched trench due to growth rate enhancement depending upon the spacing between etched grooves.

An increased growth rate can increase zinc incorporation [76], resulting in a lower percentage of active dopants, lower mobility and increased trapped charges. Adding a CCl_4 etch prior to regrowth etches the exposed GaAs with chlorine by forming $GaCl_3$ at elevated temperatures which cleans the surface of contaminants [77] while removing approximately 2 nm of GaAs. This reduces any environmental contaminants from the interface providing a clean GaAs upon which to grow. Finally the five minute 700°C anneal desorbs native GaO_x from the v-groove surface which would otherwise provide an amorphous surface upon which to grow thus reducing the crystalline quality.

Solar cells were fabricated with both the dovetail and v-groove etch, no sulfur passivation and no acetone & IPA clean following etch. Three growth conditions were used: 2 μm/hour growth rate with a V/III ratio of 35.4, a reduction in growth rate to 0.2 μm/hour and increase of V/III to 354, and the reduced growth rate in conjunction with the CCl_4 etch prior to the *p-type* regrowth. The CCl_4 etch was only used for the *p-type* regrowth to avoid carbon doping the interface of the *n-n* ohmic contact in the *n-type* regrowth.

Efficiency is plotted for each of the process conditions in Figure 5.13 where the different colors indicate different grid finger spacing. Both J_{SC} and V_{OC} improve as the grid finger spacing is increased, J_{SC} due to a reduction in shadowing and V_{OC} because of a reduction in the regrowth interface area. For each of the process conditions the dark current from the regrown interface was higher than the dark current from the *nipi* SL, so a reduction in regrown contact area improves V_{OC}.

The highest efficiency of 9.14% was measured on the device with dovetail etch and the faster growth rate. For both the v-groove and dovetail etch conditions the faster growth rate conditions demonstrated an average improvement in efficiency. A relative improvement of 2.16% was seen for the dovetail etch, and 1.17% for the v-groove etch for the 2 μm/hour growth rate over the reduced rate when outliers were not considered. This is contradictory to the test structure results; however, the test structures were processed with the room temperature $(NH_4)_2S$ passivation step that degraded the interface. It is possible

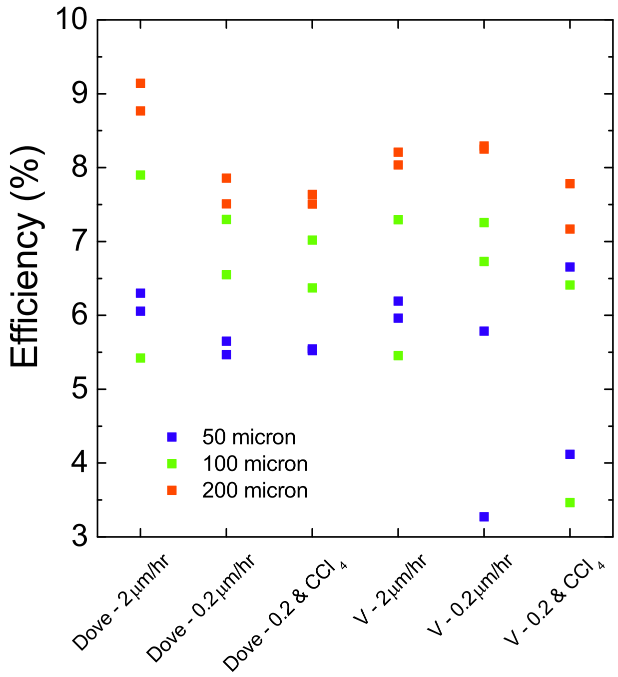

Figure 5.13: Efficiency for each of the etch and regrowth conditions plotted as a function of grid finger spacing.

that an interaction between the regrowth conditions and the sulfur passivation resulted in the apparent contradiction in results; however, this was not tested in the test structures.

Comparing the reduced growth rate solar cells with and without CCl_4 a small loss in efficiency of 0.5% was seen when the CCl_4 etch was included. The etch likely roughens the GaAs surface slightly which would degrade the solar cell if the interface has minimal environmental contamination due to the short time between etch and regrowth. This is contradictory to the test structure; however, this could also be related to an interaction between growth and processing conditions.

A nominal improvement of 0.65% was seen for the v-groove etch over the dovetail etch on average, and shows no statistical difference. The difference resultant from the change in exposed crystal face does not seem to be a significant factor affecting the regrowth interface. This is a surprising result, especially given the initial assumption that the dovetail etch would result in degraded results since the face of the side-wall is directed away from the flow of source material.

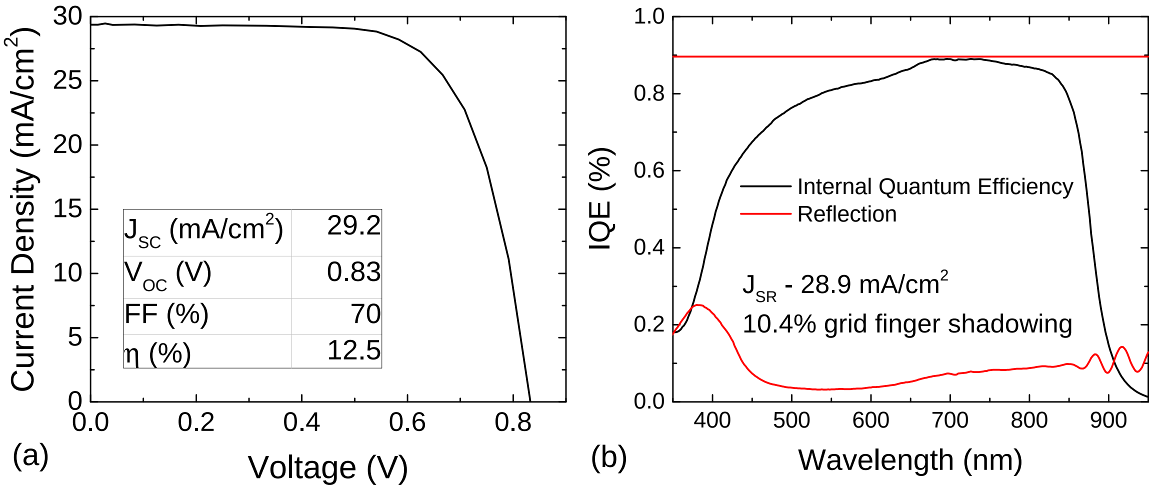

Figure 5.14: Plot of (a) one-sun AM0 J-V, (b) internal quantum efficiency and reflectivity of the highest efficiency *nipi* solar cell with dovetail etch, no additional chemical processing and 2 μm/hour growth rate with a dual layer AR coating.

Following analysis a dual layer ARC was deposited with zinc-sulfide (ZnS) magnesium fluoride (MgF) onto the solar cell by thermal evaporation to minimize reflection. One-sun AM0 and internal quantum efficiency measurements were taken of the highest efficiency solar cell with dovetail etch, no additional chemical processing and 2 μm/hour growth rate. The results are plotted in Figure 5.14. This result demonstrates the highest efficiency measured for a *nipi* solar cell to date of 12.5%, and a J_{SC} of 29.2 mA/cm^2. The majority of the loss in current is due to the grid design which resulted in 10.4% shadowing, with the non-shadowed collected at nearly 100% quantum efficiency. Some additional loss in current was due to the anti-reflection coating being slightly off resulting in 5-10% reflection. Additional characterization was completed on this solar cell prior to ARC and is presented in the following Section 5.1.4, followed by analysis of the regrowth interface by transmission electron microscope (TEM) in Section 5.1.5.

The V_{OC} measurement after depositing ARC increased to 0.83 V from 0.78 V before ARC. There are two possible causes for the increased V_{OC}. The first cause is that the increased light coupled into the cell increased V_{OC} according to the logarithmic trend predicted by the ideal diode equation, however

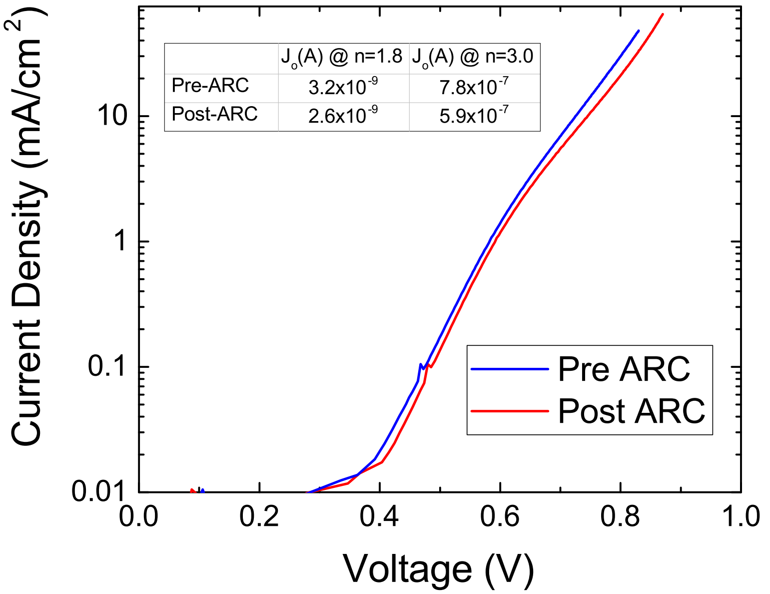

Figure 5.15: J_{SC}/V_{OC} measured both before and after ARC, showing a slight improvement in dark current reflected in the extracted dark saturation current.

the increase for these devices is greater than would be expected. The increase in light also increases the photo generated carrier density which can fill trap, which was discussed in Section 3.3, and will be discussed further in the following Section 5.1.4. The second cause of an increase in V_{OC} would be from the passivation of surface states on the side-wall of the *nipi* SL. As was mentioned in Section 3.2.1 unpassivated bonds on the side-wall can result in a decrease in V_{OC} that is greater in a *nipi* device than in a conventional solar cell due to the 25 junctions that exist in the device under test. Prior to the deposition of ARC the device was etched in a dilute HCl:H_2O (1:10) mixture to remove any surface oxide, the ARC can then form bonds with the dangling bonds on the side-wall.

To isolate the two effects discussed J_{SC}/V_{OC} measurements were taken. The J_{SC}/V_{OC} measurement is irrelevant to the intensity of the light shining on the device, it is an relationship between the light coupled into the cell with the internal voltage induced, so any decrease in J_{SC}/V_{OC} would only be caused by a passivation of surface states. The measurement is shown in Figure 5.15, where a decrease in dark current is seen after ARC. Dark saturation current was extracted and a reduction from 3.2x10^{-9} A to

Table 5.3: Measured light I-V metrics of the highest efficiency *nipi* solar cell measured as a function of solar concentration.

Concentration	J_{SC} (mA/cm^2)	V_{OC} (V)	FF (%)	η (%)
1.0	8.7	0.77	71	9.45
3.8	33.2	0.78	70	9.47
7.4	64.2	0.89	64	9.93
11.8	103	0.95	58	9.53
19.4	169	0.97	51	8.64
27.6	240	0.98	45	7.74

2.6x10^{-9} A in the n=1.8 region and from 7.8x10^{-7} A to 5.9x10^{-7} A in the n=3.0 region. This indicates that passivation of side-wall surface states is occurring and at least partially contributing to the increase in V_{OC}. It is possible that depositing the ARC by a chemical means like plasma enhanced chemical vapor deposition (PECVD) instead of the more physical deposition of thermal evaporation a more complete passivation could occur, further improving V_{OC}.

5.1.4 Characterization of *nipi* Solar Cells Under Concentration

The highest efficiency *nipi* solar cells fabricated in the previous study were measured under solar concentration from 1x10^{-4} to 27 suns. A plot of the J-V curve for different concentration levels is shown in Figure 5.16, with the extracted data shown in Table 5.3. As the concentration is increased the current scales linearly with concentration, and the voltage increases; however, a significant reduction in FF is seen. The cause of the reduction is due the baseline design with 1x10^{18} /cm^3 doped layers that are 50 nm thick. This is sufficient for the *n-type* layer; however, the *p-type* layer has an order of magnitude lower resistivity which can result in I^2R losses at higher currents. The current baseline structure was not designed for measurement under concentration, and changes to the design would allow increased concentration without losses in FF.

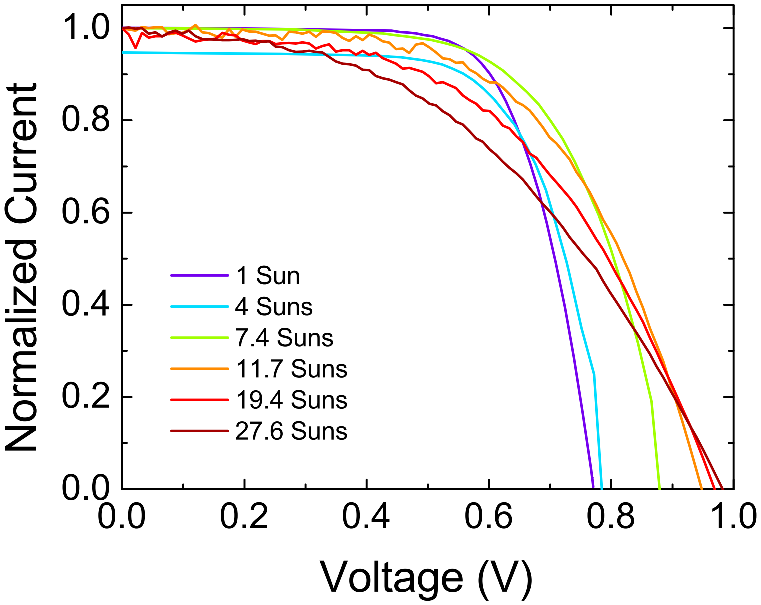

Figure 5.16: Current-voltage plot of the *nipi* solar cell measured at concentration from 1 to 27.6 suns. Current is normalized to one sun J_{SC}.

Further analysis of V_{OC} with respect to concentration showed an improvement that exceeded the expected $\frac{kT}{q} ln(X)$ trend when X is concentration factor. This formula is an adaptation of the ideal diode equation [49], which determines the change in V_{OC} with a relative change in J_{SC}. It is expected that V_{OC} would logarithmically increase with respect to concentration; however, for the *nipi* device the rate of increase in V_{OC} exceeds the logarithmic trend. The data is plotted as bandgap-V_{OC} offset (W_{OC}) which is E_g minus V_{OC} in Figure 5.17 (a). W_{OC} is a figure of merit that is expected to be approximately 0.4 V for a high quality solar cell operating at one sun. The loses that result a 0.4 V W_{OC} are largely driven by radiative recombination that escapes the device, and any additional loss in excess of 0.4 V can be generalized to be related to non-radiative recombination [78]. In the figure the experimental data is shown in red with the extrapolated logarithmic trend shown in the green dotted line, which diverges from the experimental at close to one sun.

To understand the divergence the model developed in Section 3.3 was used to fit the experimental results. In order to calculate the I-V curve the fitting terms for series and shunt resistance R_s and R_{sh}

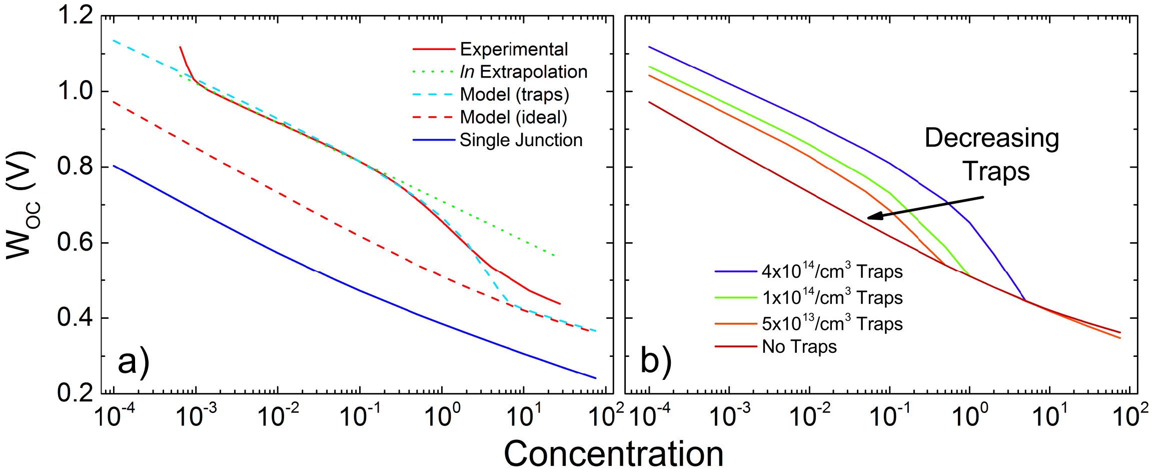

Figure 5.17: Plot of W_{OC} versus concentration for (a) the experimental measurement, extrapolation of the expected logarithmic decay, modelled results with traps to fit the experimental, ideal modelled results and a comparison to a single junction device and (b) a comparison of modelled results with four trap densities.

were found to be 0.2 Ω and 1x10^8 Ω, respectively. The fitting parameters for the lifetime and dark saturation current calculations are identical to those described in Section 3.3. Current-Voltage curves were calculated as a function of concentration from 1x10^{-4} to 100 suns and compared to solar cell measurements under similar concentrations. The fitted results are shown in the blue dashed line which has a greater than expected improvement in W_{OC} between zero and 7 suns. For comparison additional curves were calculated, where the red dashed line is an ideal *nipi* calculation that assumes no trap states, and the blue solid curve is a calculation for a single junction solar cell that follows the two diode model with the contact term neglected.

The modeled results follow the trends seen in experimental data very well up through the improvement in W_{OC}, which is a good indication that the improvement is in fact due to state filling of traps. The model shows that after a solar concentration of 6x it is expected that all the trap states will be filled and the traps will no longer degrade the I-V results. The experimental results don't line up perfectly with the modeled improvement that matches the ideal case past 7 suns. An explanation would be that the model assumed a single trap energy E_t; however, in reality multiple energies or a dispersion of energies would vary the concentration needed to fill the states.

Additionally, modeling was completed varying the interface trap density from 4x10^{14} /cm^3 which matched the experimental results to no interface traps and is plotted in Figure 5.17 (b). As the trap density is reduced the concentration at which the model matches the ideal case is reduced to lower and lower levels. This provides an achievable target for trap densities, which are required to be below a level at which the W_{OC} improves to ideal values at a concentration below one sun. That point for these conditions would be a density of 5x10^{13} /cm^3.

5.1.5 TEM Characterization of Regrown Samples

Additional TEM characterization of the regrowth interface of the *nipi* solar cell with the highest reported efficiency of 12.5% which was discussed in Section 5.1.3 was completed. The work was done in collaboration with researchers at Ohio State University (OSU) where the TEM measurements were taken. The sample was prepared by focused ion beam (FIB) to thin and extract a sample from the regrowth interface. The sample was further thinned to allow for high resolution TEM (HR-TEM) imaging.

For the TEM analysis both scanning transmission electron microscope (STEM) and HR-TEM techniques were used. STEM is distinguished by the use of a focused electron beam that rasters over the region of interest to form an image, which allows for additional analysis. HR-TEM uses the wave nature of electrons, which interferes with the crystalline structure of the material to provide atomic level contrast in the material.

The dark field STEM image of the regrowth interface in Figure 5.18 provides some guidance as to the growth defects that have resulted in degraded device performance. Following the v-groove etch the intersection between the (100) and (111)A crystal planes is also where the InGaP layer is exposed. At this location a bright spot is seen in the image, which is indicative of a dislocation that forms at that interface. This is not surprising given the possibility of growth facets forming at this location, and the

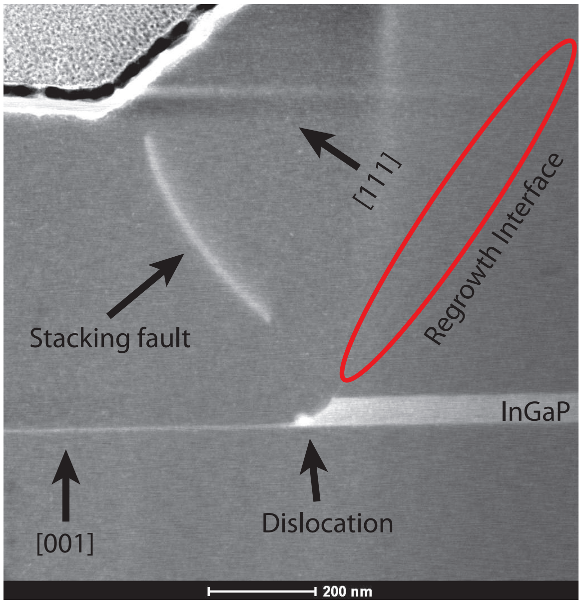

Figure 5.18: A dark field STEM image of the regrowth interface, showing a dislocation at the intersection of the (111)A and (100) planes, a stacking fault that seems to propagate from the dislocation, and increased diffraction at the regrowth interface.

likely degradation in the InGaP surface quality prior to growth. The regrowth process is completed at 620°C which is a temperature at which As is mobile in GaAs and P is mobile in InGaP. The growth chamber is an AsH_3 rich environment to ensure that there is a surface equilibrium that doesn't deplete the crystal of As. This ensures the GaAs remains in it's crystalline state, however it allows for the possibility that InGaP becomes InGaAsP or InGaAs as the As substitutes for P, which would result in strain given the larger lattice constant of InGaAs and increased defect density. This could be alleviated by switching the back surface field (BSF) layer to an As containing material like AlGaAs instead of InGaP. Also seen in the figure is a stacking fault that seems to propagate from the dislocation, which is likely from the same cause.

Increased diffraction is seen at the regrowth interface, both on the (111)A side-wall and on the (100) surface. There are multiple theories as to the cause of the increased diffraction, however no clear conclusions. The out-diffusion of P from the InGaP BSF layer could be exchanged for As in the GaAs, resulting in a thin surface GaAsP layer. It would be assumed; however, that this would appear as a

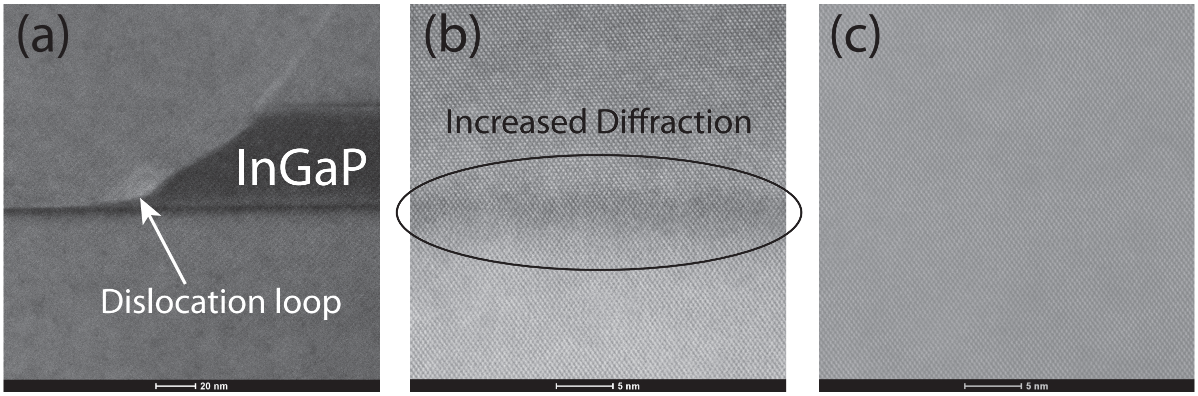

Figure 5.19: Three light field HRTEM images showing (a) the dislocation at the intersection between the (111)A and (100) planes, (b) increased diffraction at the regrowth interface, and (c) the initial growth interface showing no increased diffraction.

darker region in the bright field image since GaAsP would have a smaller lattice constant than GaAs. Alternatively the increased diffraction could be from environmental contamination from the processing prior to regrowth. There could be residue from the etchant, or cleaning process, or residual native oxide that formed after etch prior to loading into the chamber. In an effort to determine the cause of the increased diffraction energy dispersive spectroscopy (EDS) measurements were taken with the STEM to map the material composition of the image. Nothing other than GaAs was seen at the regrowth interface, which did not shed any additional light on the source of the increased diffraction. EDS only has the capability of detecting particles on the order of parts per thousand or up to parts per ten thousand, so low level environmental contamination might not be detectable.

Additional analysis was completed with light field HR-TEM analysis to characterize the crystalline structures at the different interfaces, which is shown in Figure 5.19. Analysis of the regrowth at the intersection of the (100) and (111)A planes in Figure 5.19(a) shows what seems to be a dislocation loop where the GaAs grows direction on the InGaP BSF. Detailed analysis of the image at the growth interface does show an increased bond length in the [001] direction, which could indicate pseudomorphic strain in the growth direction from the strained InGaAs.

The increased diffraction of the regrowth interface along the (100) and (111)A planes was also completed, and is seen in Figure 5.19(b). An increase in diffraction is seen, however no loss in crystallinity or apparent change in lattice constant. It is unclear the cause of the increased diffraction, however an image was also taken of the initial growth interface on the epi-ready surface that is 500 nm beneath the InGaP BSF shown in Figure 5.19(c). This region showed no signs of material contrast with GaAs, indicating that the epi-ready preparation that the substrate underwent prior to growth did not result in the same interface contamination that the v-groove etch and preparation caused.

Additional work is required to improve the interface, eliminating the defects that have been detected through TEM analysis. Switching to AlGaAs would likely limit the formation of dislocations on the BSF surface, however it is unclear if this would affect the regrowth on the (100) and (111)A surfaces. An evaluation of epi-ready preparation processes would be required in order to understand how to eliminate environmental contamination following etch prior to regrowth.

5.1.6 Varying Regrowth Semiconductor

Given the significant improvements witnessed in the epitaxial regrowth structures, it was hypothesized that using a higher bandgap material such as AlGaAs and InGaP for the regrown contact would improve V_{OC}. The concept is similar to using a higher bandgap window layer in a conventional single-junction solar cell, where for a *p-type* regrowth an increased barrier is created for the electrons in the *n-type* layers. The electrons will encounter a larger barrier at the *p-type* contact and be driven back into the majority doped *n-type* layer. At the same time the holes are easily collected from the *p-type* layer that has a negligible barrier to InGaP with 3×10^{18} /cm^3 *p-type* doping.

A simulated band diagram for GaAs to both materials is shown in Figure 5.20 where it shows that a small barrier is formed between the *n-type* AlGaAs and GaAs, and between the *p-type* InGaP and GaAs due to the work functions of the materials. Simulations also show that this should have a negligible

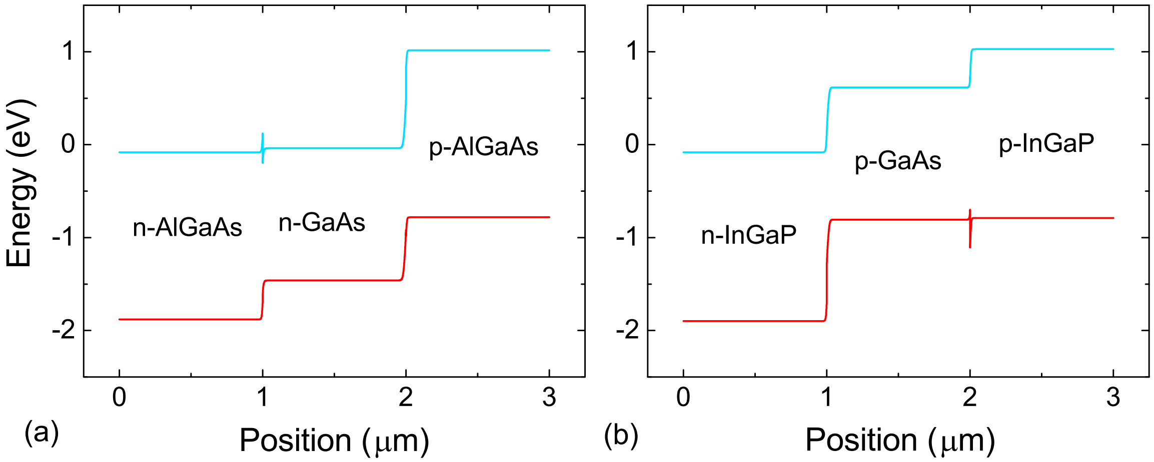

Figure 5.20: A simulated band diagram for the higher bandgap regrowth for (a) *n-type* GaAs to $Al_{0.3}GaAs$ and (b) *p-type* GaAs to $InGaP_2$

Table 5.4: Summary of one sun I-V results for devices growth with varying regrowth semiconductors

Contact Method	J_{SC} (mA/cm^2)	V_{OC} (V)	FF (%)	η (%)	R_s (Ω)	R_{sh} (Ω)	n	J_o (A/cm^2)
GaAs Regrowth	22.2	0.58	63	6.0	1.1	31 k	2.45	$1.95\text{x}10^{-6}$
InGaP Regrowth	21.0	0.66	59	6.0	2.4	27 k	2.12	$1.14\text{x}10^{-7}$
AlGaAs Regrowth	5.2	0.42	54	0.9	3.6	5 k	1.47	$8.43\text{x}10^{-8}$

effect on the series resistance, however using *n-type* InGaP and *p-type* AlGaAs is a better solution. For this experiment keeping both regrowth materials constant was chosen to focus on the characterization of each materials regrowth properties.

The process for fabricating a device with $InGaP_2$ or $Al_{0.3}Ga_{0.7}As$ regrown contacts is identical to that of GaAs, with the only change being the precursors used during the regrowth process. InGaP was grown with nominally lattice matched conditions, however it is known that the surface diffusivity of In and Ga differ, which results in non-lattice matched growth in the v-groove trench due to differences in GRE [79]. Doping for the InGaP regrowth was nominally 6x10^{18} /cm^3, while the $Al_{0.3}GaAs$ was only able to be doped at approximately 3x10^{17} /cm^3 for both contacts with the dopant sources used of DEZn and Si_2H_6.

Test results from one-sun AM0 and dark I-V testing are shown in Figure 5.21, while the metrics

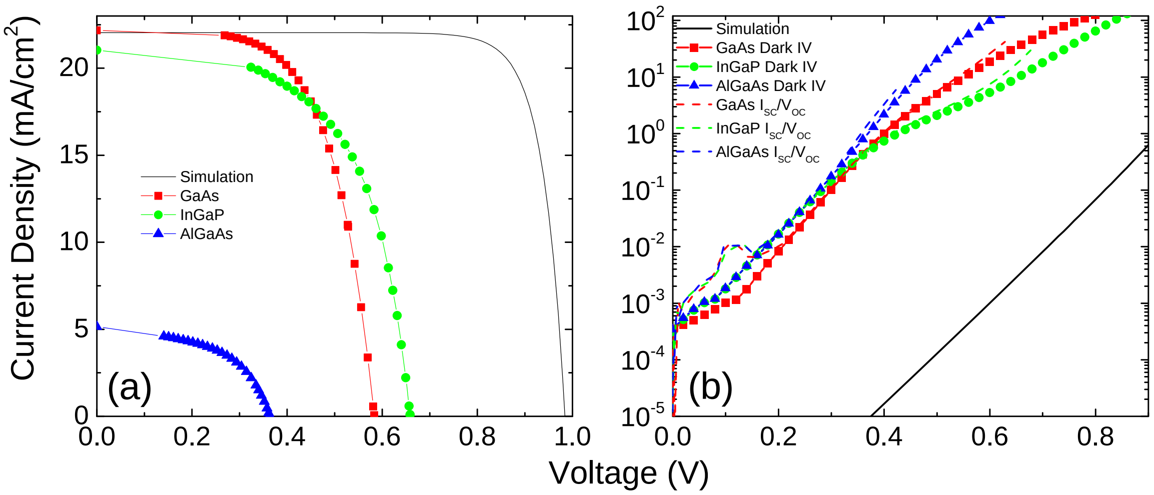

Figure 5.21: (a) One sun AM0, (b) dark I-V, and J_{SC}/V_{OC} curves for devices contacted with GaAs, InGaP and AlGaAs regrowths

and extracted data are shown in Table 5.4. The AlGaAs regrowth resulted in an efficiency of only 0.9%, which is significantly lower than the comparable GaAs or InGaP regrowths. One concern leading to the degraded result is the AlGaAs doping concentration that only reached $3\text{x}10^{17}$ /cm^3 for both *n*- and *p-type* layers. As the doping level is decreased it becomes much more likely that the trap states at the interface can compensate the regrowth, resulting in increased dark current injection and a barrier at the ohmic contacts. This results in an increased series resistance of 3.597 Ω, while also decreasing the shunt resistance by allowing a conductive path along the regrowth interface. A possible solution to the low doping concentration would be to use Te and C as the dopant sources for the regrown contacts to increase the dopant concentration and minimize these effects. Figure 5.22 shows the EQE of the device with AlGaAs regrowth which is degraded with respect to the other regrowths. An integration of the EQE measurement shows that the expected J_{SC} is 16.8 mA/cm^2 for an AM0 spectrum, which is over three times higher than AM0 one sun measurement. It is suspected that the result of the reduced one sun measurement is due to internal series resistances which can result in current loss at J_{SC} if high enough. This would also explain the reduction in EQE between 500 and 900 nm, which is where the lamp intensity of the EQE system is the highest, resulting in the highest current and corresponding

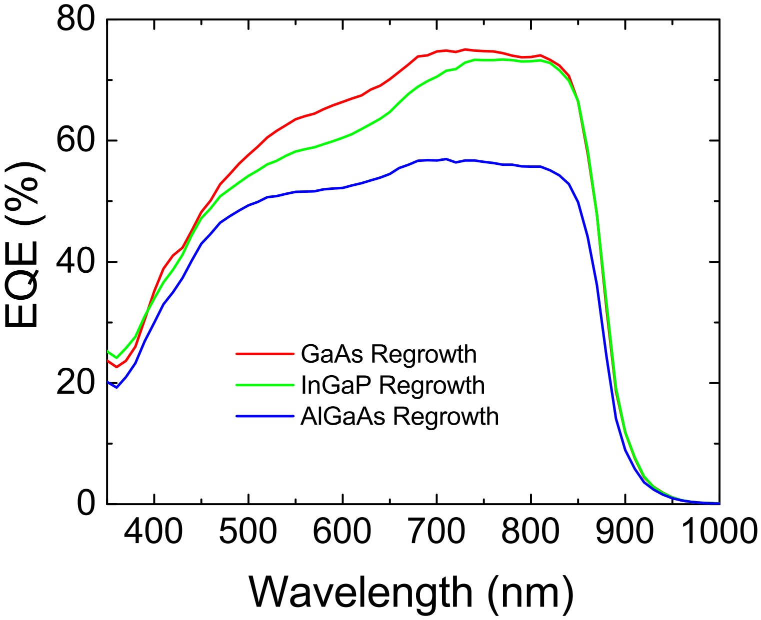

Figure 5.22: External quantum efficiency measurements of devices regrown with GaAs, InGaP and AlGaAs are compared. Measurements were taken on the devices, and were corrected for shadowing losses.

InGaP regrowths were able to achieve an efficiency of 6.0% matching the GaAs efficiency. However, an increase in V_{OC} and a decrease in J_{SC} was measured with respect to the GaAs regrowth. The regrowth of InGaP had poor selectivity, resulting in an increased volume of amorphous growth that nucleated on the selective oxide. Additional processing to mask the regrown trenches would allow the amorphous growth to be etched. However, this was not completed for these devices and a loss in J_{SC} resulted. This can is confirmed in Figure 5.22 where the EQE from the wavelengths less than 670 nm where InGaP absorbes is decreased with respect to the GaAs regrowths.

The InGaP regrowth does result in an increase in V_{OC} relative to the comparable GaAs regrowth, and the dark current measurement has a unique trend. Figure 5.21 (b) shows the dark diode curve for these devices along with the J_{SC}/V_{OC} curves. It can be seen that the InGaP regrowth devices move from a lower ideality regime below 0.3 V to a higher ideality regime between 0.3 and 0.5 V before series resistance begins to dominate above 0.6 V. The shift in diode ideality is related to the recombination mechanisms and not due to series resistance because the same trend is seen in the J_{SC}/V_{OC} curve. The mechanism that leads to this behavior is likely related to the filling of trap states at the regrowth interface, following a similar argument to that presented in Section 3.3 where increased carrier concentration results in a recovery. This can lead to a decrease in sensitivity to trap states at the interface in the InGaP regrowth, resulting in a more robust design.

An additional challenge for InGaP regrowths is related to the dynamics of selectively regrowing a ternary that is sensitive to strain. Since Ga and In have differing diffusivity the composition in the v-groove trench will differ from the composition of planar growth. As a result additional calibration is required to approach lattice-matched conditions for selective growth. Further compounding this difficulty is the compositional variability that can exist within the v-groove trench from the center to the edge, which cannot be eliminated by calibration [79]. As long as the deviation from lattice-matched conditions does not result in layers that exceed the critical thickness, InGaP is believed to be a viable alternative to GaAs regrowths.

5.2 EVALUATION OF DEVICES FABRICATED WITH DIFFUSED CONTACTS

Devices were fabricated with diffused junctions as described in Section 4.2. The tin diffusions were completed at 850°C for 45 minutes, while the zinc diffusions were completed at 750°C for 45 minutes. The one-sun AM0 I-V plots are shown in Figure 5.23 (a), while the extracted parameters from each of the I-V measurements are shown in Table 5.5. For comparison a simulated I-V curve was added to the figure and table, for both the epitaxial regrowth and diffused junction devices.

Contacts formed via SOG dopant resulted in a graded junction in place of the nearly abrupt junction that is formed during epitaxial regrowth. For the rectifying contact it is clear that a graded junction

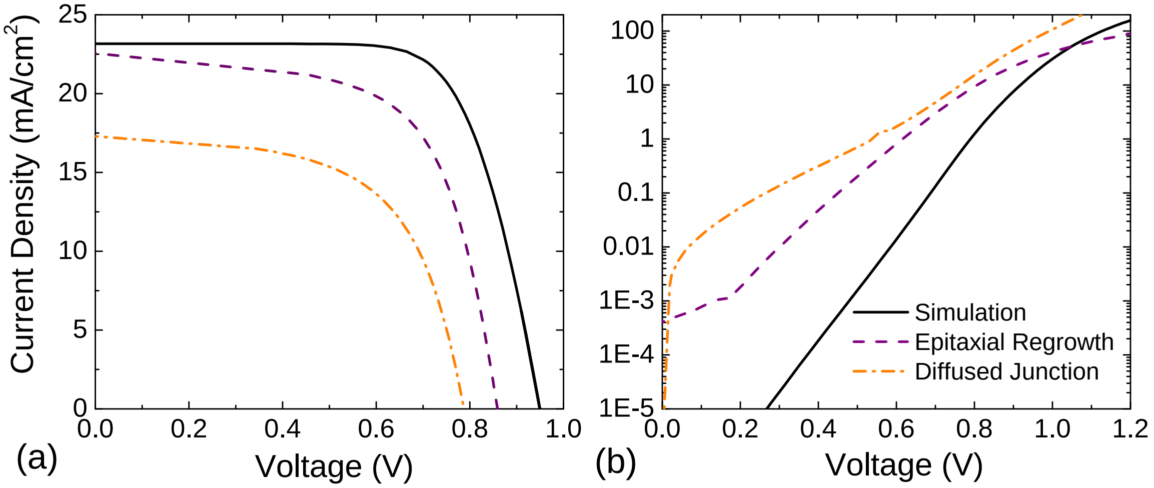

Figure 5.23: (a) One-sun AM0 and (b) dark I-V results for solar cells with epitaxial regrowth and diffused junctions contacted with back side contacts along with device simulations for comparison.

Table 5.5: Summary of the one sun and dark I-V metrics for devices contacted with diffused contacts, compared to simulations of regrowth and diffused contacts

Contact Method	J_{SC} (mA/cm^2)	V_{OC} (V)	FF (%)	η (%)	R_s (Ω)	R_{sh} (Ω)	n	J_o (A/cm^2)
Spin-on Diffusion	17.3	0.79	60	6.0	2.45	3.86 k	2.504	1.14x10^{-7}
Regrowth Simulation	22.21	0.9427	80	12.31	1.08	605 M	1.712	1.68x10^{-11}
Spin-On Dopant Simulation	22.19	0.9415	79	12.09	1.52	519 M	1.648	9.594x10^{-12}

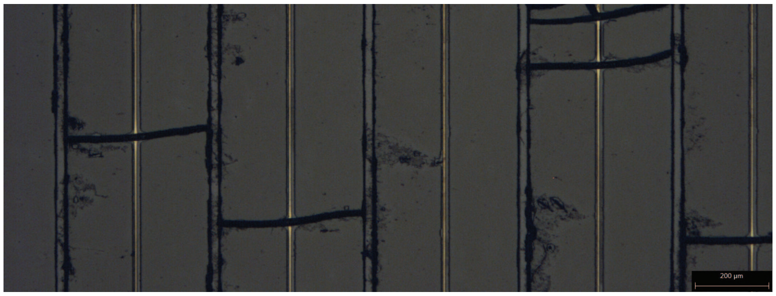

Figure 5.24: Optical micrograph of a fabricated *nipi* solar cell with diffused contacts that formed cracks in the semiconductor surface.

will result in slightly lower rectification. However, simulations show that the effect of this should not degrade device metrics significantly. Two-dimensional simulations completed in Synopsys *Sentaurus* show that the change in V_{OC} was negligible while the FF is reduced to 78.7% for the diffused junction contact from the 80% simulated for a regrown contact. The simulations do not take into account the interface traps that are possible for the regrown device, or the cracks in the crystal that can occur in high temperature diffusions, both of which would degrade the device.

Experimental results from the diffused junction contacts had a relatively low dark saturation current of 1.14x10^{-7} A/cm^2. Dark current is naturally expected to be higher for a *nipi* structure due to the 25 *p-n* junctions that exist within the SL. However, simulated I-V curves result in a dark saturation current of 9.59x10^{-12} A/cm^2 with an ideal interface. Comparing simulated and measured J_o values suggests that defects are created during the diffusion process, either in the *nipi* layers due to the high temperatures or at the diffused contact due to the formation of interstitials or traps.

Some difficulty was encountered with this fabrication method due to the high temperatures of 850°C required for the tin diffusion. At these temperatures the two 500 nm oxide layers and the 300 nm SOG source result in enough residual strain during the anneal to crack the GaAs surface as shown in Figure 5.24 due to the order of magnitude higher thermal expansion coefficients of GaAs when compared to SiO_2. At 850°C thermal expansion results in a stress of 2.16x10^8 N/m^2 assuming the materials are strain-free at room temperature, while the tensile strength of GaAs is 2.7x10^9 N/m^2. Although it is clear

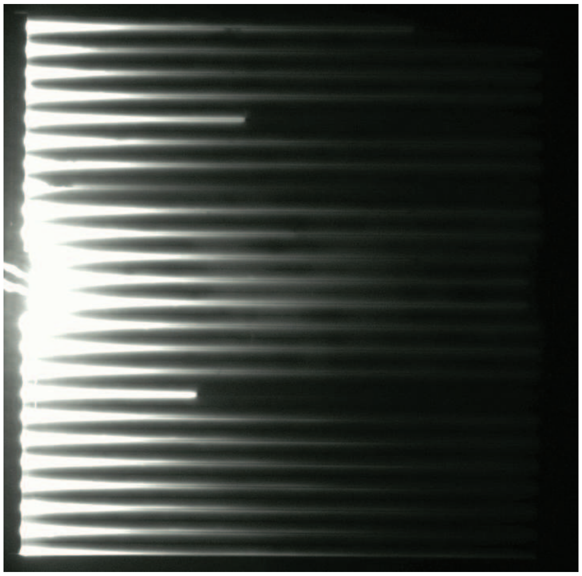

Figure 5.25: An electroluminescence image taken in a microscope of a diffused junction device that shows multiple grid fingers not emitting due to cracks in the GaAs surface.

that SiO_2 should not create enough stress to crack GaAs it is likely that the thermal expansion coefficient of the SOG does not match SiO_2, which would result in a much larger strain on the wafer. Visible cracks contribute to a shunt path in the device, explaining the increased dark current and reduced V_{OC} from what was expected via simulation.

Cracks through the epitaxial layers reduced the current to 17.3 mA/cm^2 from the 22.19 mA/cm^2 expected from simulation. Electroluminescence imaging shown in Figure 5.25 determined that multiple regions between grid fingers were not emitting. The regions with cracks correlated with the loss of emission, leading to the reduction in current. Another mechanism that resulted in current loss was due to a thin film that was not fully removed following the tin diffusion. The EQE in Figure 5.26 shows loss in the visible with respect to the GaAs regrowth device, likely due to absorption and scattering in the thin film. It is possible to remove this film with more aggressive plasma etching.

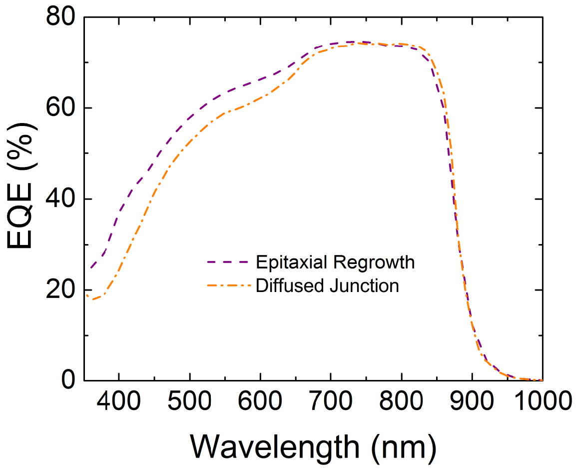

Figure 5.26: EQE measurement of the device fabricated with the diffused junction process compared to the epitaxial regrowth process.

5.3 CONCLUSIONS

This chapter represents the bulk of the work completed for this thesis, and demonstrates the significant progress towards the development of *nipi* solar cells. The progress made in developing a fabrication process for *nipi* devices was detailed, discussing the major advancements in understanding of the epitaxial regrowth process, and characterizing alternative methods for fabrication.

The first major advancement was to move from a dual front side contact design to using a design that has front and back-side contacts. This eliminates the formation of a shunt path between the metal contacts, and increased efficiency from 3.4% to 9.0%. Additional improvements were gained by completing the v-groove etch process at NASA GRC instead of at Rochester Institute of Technology (RIT), reducing the delay between etch and regrowth which resulted in an lower overall dark current and improved V_{OC}.

An optimization study of the regrowth preparation processing conditions was also completed, leading to further improvements in device performance to 9.14% efficiency prior to ARC and a new record efficiency for *nipi* solar cells at 12.5% following ARC. The characterization of the regrowth process showed that any additional chemical processing or cleaning steps after etch prior to regrowth ended up degrading the solar cell. It was also determined that although there was no statistically significant difference between using a v-groove etch and a dovetail etch the dovetail etch did result in a slight improvement of 0.65% to device efficiency. Analysis of the highest efficiency solar cell before and after ARC did indicate that the ARC improved the dark current by providing passivation to the side-walls of the *nipi* SL.

Further analysis of the high efficiency devices was also completed by measuring them under concentration, where the pre-ARC efficiency was increased to 9.93% at 7.4 suns. An improvement in V_{OC} was seen, improving from 0.77 V at one sun to 0.98 V at 27.6 suns, which was concluded to be due to a carrier concentration filling of trap states at the regrowth interface. This was corroborated by modeling which was used to fit a trap density of $4x10^{14}$ /cm^3 with the trap energy at mid gap. TEM characterization of the regrowth interface also confirmed the existence of defects, likely propagating from the InGaP BSF layer. Additional defects are likely caused by environmental contamination from processing.

Variants of the carrier selective contact formation process was also completed. Using the epitaxial regrowth process, the regrowth material was changed from GaAs to InGaP and AlGaAs to evaluate the effect of increasing the rectifying barrier height. Growth and doping limitations contributed to the poor performance of the AlGaAs regrowth, however the InGaP regrowth showed promise with an improved V_{OC} over the GaAs regrowth control device. Another alternate fabrication method was completed with a diffused junction process, utilizing a SOG dopant to form the carrier selective contacts. Multiple challenges were encountered due to the high temperature of 850°C required to drive in the tin *n-type* dopant, resulting in cracks in the epi surface. However, if the formation of cracks can be eliminated this process also shows promise.

Chapter 6

Optical Characterization of *nipi* and QD-*nipi* Superlattices

A significant amount of resources in recent years has been placed in work directed towards the development of an IBSC [80, 23, 81]. As discussed in Section 1.1 the IBSC has three transitions within one bulk bandgap, simultaneously reducing the energy losses from thermalization and transmission with the optimal bandgap alignment [22]. Traditionally this work has been pursued with single-junction devices with the intermediate band region consisting of QD or QW in the intrinsic region [82, 83]. One of the difficulties with this approach is the need to have the confined level at the Fermi level of the host semiconductor [84], which is very difficult to achieve for multiple QD or QW in one intrinsic region due to band bending. A strength of the *nipi* design is that QD can be placed in either the intrinsic or doped layers while minimizing recombination loss due to the short diffusion length requirements. Additionally QD can be placed in each of the multiple *nipi* periods, resulting in an increase in the total QD volume and subsequently total absorption via QD energy states.

A concept of what a *nipi*-IBSC band diagram could look like is displayed in Figure 6.1. The intermediate band is formed in the *n-type* region of the SL, which with proper doping levels would allow the QD states to be partially filled. The three transitions that would occur in an IBSC are depicted with the first transition between the VB and IB, followed by the IB to CB, while the third transition is the bulk transition from the CB to VB. There would also be interaction between the *nipi* confined states and the QD states. It is possible that the spatially indirect transitions would occur at much shorter wavelengths through the QD states as shown in the fourth transition, and it is important that this be avoided or have a low probability to ensure that the three desired transitions are dominant.

The use of QD within a *nipi* stack provides a simple method for changing the electric field in which the QD exists. In a conventional solar cell the QD are typically placed in the intrinsic region, which has a varying electric field depending on how close the QD is to the base or emitter. With the *nipi* design having multiple junctions a few QD can be placed in each junction within a region of specific electric field. Adjusting the electric field in which a QD exists has many implications which will be discussed here. A field is required to separate the carriers from the QD and limit recombination, however too great of a field can result in increased SRH recombination. Also a field can shift the confined energy levels via the quantum confined Stark effect (QCSE). Finally a high electric field can increase the escape probability of a carrier from the QD by thinning the barrier, increasing the probability of tunneling escape. A part of this study will be a characterization of the effect of changing the field in which the QD exists.

6.1 GROWTH & EXPERIMENTAL

Doping SL test structures were grown on semi-insulating (100) GaAs wafers with a 2° offcut towards the (110) direction. All wafers were double-side-polished to allow for transmission measurements. Six *nipi* test structures were grown with various thicknesses and doping levels with and without QD in

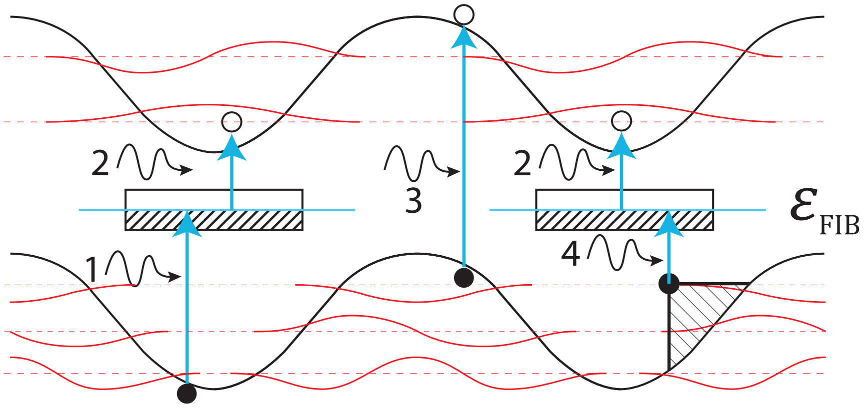

Figure 6.1: Band diagram depicting a QD-*nipi* IBSC concept device with three absorption pathways. 1) from VB to IB, 2) from IB to CB, 3) from VB to CB, and 4) from *nipi* confined level to IB

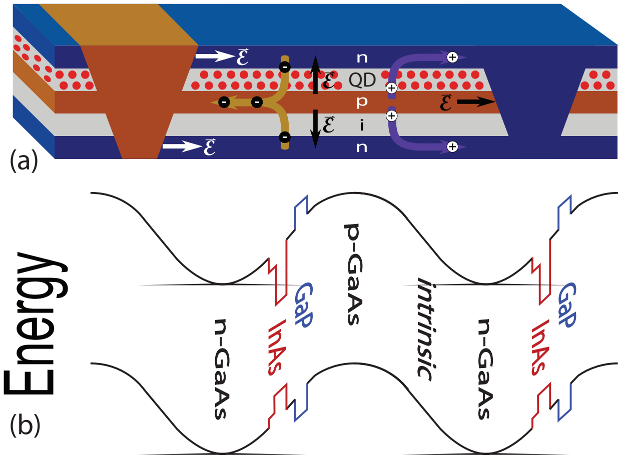

Figure 6.2: (a) Cross section of a QD-*nipi* superlattice solar cell with lateral carrier transport depicted. (b) A simplified band structure of a vertical slice through the QD-*nipi* superlattice

the SL to characterize the effect of the doping SL on absorption and photoluminescence (PL). Repeat period thickness of the SL was varied from 50 to 100 nm, and the doping levels were varied as shown in Table 6.1. Each period has four GaAs layers of equivalent thickness, consisting of *n-type* / intrinsic / *p-type* / intrinsic doped layers. The doping level was changed to modify the built-in potential which is also shown in Table 6.1, which increases for the test structures with higher levels of doping.

Two of the *nipi* devices were grown with QD inserted in one of the *i*-regions of the *nipi* stack. InAs dots were grown on the GaAs surface through the Stranski-Krastanov (S-K) growth mode [32], and

Table 6.1: Summary of the *nipi* test structures grown with and without QDs

Layer thickness (nm)	Period thickness (nm)	Doping (/cm^3)	V_{bi} (eV)	# Repeats	QD Layers	QD Location
12.5	50	1x10^{18}	0.17	48	0	n/a
12.5	50	6x10^{18}	1.02	48	0	n/a
12.5	50	6x10^{18}	1.02	48	1x	*i*-region
25	100	1x10^{18}	0.68	24	0	n/a
25	100	3x10^{18}	1.42	24	0	n/a
25	100	3x10^{18}	1.42	24	2x	*i*-region

were strain compensated with a GaP layer to balance the highly compressive strain in the InAs layer as depicted in Figure 6.3 [27]. Growth of QD by the S-K growth mode results in the formation of a 2D wetting layer, which is planar film on the order of a few monolayers. This forms prior to a critical thickness where the formation of QDs occur, which distinguishes S-K growth from Volmer-Weber (V-W) growth which has no wetting layer prior to formation of QD as islands. The QD stack consists of InAs and GaAs layers grown at 475°C, followed by a GaAs/GaP/GaAs stack grown at 590°C. The total thickness of the QD stack is 13 nm, as measured by x-ray diffraction. The QD stack replaced one of the 12.5 nm intrinsic regions in each of the 24 periods of the 50 nm pitch QD-*nipi* device. One period of the 1x QD device is depicted in Figure 6.2. Similarly, two QD layers were grown in the intrinsic region of the 100 nm period structure, which had a total of 6 *nipi* periods. Additionally, a sample with ten repeats of the same InAs/LT GaAs/HT GaAs/GaP/GaAs stack described above and shown in Figure 6.3 with no *nipi* SL were grown as a baseline comparison for the QD-*nipi* structures.

For the devices grown, absorption was measured using a Perkin-Elmer UV-Vis spectrophotometer. The absorption coefficient was calculated using (6.1) by comparing the transmission (T_{GaAs}) and reflection (R_{GaAs}) of a bare substrate to the transmission (T_{nipi}) and reflection (R_{nipi}) of a similar wafer with a *nipi* SL. In (6.1), λ is the wavelength, and t is the thickness of the structure grown. In (6.2), $A(\lambda)$ is the percent absorption, and t is the thickness used for the absorption calculation, which is 2.5 μm for

Figure 6.3: (a) An illustration of the QD stack including stain compensation, and (b) an AFM image of QD grown on GaAs.

the doping SL structures and 650 nm for the equivalent of 50 QD periods.

$$k(\lambda) = \frac{(T_{GaAs} + R_{GaAs} - T_{nipi} - R_{nipi}) * \lambda}{4 * \pi * t} \tag{6.1}$$

$$A(\lambda) = 1 - 10^{\left(-4*\pi*t*k*\lambda^{-1}\right)} \tag{6.2}$$

PL was measured using a 514.5 nm CW argon laser, to excite the carriers. The luminescent signal was measured with a Horiba iHR-320 monochromator mated with a Stanford Research SR830 lock-in amplifier. Temperature-dependent measurements used a liquid He cryostat with a built-in substrate heater to cool the temperature to 10 K and control it at any temperature up to 360 K. time-resolved PL (TRPL) was measured using a Fianium WhiteLase continuum laser with an acoustic optical filter for exciting the carriers. Single photon counting was completed with a iHR-320 monochromator mated with a Hamamatsu H10330A photomultiplier tube for single photon counting.

To date, no QD-*nipi* devices have been fabricated. To explore the properties of the QD-*nipi* SL, it was decided to evaluate test structures by spectroscopic means. This allows the understanding of absorption, carrier transitions and lifetimes, which can guide in the proper selection of SL conditions to use in a solar cell.

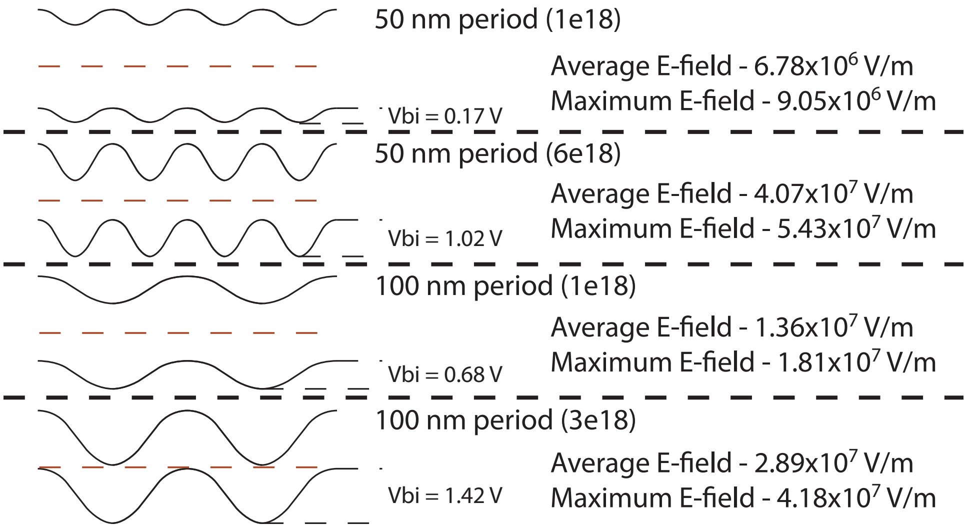

Figure 6.4: Band diagrams showing the built-in voltage for the four *nipi* superlattice designs evaluated here.

6.2 SPECTROSCOPIC ANALYSIS

6.2.1 Absorption

Absorption coefficients were extracted for the four *nipi* structures without QD, and the percent absorption was calculated for an effective thickness of 2.5 μm for each doping SL as shown in Figure 6.5 (a). A direct correlation between absorption for a structure and the built-in voltage due to the doping SL was demonstrated. Using Poisson's equation, the V_{bi} was calculated using (2.3) and (2.4) to be 0.17 and 0.68 V for the structures doped at 1x10^{18} /cm^3 with 50 nm and 100 nm pitch, respectively, as shown in Figure 6.4. Separation increases to 1.02 V and the maximum built-in voltage of 1.42 V for the 50 and 100 nm devices with higher doping. The trend of increasing absorption versus built-in voltage corresponds directly with theory and calculations discussed in Section 2.3.

Doping SL structures absorb in the subband regions due to confinement between the similar type doped layers in the SL. The band structure creates QW as shown in Figure 6.1 that are parabolic in

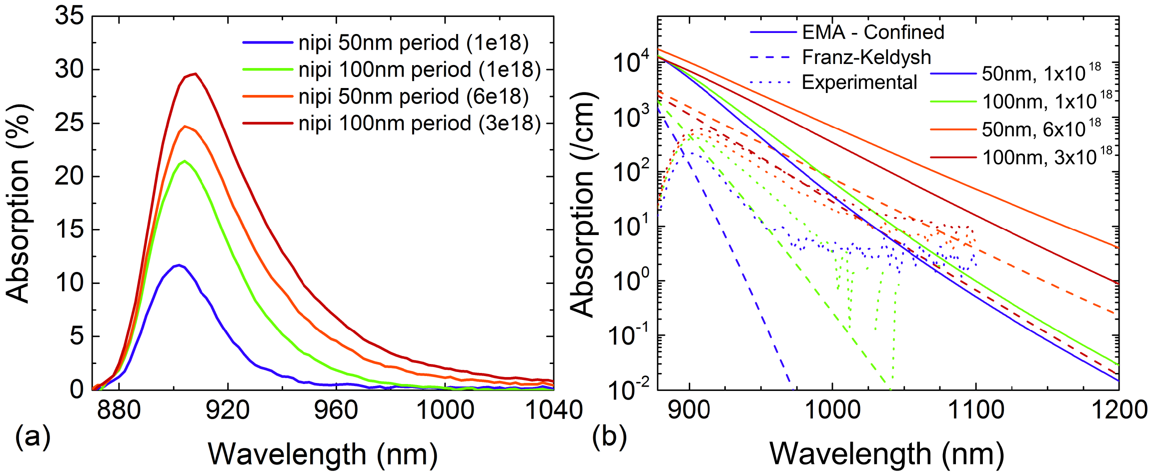

Figure 6.5: (a) Percent absorption calculated for 4 *nipi* structures with 50 and 100 nm periods, with varying doping levels, and (b) measured absorption compared to theoretically calculated absorption.

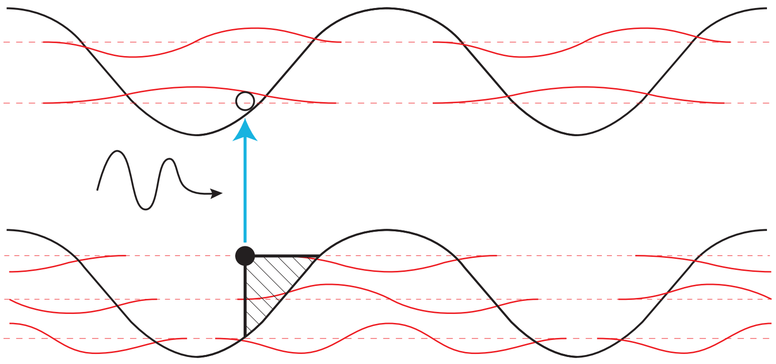

Figure 6.6: A quantum confined *nipi* band diagram that depicts the spatially indirect transition that requires penetration into the triangular barrier shown.

shape. Energy levels can be found in the wells by applying the harmonic oscillator solution of $E_n = \hbar\omega(n + 1/2), n = 0, 1, 2, ...$ States are formed in the CB of the *n-type* region and the VB of the *p-type* region. Interband absorption occurs from the spatial overlap of the confined states within each of the wells. Absorption increases as the energy level index n increases due to the corresponding increase in overlap between the confined levels [11]. The fundamental absorption processes occurring in the *nipi* structure are similar to that of a type-II SL. A band diagram depiction of the spatially indirect or type-II transition is shown in Figure 6.6 where the carrier must tunnel through a triangular barrier prior to the being excited by a photon.

As the doping level and period spacing are increased the average and maximum electric fields within the *nipi* layers are also increased as shown in Figure 6.4. This results in an increased absorption as shown in (2.20) and (2.21) which relates the F-K absorption effect to electric field strength. Also the overlap of subband states is related to the sharpness of the band bending, largely driven by field strength as shown in (2.23) and (2.24). As the electric field increases the overlap between the confined levels increases, resulting in more absorption through the confined levels. Theoretical calculations have been completed and are compared to the experimental results in Figure 6.5 (b). The trend seen in experimental measurements follows what is theoretically calculated where the absorption tends to increase as the electric field is increased.

Theoretical calculations do exceed the experimentally measured absorption, which can result from two sources. Primarily there was a large amount of uncertainty in the measured absorption. The absorption was calculated from four separate measurements on two samples; reflection and transmission measurements on a substrate with no epi layers, and one with the SL structure. A method of removing the substrate and measuring transmission more directly would be preferred to eliminate some of the sources for cumulative error. The second source of divergence would come from the simplifying assumptions used in the theoretical calculation, such as the parabolic solution to the Schrödinger equation, and only accounting for two bands instead of a full eight band solution. Regardless of the simplifications the trends match very nicely and help describe the results.

Due to the increased absorption in the structures with higher doping levels, these structures are used as the base structure into which QD are grown. The structure of the device was described previously. Comparisons can be made between a 10x QD stack, and *nipi* structures with and without QD grown in the intrinsic regions.

Almost a doubling of the maximum absorption at 915 nm is seen following the addition of QD to the *nipi* stack, with slight changes in the spectral shape of the absorption curve depending on the number

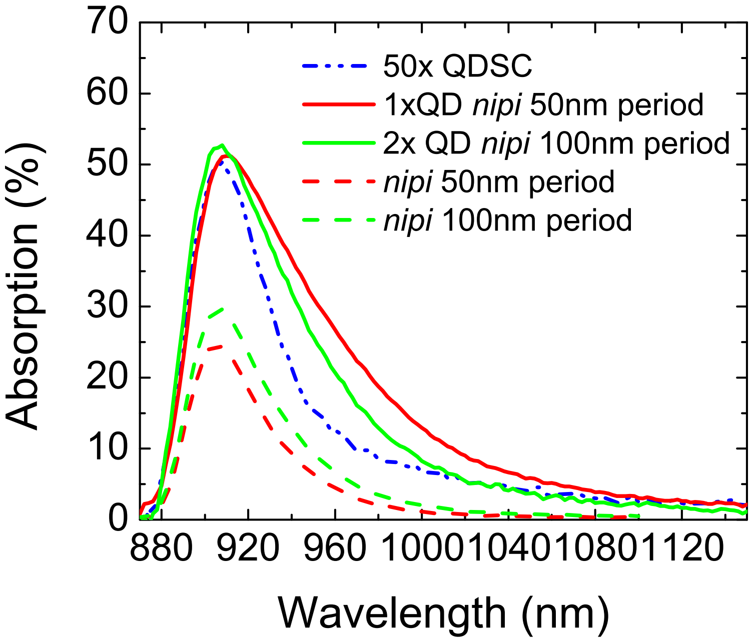

Figure 6.7: Percent absorption calculated for 2.5μm of the *nipi* and QD-*nipi* stacks, compared to the absorption in the total number of QD layers that would be grown in a *nipi* stack of that thickness

of QD layers in each intrinsic layer. Figure 6.7 plots the percent absorption calculated from extinction coefficient measurements for the various structures. Although the structures tested had varying thicknesses, the expected absorption was calculated for 2.5 μm of the doping SL structures, and for 50 QD layers. Fifty QD layers are plotted as a comparison because it is equivalent to the total number of layers that would be grown in a 2.5 μm *nipi* stack given one QD layer every 50 nm period or two QD layers every 100 nm period.

When comparing absorption in the QD-*nipi* structures, it is apparent that the shape of the 1x and 2x QD-*nipi* curves differ. Although the number of QD layers in both devices is the same, the 1x QD device has higher absorption between 930 and 1100 nm, but slightly lower absorption in the wetting layer before 920 nm. It can also be seen in Figure 6.7 that the absorption in the 1x QD structure between 940 and 1040 nm is greater than the sum of the component *nipi* and QD parts. This effect comes from the electric field that exists in the QD and wetting layer due to the built-in field from the doping SL. The

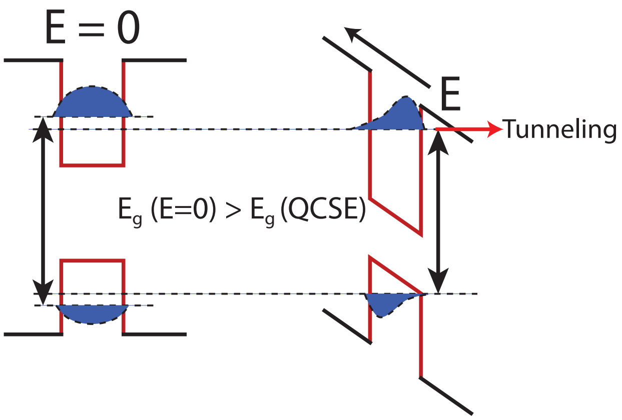

Figure 6.8: An illustration of the effect of electric field on an energy level confined within a quantum dot, increasing the energy gap and spatially separating the electron and hole sub-bands.

field at the spatial location of the QD reaches 5.43×10^7 V/m for the 1x structure which is slightly higher than the field of 4.18×10^7 V/m generated in the 2x structure, both of which are significantly higher than the near zero field in the non-*nipi* QD stack. The field through the confined layers results in the QCSE shifting the energy of the QD absorption peak [85]. The QCSE lowers the electron subband, while raising the hole subband, thereby reducing the bandgap of the confined state within the QD as depicted in 6.8. This increases the absorption in the infrared (IR) for QDs placed in the higher field regions.

The increase in absorption further into the IR is required for the development of the IBSC. In order for the IBSC to function, the subband state has to have a high absorption coefficient to attain high quantum efficiency in each of the absorption bands. Placing QDs within the high-field *nipi* layers does result in a peak shift towards the IR, and the absolute absorption can be increased further as more QD layers are grown in the *nipi* structure. An additional benefit of growing QDs within a doping SL is that the number of QD layers can be easily increased by placing them in any of the doped or undoped layers, further improving absorption in the subband state. This can be done without significant increase to the recombination rate, because the continuously varying electric field through the device will quickly collect carriers.

6.2.2 Photoluminescence

Another effect of the high electric field on the QD within the structure is a change in the characteristics of the excited states within the confined regions, which can be probed through various PL methods. Steady state PL was used to compare the peak positions between the baseline *nipi*, QD, and two QD-*nipi* structures. Peak positions were extracted by fitting multiple Gaussian peaks to the PL measurements plotted in Figure 6.9. The baseline *nipi* structure emits from the GaAs band edge, and has one subband peak at 1.37 eV due to confinement within the doping SL. The 10x QD baseline shows that emission peaks in the QD of 1.35 eV and 1.18 eV were found for the wetting layer and the QD energy level, respectively. The wetting layer peak stays constant for each of the samples, but the QD emission is modified by the electric field and a second peak is clearly distinguished for both of the QD-*nipi* samples. The second peak results from a second electron sub-band which is at a lower energy level, increasing the confinement in the QD-*nipi* device due to the QCSE. The lower energy peak is referred to as the ground state, and the higher energy peak would be the excited state in the QD. For both the 1x and 2x QD structure, two peaks are seen in each sample at 1.23 eV and 1.14 eV. The higher electric field present within the QD-*nipi* samples resulted in the QCSE in the QD energy levels as previously discussed, and shown in Figure 6.9 (black dashed curve to red or green).

The shift of 40 meV seen in the ground state between the QD to QD-*nipi* structures corresponds to theoretical calculations [86]. Since both QD-*nipi* structures have very similar electric fields through the intrinsic region, it is not expected that energy shifts would be seen in the QD peak emission. This has been verified experimentally, since changes in peak positions between the two QD-*nipi* structures were within the error of the fit.

Shifts to lower energy due to the electric field in the structure are beneficial for the InAs/GaAs QD system. One of the difficulties in using this system for the IBSC device continues to be that strain

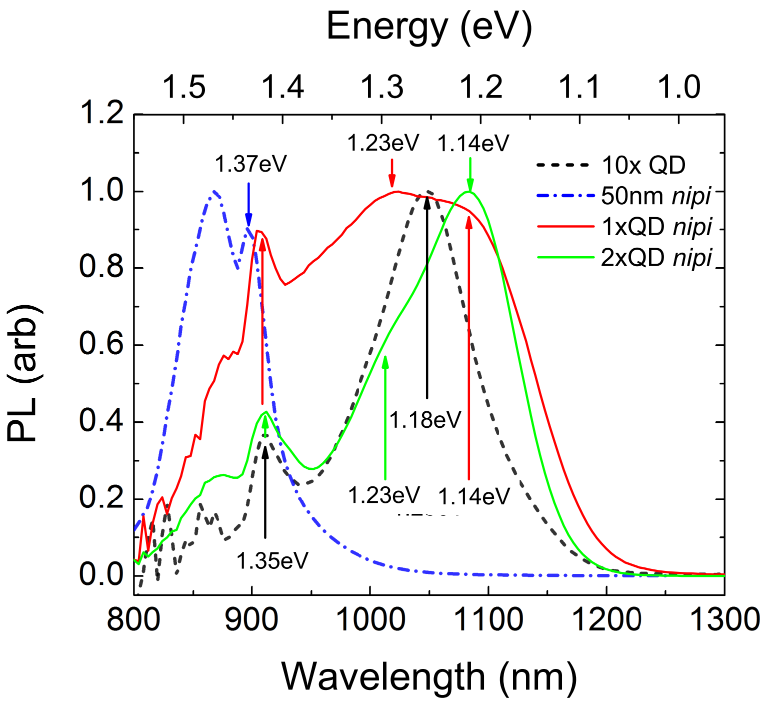

Figure 6.9: Photoluminescence from baseline *nipi*, QD, and QD-*nipi* structures, demonstrating shift in emission wavelength due to the doping superlattice.

raises the QD confined states existing too close to the GaAs CB at approximately 0.3 eV [87, 23]. The lower CB offset leads to difficulties extracting the carriers through photons since carriers can easily escape from the dot via phonons or tunnelling. As a result, the 40 meV reduction in energy gap slightly increases the tunneling barrier in this structure.

To further characterize the effect of the *nipi* structure on QD, temperature-dependent PL (TDPL) was measured to extract the activation energy. TDPL was taken through tempearture from 10K to 360K for each sample, and the lower energy peak of each scan was fit with a Gaussian. The integrated PL intensity versus temperature for the each of the test structure is shown in Figure 6.10. Activation energy was found by fitting the curve with the following equation [88]

$$I(T) = I_O \left[1 + C * exp \left(-\frac{E_A}{k_B * T} \right) \right] \tag{6.3}$$

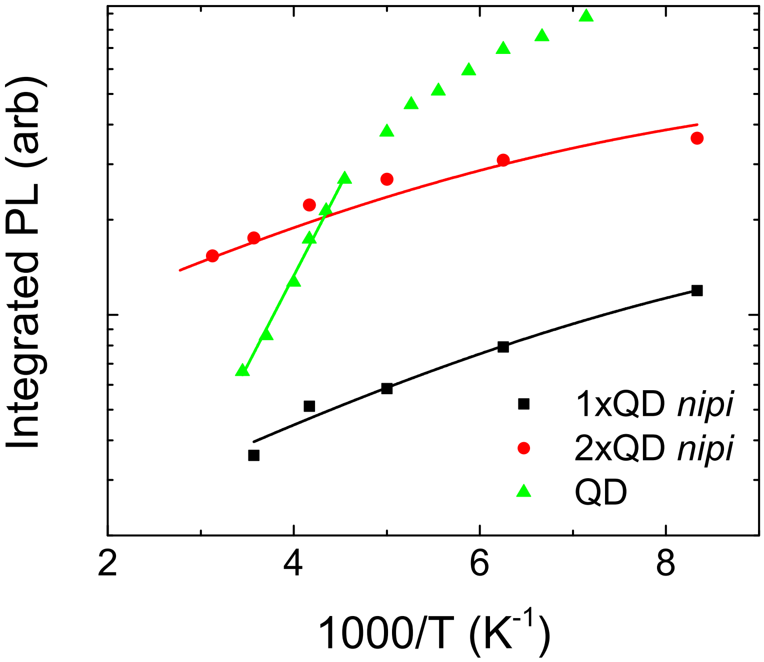

Figure 6.10: Arrhenius plot PL intensity versus temperature, with the activation energy fits shown with solid lines.

where I is the integrated PL intensity, I_O is the PL intensity at absolute zero, C is a fitting parameter, E_A is the activation energy, k_B is the Boltzmann constant and T is temperature.

Extracted activation energies for the QD-*nipi* structures were found to be 30.5 and 30.3 meV for the 1x and 2x QD samples. This is lower than activation energies found for InAs QD grown in GaAs by others between 95 and 125 meV [89, 90], and measured in the 10x QD sample at 113 meV.

Reductions in activation energy demonstrate that carriers are escaping from the dot states at lower temperatures. The QDs in each of the samples are physically the same. The only difference is that the dots in the QD-*nipi* structures are within the high electric field of the doping SL. The field modifies the GaAs barrier, forming a thinned triangular barrier which allows thermally assisted tunneling to occur at decreased temperatures depicted in Figure 6.8, reducing the activation energy [90]. The QDs within the baseline structure are within a much weaker electric field, and therefore have a larger barrier, which limits tunneling escape.

A decrease in activation energy is not desirable for the IBSC because it is preferable to excite carriers out of the dot states via a photon. The tunneling process through which carriers are escaping result in a loss of V_{OC} for a solar cell. However, the tunneling barrier can be increased by placing the QD within either of the doped regions of the structure, where the field is reduced, or by designing the strain compensation layers to act as a tunneling barrier. The activation energy can be further increased by changing the host material to InGaP or AlGaAs, which would increase the VB offset due to the increased bandgap in lattice-matched InGaP.

Additional testing was completed by measuring lifetimes at room temperature through TRPL. QD-*nipi* samples were excited nonresonantly with multiple laser channels, which ranged from 608 to 657 nm with a fluence of 3.9 W/cm^2 and pulse repetition rate of 5 MHz. The QD sample was excited with a single channel 700 nm, with a fluence of 6.1 W/cm^2 at 20 MHz. The PL signal was measured through a monochromator set at steady state PL peak wavelength. Lifetimes were extracted from the temporal scans by fitting the data to the equation $PL(t) = A * exp(-\frac{t}{\tau})$ where A is the amplitude of the curve, t is time, and τ is the decay time constant. Lifetime measured by TRPL is effectively a sum of the radiative, non-radiative, carrier escape and capture rates. Carriers are captured during the pulse in the QD and as the carrier concentration is decreased the PL intensity correspondingly decreases.

As a baseline, the lifetime for the QD device was measured, and a single exponential was used to fit to the curve plotted in Figure 6.11. The decay rate was found to be 1.64 ns, which compares well to previous results [91]. The use of a single exponential fit versus bi-exponential has been, and the source and meaning of each decay rate has been discussed by many authors with no definitive conclusion [92, 93]. The source of the decay rate has complex origins, which depend on the carrier depopulation events such as radiative and non-raditaive recombination and how they compare to the carrier re-population events such as electron capture from the bulk or carriers relaxing from higher energy states.

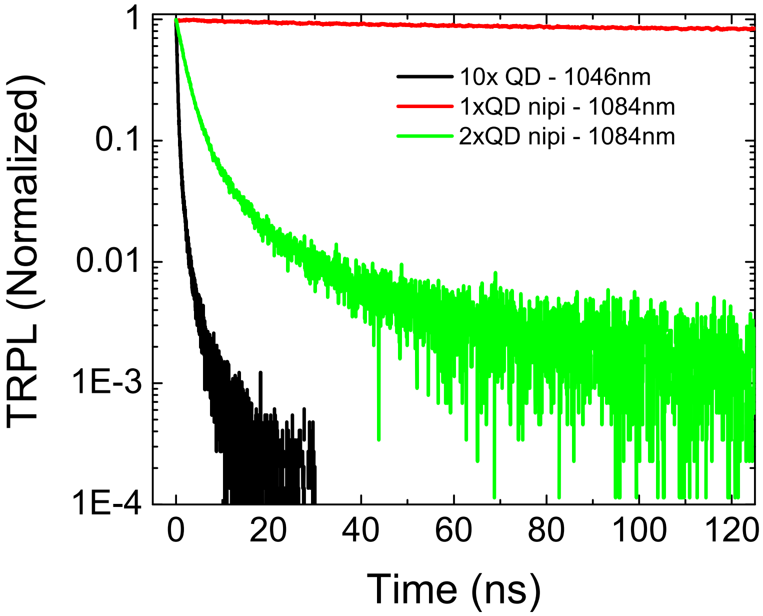

Figure 6.11: Time resolved photoluminescence for QD and QD-*nipi* samples.

It is apparent however that the lifetime in the QD-*nipi* samples are much longer for the peaks measured. The 2x QD sample has a bi-exponential decay curve that results in two time constants of 2.11 ns and 11.14 ns. The shorter lifetime is close to that of the dot decay rate; however, the second constant is nearly an order of magnitude higher. Two mechanisms are possible for the longer lifetime. The QCSE spatially separates electrons and holes, which increases the radiative lifetime of confined states within an electric field [94]. Second, since the sample is non-resonantly pumped, it is possible that the long lifetime carriers in the majority-doped region of the *nipi* SL are filling the QD states as they are recombining radiatively. This is possible because the doping SL extends the lifetime of GaAs by spatially separating carriers in the *n*- and *p-type* layers as discussed in Section 2.2. Due to the spatial separation it is less probable that carriers recombine through the GaAs bandgap, but will recombine through the QD as shown in Figure 6.12 because it provides the quickest recombination pathway.

For the 1x QD sample, two decay constants were approximated to be 48 ns and 1.6 μs. Due to equipment limitations, the sweep was not fully decayed during the laser pulse, resulting in increased

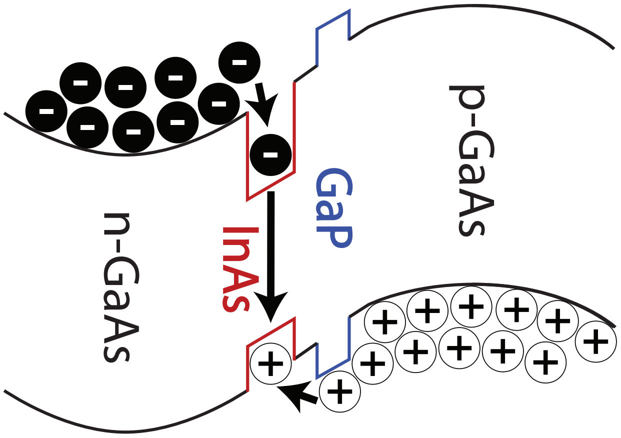

Figure 6.12: Band diagram of a QD-*nipi* period with the majority carrier population in the doped layers recombining through the QD.

uncertainty in the fit. The mechanisms that result in the multiple decay constants is unclear. However, it is evident that decreasing the number of QD layers within the *nipi* stack results in a dramatic increase in the recombination lifetime in the structure. Theoretically, the lifetime of the *nipi* structures with 50 and 100 nm pitch should be similar [15]; however, the addition of a second QD layer dramatically decreases the time constant. Two effects are expected to play a role in the increased recombination rate for the 2x QD device. The second QD layer increases the recombination pathways by doubling the QD volume within a *nipi* period, thereby leading to a reduction in lifetime. Additionally, the 50 nm period device has an average electric field strength of $4.08\text{x}10^{5}$ V/cm, nearly double that of the 100 nm period device of $2.84\text{x}10^{5}$ V/cm. The higher average field will keep carriers confined within the doped layers instead of filling the QD states where recombination will occur. To verify whether the effect is due to the second QD layer or the *nipi* period thickness, future work could investigate adding a single QD layer within a 100 nm period *nipi* structure.

Further testing was attempted to resonantly pump the QD-*nipi* structures to determine if the lifetime in the QD was changed, or if the longer measured lifetime was coming from carriers in the *nipi* SL. This was not able to be completed due to the lack of a laser with enough luminance at the QD absorption

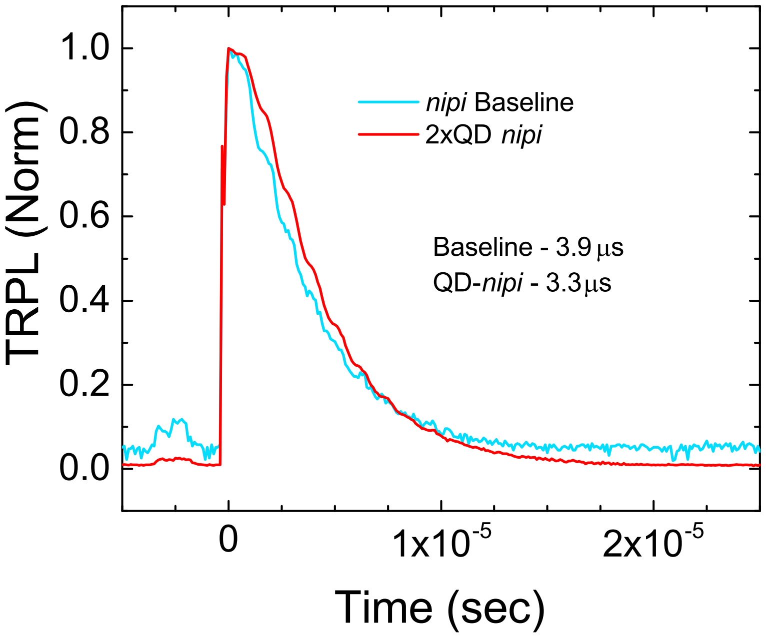

Figure 6.13: TRPL measurements of *nipi* baseline and QD-*nipi* test structures with 100 nm *nipi* periods.

edge and equipment limitations for measuring lifetimes greater than 100 ns at wavelengths greater than 1 μm. Another method to determine the source of the longer lifetime was attempted by measuring TRPL at 900 nm for the *nipi* baseline structure corresponding to the sub-band absorption, and 960 nm for the QD-*nipi* structure corresponding to the QD wetting layer shown in Figure 6.13. This data shows a clear explanation given the close match between the lifetime of the *nipi* SL with and without QD. The longer lifetime seen from the QD emission at 960 nm is due to the longer lifetime in the *nipi* SL that allows carriers to recombine through the QD.

The enhancement in lifetime in a *nipi* SL is due to the spatial separation of excess carriers into the doped regions which limits recombination discussed in Section 2.2. Carriers cannot easily recombine from the GaAs bandedge, so they diffuse to the QD region where they can more easily recombine through the QD. As was discussed previously the measured lifetime depends on both emission and capture processes, here the recapture process has a very long lifetime whereas the emission process has a relatively short lifetime, allowing the long lifetime of the *nipi* SL to determine the lifetime measured from the QD.

The clear benefit for photovoltaic devices with a QD-*nipi* structure as the absorbing material is that the absorption increases in the subband portion of the spectrum. This allows greater collection of carriers further into the IR, and therefore increased efficiency. For a conventional solar cell application, the reduction of the thermal activation energy is a benefit for collecting carriers from the QD states in the device. It takes very little energy to excite the absorbed carrier from the confined state, resulting in increased collection efficiency. Although this is a benefit for the collection of carriers, a decrease is expected in the open-circuit voltage due to escape via tunneling. As previously discussed, the reduction in activation energy is not beneficial for an IBSC application because the carriers can be easily extracted from the QD by processes other than photon excitation.

Increases in lifetime within the QD states have a clear benefit for all photovoltaic applications. The longer a carrier remains within the QD state, the more likely it is that the carrier can be collected by either a photon, phonon or tunneling process. For the IBSC case it is essential that carriers exist in the QD states to provide carriers to be excited into the continuum.

6.2.3 Transient Absorption

Since TRPL measurements weren't able to measure the carrier lifetime inside the QD directly another technique called transient absorption (TA) was used. TA measurements were taken on a QD-*nipi* sample with one QD layer per intrinsic region, doping of 3x10^{18} /cm^3 and a period thickness of 50 nm. The TA measurement setup is depicted in Figure 6.14 where a single Ti-Sapphire laser is split and sent through two optical parametric amplifiers (OPA) to set the wavelength of the pump and probe pulses. The probe pulse is sent through a delay stage to allow the pulse to arrive at a specific time with relation to the pump. Both pulses are focused on the sample with the probe focused to a spot within the pump to ensure that the probe generates carriers in the entire region where the probe passes through the sample

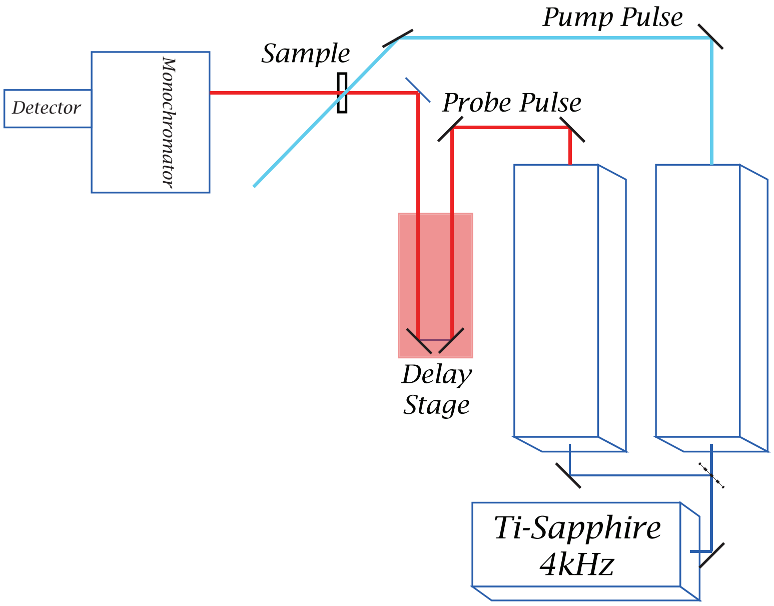

Figure 6.14: Depiction of the TA setup with a Ti-Sapphire laser emitted through two OPAs to set the wavelength of the pump and probe pulses, where the probe is measured through a monochromator

and is measured on a detector through a monochromator. The objective of this measurement is to have the pump generate carriers in the sample, modifying the absorption measured by the probe due to filling of carrier states.

TA measurements are shown in Figure 6.15, where $\Delta T/T$ is plotted versus delay time between the pump and probe pulses for measurements with a varying pump wavelength and set probe wavelength of 1300 nm. The probe wavelength of 1300 nm (0.95 eV) is a low enough energy that no carriers should be excited from the valence band to the conduction band by photons. The minimum energy required to excite carriers into the ground state of the QD is 1.1 eV. As a result there should be no absorption from the 1300 nm pulse unless carriers were populating the QD states and excited by the lower energy probe into the conduction band continuum. The pump wavelength was varied to excite carriers primarily into the wetting layer (930 & 985 nm), into the QD states (1005 & 1055 nm), or generate no excess carriers in the QD (1250 & 1290 nm). A negative $\Delta T/T$ signal indicates an increase in absorption (decrease in transmission) for the probe due to the carriers generated by the pump pulse, also referred to as photo-absorption. A photo-absorption for the probe wavelength of 1300 nm is indicative of a two-photon absorption process where the pump excites carriers into the QD states and the probe excites carriers from the QD into the conduction band continuum. The highest photo-absorption peak reaches nearly 20% which indicates that 20% of the 1055 nm light is absorbed if a carrier is in the QD that can be excited into the conduction band continuum.

Two things can be noted from the measurements. The first is that a half picosecond delay exists when the pump pulse is below 1055 nm, and the second is that the TA peak nearly disappears at pump wavelengths at or above 1250 nm. The delay is caused by the shorter wavelength pump exciting carriers primarily into the QW, which cannot be excited by a photon into the conduction band due to QW selection rules when the photon direction is normal to the surface [95]. The carriers in the wetting layer will energetically drop into the QD over the first half picosecond where they can be excited out of the QD states by a photon. This theory is further corroborated by the elimination of the delay time for the measurement with a probe wavelength of 1055 nm which should be absorbed only into the QD state. As the pump photon energy drops below the QD ground state of 1.1 eV (1127 nm) the pump can no longer excite carriers into the QD from which the probe can excite.

The very short lifetime of the photo-absorption on the range of 1 ps results from the low barrier for escape from the QD. With the QD ground state approximately 0.22 eV beneath the conduction band in an electric field with field strength of 5x10^7 V/m, the calculated time prior to thermal excitation from the confined level into the conduction band is 8.15 ps, which is within an order of magnitude of the photo-absorption lifetime seen. The lifetime was calculated with the use of theory presented elsewhere [96]. It is likely that the photo-absorption decay rate would decrease significantly with measurement at lower temperatures, giving rise to increased two-photon absorption and potentially a stronger photo-absorption. The short lifetime further demonstrates the impracticality of using InAs QD in GaAs

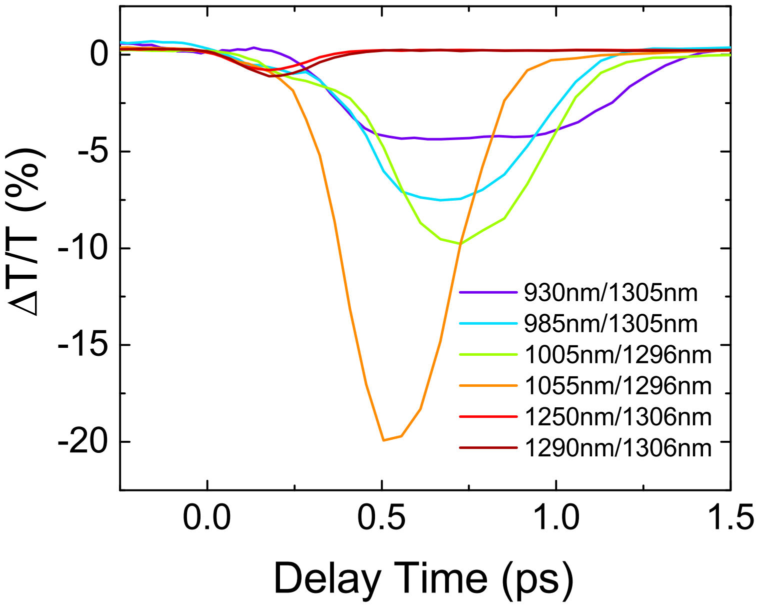

Figure 6.15: TA measurement of $\Delta T/T$ with a probe wavelength of 1300 nm and a variable pump wavelength

due to the short lifetime of the carriers in QD prior to thermal excitation into the continuum. Also this demonstrates that the *nipi* SL does not modify the lifetime of the carriers within the QD, but the longer lifetime measured by TRPL is due to the lifetime in the *nipi* SL instead.

6.3 CONCLUSIONS

In this chapter an evaluation of the effect of placing QD within a *nipi* SL was completed, focusing on optical characterization. An initial introduction to the growth of QD was followed by a discussion of the samples used for the experiments presented here.

Initial characterization of absorption was completed of both the *nipi* and QD-*nipi* SLs. The *nipi* test structures showed sub-bandgap absorption strength that was directly related to the electric field, with the maximum absorption reaching 30% for a 2.5 μm thick SL with 100 nm period and 3x10^{18} /cm^3 doping. Introducing QD to the stack resulted in an increase in absorption, slightly exceeding 50% for a 2.5 μm test structure. Absorption from QD in the QD-*nipi* device did extend further into the IR than the conventional QD due to the QCSE.

PL measurements also saw a red-shift due to the QCSE of approximately 40 meV, however a decrease in activation energy also related to the high field was seen, dropping from 113 meV to 30 meV for the QD-*nipi* test structure. TRPL measurements showed a considerable increase in lifetime for the QD-*nipi* test structure, increasing from 1.64 ns in the QD structure to 3.3 μs in the 2x QD-*nipi* case. This increase was however explained by the increase of lifetime in the *nipi* SL trapping carriers which relax through the QD states. Final analysis by TA was able to show that the lifetime within the QD did not exceed the lifetime expected to be measured in a QD, showing that the high field of a *nipi* SL has no direct effect on QD lifetime.

Chapter 7

Exploring the Radiation Tolerance of *nipi* Solar Cells

Historically and even today the space environment has been a driver for the advancement in solar cell technology. The space environment does; however, impose a number of challenges, of which radiation is a large concern. As was discussed in Section 2.1.1, the *nipi* solar cell has the potential of increased radiation tolerance due to the short diffusion length requirements. This theory will be tested by irradiating solar cells to determine the degradation in a *nipi* device as compared to a conventional space solar cell design.

The experimental work in this chapter will be evaluating the effect of radiation damage by 1 MeV electrons. As a comparison the expected 1 MeV electron doses were calculated for various orbits. In a geosynchronous equatorial orbit (GEO) orbit the equivalent electron dose after ten years would be 1.5x10^{19} /cm^2 without a coverglass, or 9.6x10^{13} /cm^2 with a 20 mil coverglass where a typical EOL for a conventional solar cell is on the order of 1x10^{15} /cm^2. For an orbit similar to the International Space Station with an orbit at 400 km and inclination of 51.65° the equivalent dose without coverglass is 5.6x10^{14} /cm^2 and 8.8x10^{11} /cm^2 with a 20 mil coverglass. The calculations were completed using Space Environment Information System (SPENVIS) which was created by the European Space Agency (ESA) to calculate doses at various orbits. The model was based on flux calculations that were developed elsewhere [97, 98].

7.1 SIMULATION OF *NIPI* RADIATION TOLERANCE

Given the objective of increasing EOL efficiency in the *nipi* device, a means of approximating the crystal damage resulting from large radiation doses is needed in order to properly optimize the design. When particles irradiate a device, multiple device parameters are adversely affected that end up degrading the device performance [99]. The parameters most affected are diffusion length, carrier concentrations in both *n*- and *p*-type regions, and front and rear-surface recombination velocities. The diffusion length (L) and *p*-type carrier concentrations (p) are the predominant factors that describe the effects of the radiation damage in the device. Relationships between device metrics and radiation flux have been discussed in Section 2.1.1, with the relationship to diffusion length shown in (2.7) and doping concentration in (2.8). The diffusion length relation depends on a damage coefficient K_L, and carrier removal is related to the carrier removal rate R_c.

The simulation environment that was used for this evaluation is Synopsys *Sentaurus*. The electrical coefficients used by *Sentaurus* do not use the bulk diffusion length to describe the transport characteristics, but uses the radiative recombination rate, SRH lifetime, and surface recombination velocity. Equation (2.7) is then quite easily manipulated to provide a relationship to determine the radiative recombination rate (R), SRH lifetime (τ) and surface recombination velocity (ν) shown in (7.1) through (7.3), where N_t is the number of traps, σ is the capture cross-section, and μ is bulk mobility.

$$R_\phi = R_o + \frac{K_L \phi D}{N_A} \tag{7.1}$$

Table 7.1: Layer structure for the *nipi* solar cell simulation developed for radiation tolerance. The orientation is such that the *n-type* dopant is the top layer of the first junction, alternating doping with the *p-type* dopant as the final layer of the sixth junction.

JunctionNumber	Total Thickness (nm)	Percentage intrinsically doped (%)	*p*-type Concentration (/cm^3)	*n*-typeConcentration(/cm^3)
1	20	0	7x10^{17}	1x10^{19}
2	60	30	1x10^{19}	1x10^{19}
3	100	30	1x10^{19}	1x10^{19}
4	180	35	7x10^{18}	1x10^{19}
5	360	50	7x10^{18}	7x10^{18}
6	620	50	7x10^{18}	7x10^{18}

$$\frac{1}{\tau_\phi} = \frac{1}{\tau_o} + K_L \phi D \tag{7.2}$$

$$\nu_\phi = \nu_o + \frac{K_L \phi}{\sigma N_t} \frac{kT}{q} \mu \tag{7.3}$$

The carrier removal rate and damage coefficients were taken from literature. The rates were taken for proton energy of 3 MeV, which is chosen since this energy causes uniform damage in a 3 μm thick device. For this energy the R_c coefficient for GaAs is 4.2x10^3, and the K_L term is 1.3x10^{-6} [99].

A device structure was designed using *Sentaurus* to better balance the current generated in each *nipi* junction, and the layer structure is described in Table 7.1. The optimization for the design attempted to voltage-match each of the junctions to ensure there was no voltage loss when connecting the junctions in parallel.

Simulations were completed as a function of radiation dose as shown in Figure 7.1(a) for both the *nipi* design and a control device. The control device is an *n-p* solar cell with a 2x10^{18} /cm^3 doped 100 nm thick emitter, and a base with 1x10^{17} /cm^3 doping that is 2.5 μm thick. The simulations assume reflection losses, and no ARC is used. The benefit of the *nipi* design is clearly seen if an EOL efficiency of 6% is chosen. The *nipi* device will have an expected lifetime 5.8 times greater than for the control

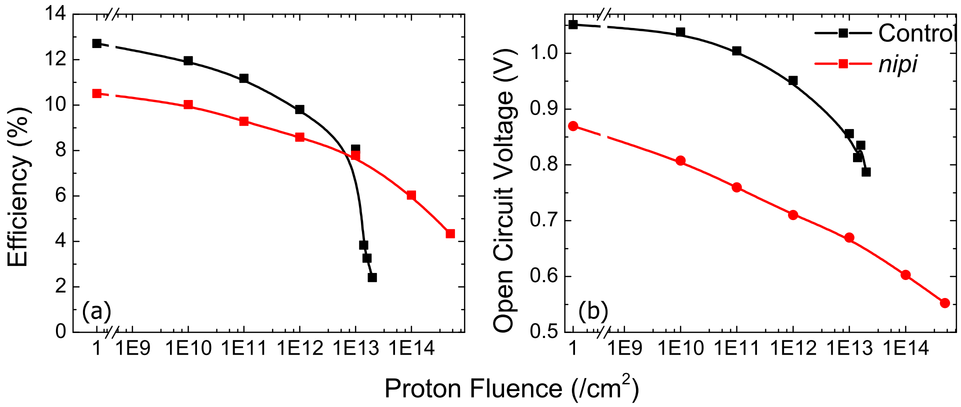

Figure 7.1: Efficiency (a) V_{OC} and (b) from both the *nipi* and control solar cells. The end of life for a *nipi* design is significantly greater than for the *n-p* diode.

device. As the required EOL efficiency is decreased, the advantage of the *nipi* design grows over the control device, and for a target efficiency of 5% the lifetime factor increases to 11.9. The cause of shorter lifetime in the control device is due to recombination in the base resulting in a loss in carrier collection. As discussed in the theory, the *nipi* structure is not affected by the reduced diffusion length, and carrier collection at higher doses remains very efficient.

The results shown in Figure 7.1 show the trade-offs of the *nipi* design, which has a higher fluence EOL, but the V_{OC} degrades more rapidly as shown in Figure 7.1(b), which results in a more gradual decrease for the *nipi* device efficiency. Given the excess dark current generation expected in the *nipi* structure due to the multiple junctions, the operating voltages decrease more rapidly than the control device with one junction. The high doping levels in the device result in increased SRH recombination, which has a carrier density dependence proportional to $np - n_i^2$ resulting in higher dark current and lower V_{OC} as dose increases. The J_{SC} for the *nipi* device does not; however, decrease appreciably until a dose of 1x10^{14}/cm^2, where only a 13.7% decrease is seen. At the same dose, the base of the control device has been type-converted, and therefore is generating no current. The maintenance of current generation in the *nipi* device is due to the close spacing of the multiple junctions, which collect current prior to minority carrier recombination. It is also clear that the *nipi* device BOL has a slightly lower

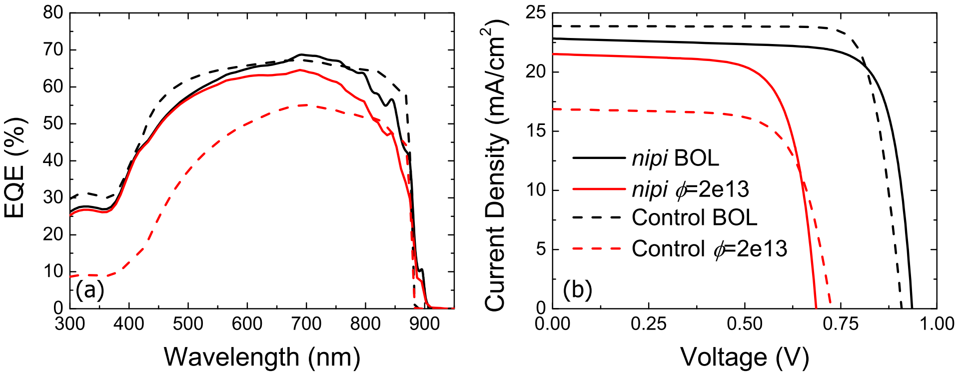

Figure 7.2: External quantum efficiency (a) and *J-V* (b) for *nipi* and np devices at both BOL, and EOL for each design

efficiency than the control, but it is shown that for any fluence past 1x10^{13} /cm^2 the *nipi* device generates higher efficiency. These results show that for certain applications, where lower efficiency is tolerable but longer lifetime is required, the *nipi* device is superior in design to a traditional solar cell.

EQE was also simulated and is shown in Figure 7.2(a) for both designs at BOL and a dose of 2x10^{13} /cm^2, further indicating the benefit of the *nipi* design in maintaining photocurrent generation following large radiation doses. Very little loss in the blue region of the spectrum was realized in the *nipi* design given the thin junction at the top of the device, which ensures that all generated carriers are well within a diffusion length of the electric field in all circumstances. The *nipi* device degrades slightly at longer wavelengths due to the wider junctions at the bottom of the device. The single-junction solar cell sees loss throughout the entire spectrum due to the two effects of the junction moving deeper into the base from type conversion and increased recombination.

The current-voltage plots shown in Figure 7.2(b) show that the *nipi* device is very efficient at maintaining current collection through the lifetime of the device. The degradation is seen in the operating voltage as previously discussed, which is opposite the trend for the traditional single-junction solar cell. It can also be noted that the BOL quantum efficiency for long wavelength light is slightly less in the *nipi* design. This loss comes about from the consideration that the active region thickness is only 1.34 μm as opposed to the 2.6 μm for the *n-p* device. To alleviate the long wavelength loss, it would be possible to use a Bragg reflector below the back surface field of the *nipi* device to reflect the long wavelength light into the upper junctions. It is necessary to use a technique such as a Bragg reflector instead of adding junctions, since increasing the amount of junctions will result in efficiency losses due to the considerations discussed previously.

The simulation work presented in this section was completed early on in the process of writing this thesis, and was done using protons as the irradiation source since a we had not determined what radiation particles would be used at that point. The experimental work that follows was completed with electron radiation, with corresponding simulations using damage estimates from electrons.

7.2 EXPERIMENTAL RADIATION TESTING

A GaAs single-junction *pin* device was fabricated as a baseline for comparison. The *n-type* base is 2 μm thick and doped at 1.6x10^{17} /cm^3, the intrinsic layer is 100 nm thick, while the emitter is 500 nm thick at a doping of 1.2x10^{18} /cm^3. $InGaP_2$ front and back surface fields are grown on either side of the device, each of which is 50 nm thick. Standard processing techniques were used to fabricate these devices into 1 cm^2 solar cells with no ARC. The *nipi* device used for this study was fabricated with the epitaxial regrowth process described in Section 4.1 with back-side contacts.

Radiation experiments were completed by utilizing an electron beam line with 1 MeV electron energies. Electrons at these energies fully penetrate the entire active region, creating equivalent damage throughout the solar cell. Three doses were selected to irradiate the *nipi* devices at 4x10^{14}, 1x10^{15}, and 2x10^{15} electrons/cm^2, which are near EOL for a typical space mission. The radiation was completed at NeoBeam in Middlefield Ohio with transmission measurements of radiation darkening tape used as a calibration. Different devices were used for each radiation fluence, so the remaining factors will be compared instead of absolute values for V_{OC}, J_{SC}, FF and efficiency. For each device one sun AM0 I-V, measurements were taken on the baseline and *nipi* devices. One sun AM0 I-V testing was completed on a class AAA dual source solar simulator, with the I-V taken on a Keithley 2400 source measuring unit.

For comparison, simulations of both the *nipi* and single junction devices were completed using the simulation package *Sentaurus* by Synopsys following the methods described in Section 3.2 and 7.1. Devices were also simulated under the radiation flux used for the experimental measurements by modifying the minority carrier lifetime, and dopant concentration as described in Section 2.1.1.

7.3 RADIATION RESULTS & DISCUSSION

One sun AM0 measurements were taken before and after irradiating *nipi* devices with 50, 100, 200 and 500 μm grid finger spacings along with a conventional single junction design for comparison. The results can be seen in Figure 7.3 where remaining factor is plotted for each device metric. The driving factor for efficiency loss in a conventional solar cell is from loss in J_{SC} due to a reduced base minority carrier diffusion length. The *nipi* structure tested has 50 nm doped layers which require a maximum minority carrier diffusion length of 20 nm prior to the carrier being collected in the drift field, minimizing the possibility of J_{SC} loss due to recombination prior to collection. This explains the near 100% remaining factor for J_{SC} for the doping SL devices.

Experimental results in Figure 7.3 demonstrate near 100% remaining factor of V_{OC} for the *nipi* devices; however simulations demonstrate that *nipi* solar cells are not anticipated to maintain V_{OC} more effectively than a single junction design. Simulations of *nipi* devices versus fluence show that V_{OC} does not degrade significantly for devices with 1.3x10^{13} /cm^2 interface traps up to a fluence of 1x10^{15} e$^-$/cm^2 while there is over 20% reduction in V_{OC} in the ideal simulation at the same dose. Although the device with interface traps has a high remaining factor, when comparing absolute V_{OC} the simulation with interface traps is lower than the ideal simulation through the entire fluence range. At BOL the ideal device has a V_{OC} of 1.036 V as compared to 0.859 V for the device with traps; after a simulated electron

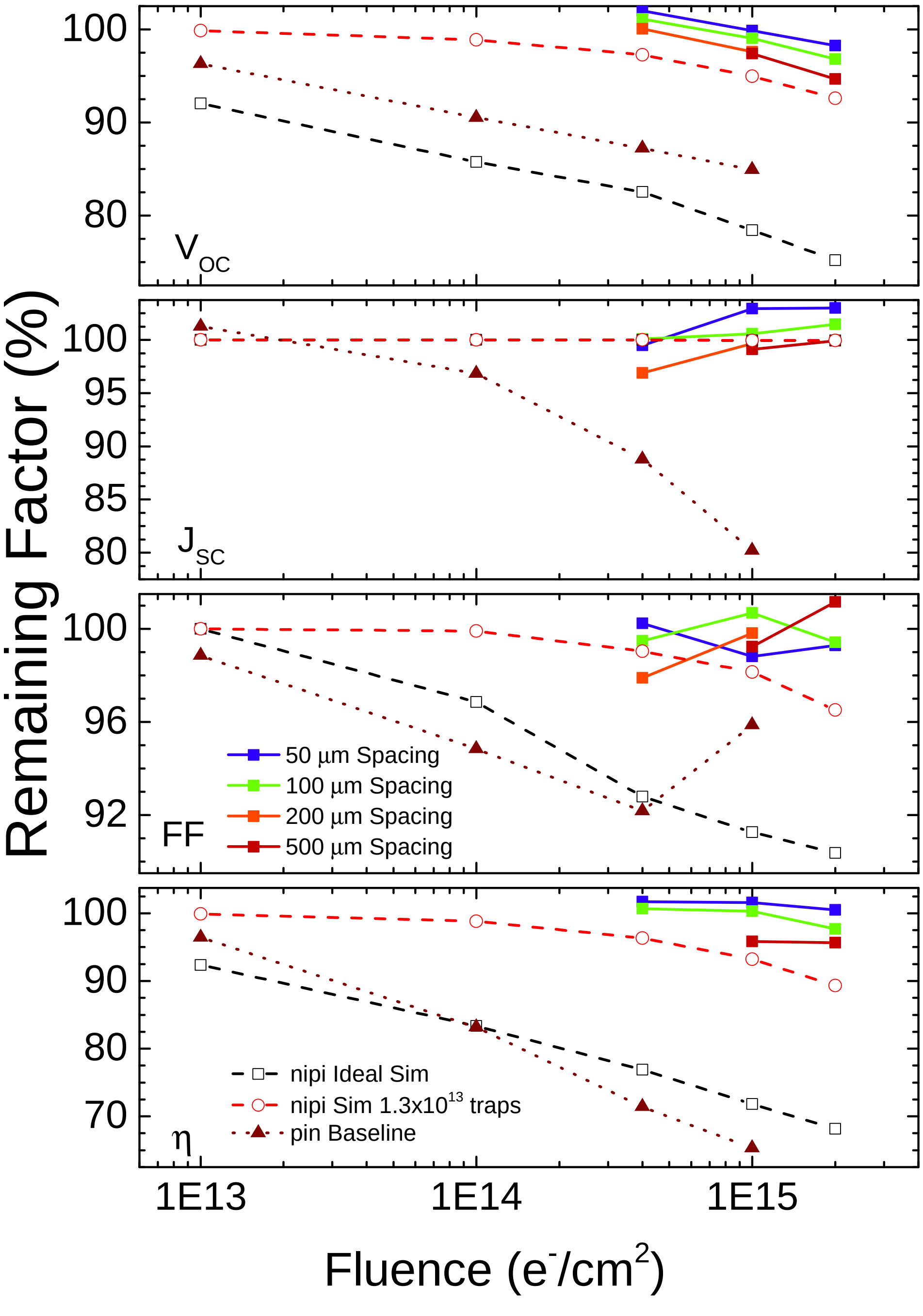

Figure 7.3: Plot of the remaining factor for V_{OC}, J_{SC}, fill factor and efficiency for four *nipi* devices compared to simulations of the device with and without traps at the regrown interface versus electron fluence and displacement damage dose. For comparison a single junction *pin* was plotted along the *nipi* devices.

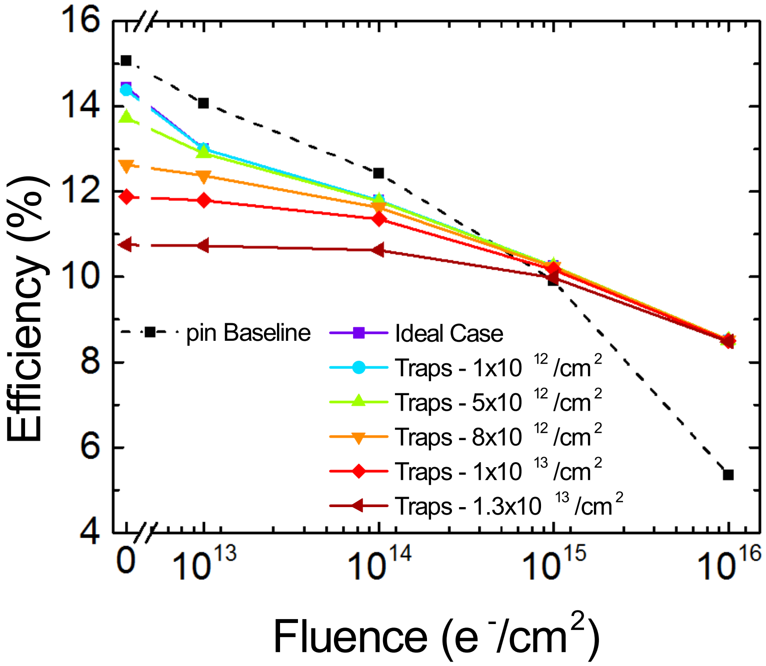

Figure 7.4: Efficiency plotted for *nipi* devices simulated with interface trap densities from 1x10^{12} to 1.3x10^{13} e$^-$/cm^2 versus fluence. A *nipi* device with an ideal interface and a conventional single junction GaAs *pin* design is simulated for comparison.

dose of 2x10^{15} e$^-$/cm^2 the V_{OC} drops to 0.757 and 0.745 V, respectively.

In order to understand the effect of interface traps on the solar cell interface trap densities were chosen between 1x10^{12} and 1.3x10^{13} e$^-$/cm^2 simulated versus radiation as described in Section 3.2.1. Efficiency is plotted for each trap density including the ideal case in Figure 7.4, which are compared to a conventional *pin* design. By comparing absolute efficiency a cross-over point can be measured where the *nipi* device will have a higher overall efficiency than the conventional design, and demonstrate increased utility although having a lower BOL efficiency.

For the ideal simulation the cross-over point where the *nipi* device has higher efficiency is at a fluence of 8.37x10^{14} e$^-$/cm^2 which is at a remaining factor for efficiency of 68.8% for the *pin* device. The cross-over point does not change for a trap density of 1x10^{12} /cm^2, and is only reduced to a fluence of 9.78x10^{14} e$^-$/cm^2 for a trap density of 1.3x10^{13} /cm^2. Minor changes are seen in the cross-over point versus trap density because of the manner in which V_{OC} degrades versus fluence. Voltage degrades more rapidly at lower fluences for a *nipi* device than a conventional *pin* design due to the multiple junctions in the design. The device simulated in Figure 7.4 has 25 diodes, each of which generates more leakage current at the junction as the Shockley-Reed-Hall recombination rate is increased. The efficiency benefit in the *nipi* device for higher radiation doses is due to the near complete maintenance of current, although the V_{OC} continues to steadily degrade. The efficient maintenance of current does demonstrate a significant improvement in efficiency at fluences greater than 1x10^{15} e^{-}/cm^{2} regardless of trap density.

7.4 CONCLUSIONS

This chapter evaluates the use of *nipi* solar cells in high radiation environments, which can exploit the drift dependent carrier collection of the design. Initial simulations using proton fluence pointed to the increase in total energy available form the *nipi* solar cell over the life of the device. The simulations also showed the expected efficient maintenance of current at high doses, which was confirmed experimentally as well.

Experimental results showed an improved V_{OC} and FF maintenance near 100% remaining factor as a function of dose, which was not expected from simulation. Simulations with a trap density of 1.3x10^{13} e^{-}/cm^{2} at the regrowth interface were able to show the efficient maintenance of V_{OC} and FF was due to the initial degraded performance of the device. Simulations also showed that with a reduction in the initial interface trap density the performance relative to a *pin* solar cell is comparable. Regardless of the interface traps, no loss in current was measured to a dose of 2x10^{15} e^{-}/cm^{2}.

Chapter 8

Conclusions and Future Work

8.1 Research Summary

This thesis explored the possibility of using a *nipi* doping SL device in photovoltaic applications. Prior to the beginning of this work a significant amount of theoretical work had gone into understanding the physics of *nipi* SLs; however, very little work had been completed towards the development of photovoltaic devices with *nipi* SLs. The work contained here continued the theoretical development, and evaluated multiple methods for fabricating *nipi* solar cells. This provides a path forwards towards the development of high efficiency solar cells that are tolerant to materials with reduced minority carrier lifetimes.

Work related to the theoretical understanding of *nipi* solar cells was the development of the modified dual diode model described in Section 3.3. The model adapted the conventional dual diode model that describes a single junction solar cell to allow n diodes to be placed in parallel in a *nipi* parallel connected diode configuration. Additionally the regrown contact could be modeled in parallel to the *nipi* diodes to account for injection from the carrier-selective contacts. The diode model was paired with calculations for minority carrier lifetimes and dark saturation currents, which were modified by photo-generated carrier concentrations. The coupling of these calculations with the diode model provided a greater understanding of trap state filling for devices measured under increased concentrations. As solar concentration was increased trap states were filled and no longer active, allowing the dark saturation current and V_{OC} of the solar cell to improve.

The modeling that was completed allowed a more detailed understanding of defects and traps at the epitaxial regrowth interface. The model was used to characterize experimental measurements of *nipi* solar cells under concentration in Section 5.1.4. Improvements in V_{OC} were seen under concentration that were greater than expected by the logarithmic increase in V_{OC} expected by theory. The results were explained by the model with a trap density of 4x10^{14} /cm^3 at mid-gap which were filled to allow V_{OC} to fully recover at a concentration of 7 suns. Sensitivity modeling was also completed to demonstrate that a trap density of 5x10^{13} /cm^3 is required in order to ensure that all the trap states were filled at a concentration of one sun, effectively demonstrating an ideal solar cell.

In addition to the modeling work, simulation work with Synopsys *Sentaurus* was also completed to gain a complementary understanding of the devices. The two-dimensional simulation software was used to gain an understanding of expected results of an ideal *nipi* solar cell in Section 3.2, and devices with traps at the epitaxial regrowth interface in Section 3.2.1. Ideal simulations showed a achievable efficiency of 14.4% without an ARC, and simulations with traps allowed a close match to experimental for V_{OC}. Further simulation work was also completed to provide a detailed understanding of the operation of *nipi* solar cells in a radiation environment in Section 7.1 and 8.2.2. Simulations with 1 MeV electrons showed that *nipi* solar cells could have BOL efficiencies close to conventional *pin* designs and a better absolute efficiency at doses higher than 1x10^{14} e$^-$/cm^2 assuming the correct design was used.

The majority of the work completed was focused on the fabrication and testing of *nipi* solar cells, demonstrating a significant improvement in the understanding of how to fabricate a device that requires carrier-selective lateral contacts. Initial characterization of the fabrication method for forming the carrier-selective contacts with both epitaxial regrowth and spin-on dopant diffusion processes was completed in Chapter 4.

Numerous solar cells have been fabricated with the processes developed, which provided a significant amount of information about the fabrication processes required to improve device results. Initial steps were able to determine that using a back-side contact a parasitic shunt path could be eliminated between the anode and cathode. This change resulted in a significant efficiency increase from 6.1% to 9.0% which corresponded to an increase in V_{OC} and FF. Further improvements were made by fine tuning the fabrication process to reach an efficiency of 9.14% prior to AR coating and 12.5% following AR coating.

Evaluation of alternate fabrication routines was also completed by changing the epitaxial regrowth process from a homoepitaxy growth of GaAs on GaAs to heteroexpitaxy using either InGaP or AlGaAs as the regrowth material. The use of InGaP as a regrowth material did show some promise with an increase in V_{OC} from 0.58 V for GaAs to 0.659 V for InGaP.

A final alternate process was developed to use a diffused junction approach. Although the device results fabricated with this process were degraded when compared to the epitaxial regrowth process, it was a demonstration of the viability of fabricating *nipi* devices through various means. With additional process development it is believed that a diffused junction process could yield results similar to the epitaxial regrowth process.

Given the objective of an IBSC device, work evaluating a QD-*nipi* SL was completed in Chapter 6. Multiple *nipi* and QD-*nipi* test structures were grown and evaluated spectroscopically. The relationship between absorption of a *nipi* SL was compared to theory where the electric field strength was directly proportional to the sub-band absorption. Absorption from QD-*nipi* test structures showed that putting

QD within the *nipi* layers resulted in a red shift for absorption from the QD states due to the quantum confined Stark effect. This resulted in an increase in absorption for the QD-*nipi* structure between 920 and 1050 nm when compared to the QD only structure. Photoluminescence analysis was able to show the same peak shift in the QD states, and TDPL showed a decrease in the activation energy for the QD-*nipi* structure to 30 meV from 113 meV for the QD structure. Time-resolved photoluminescence showed an increase in the lifetime measured from the QD-*nipi* test structure by three orders of magnitude; however, this was theorized to be due to the non-equilibrium carrier population in the *nipi* layers recombining through the QD states. This was confirmed through TRPL measurements of the conventional *nipi* structures as 900 nm which showed a similar lifetime as the QD-*nipi* device, indicating the enhanced lifetime was due to the incresed lifetime expected in the *nipi* SL. Further confirmation came from transient absorption analysis which showed the lifetime of the excited states in the QD states when resonantly pumped is on the order of half a picosecond.

Finally, analysis of the radiation tolerance of *nipi* solar cells was completed. Some initial simulations pointed to the enhanced radiation tolerance possible with the *nipi* device having a higher overall efficiency than the *pin* solar cell at 1 MeV electron radiation doses greater than $1x10^{13}$ /cm^2. Experimental results were able to show that *nipi* solar cells had a remaining factor for efficiency that remained at 100% for a dose up to $2x10^{15}$ e$^-$/cm^2, which was much higher than expected, as compared to the *pin* control device that had a remaining factor of 68.8% at a dose of $1x10^{15}$ e$^-$/cm^2. The result was explained by simulations that showed trap states at the regrowth interface dominate the dark current and V_{OC} if the trap density is higher than the defect density created by electron radiation. Simulations also showed the possibility for improving the BOL efficiency for *nipi* solar cells by reducing the trap density; however, this had a minimal effect on EOL efficiency.

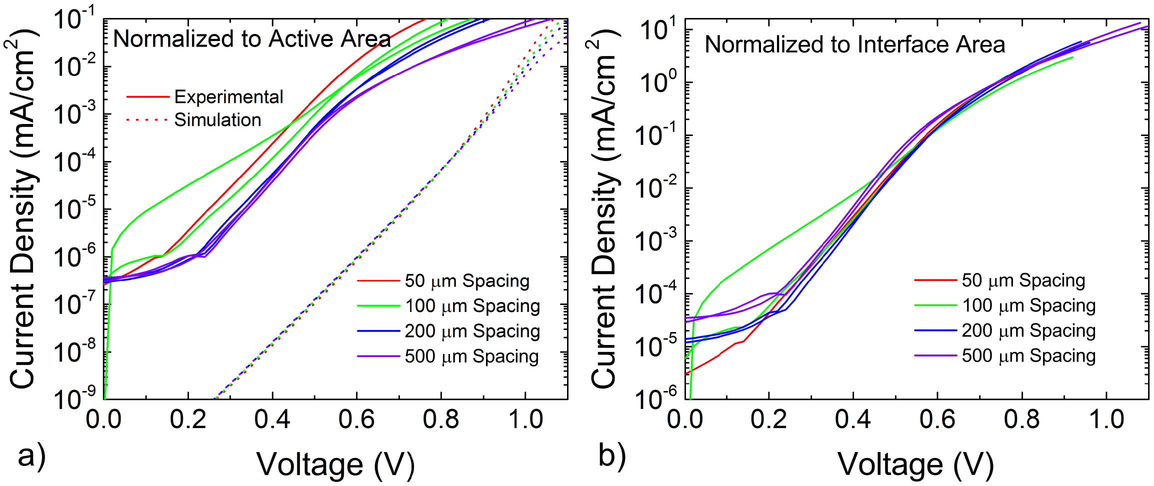

Figure 8.1: Dark current measurements of multiple *nipi* devices fabricated with grid finger spacings between 50 and 500 μm, plotted (a) normalized to active area and (b) normalized to regrowth interface area.

8.2 SUMMARY OF FUTURE WORK

The future work included involves two sections with multiple simulations and calculations that evaluate the possibility of making modifications to design or process. This is followed by a brief discussion about the prospect of each of these changes, with the details in the specific sections within the body of the document.

8.2.1 Alternative Designs for Reduced Trap Sensitivity

The device fabrication efforts completed to date have been focused on improving the device results by modifying the epitaxial regrowth preparation or growth process; however, alternate routes are available to improve the device results. Analysis of dark current from a set of *nipi* devices fabricated simultaneously with four mask-defined grid finger spacings of 50, 100, 200 and 500 μm indicates that dark current is a function of regrowth interface area, not total active area.

Dark current measured for devices with different grid finger spacing and current density is plotted in Figure 8.1 (a). It is apparent that the dark current density varies as a function of grid finger spacing, with

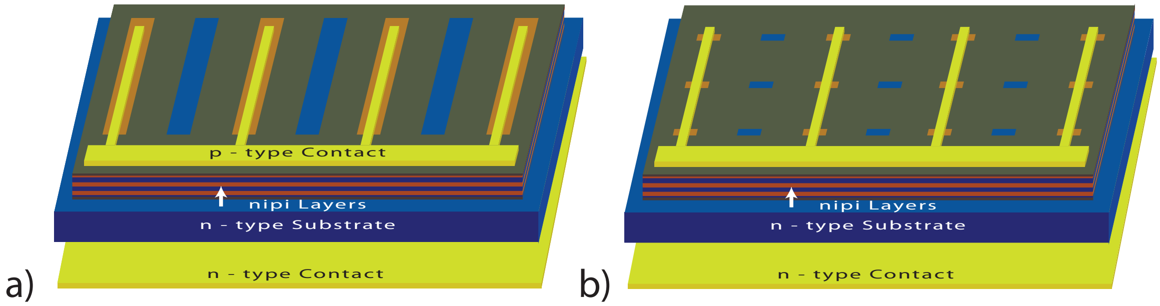

Figure 8.2: Depictions of the *nipi* design fabricated with (a) the conventional mask set that uses etched grooves extending the length of the device and (b) an alternate mask set that uses polka-dot etch holes for the epitaxial regrowth.

the highest dark current corresponding to the smallest grid finger spacing. Simulated dark current is also plotted as the dashed lines, which is more than four orders of magnitude lower than the experimental dark current. It is assumed that the simulated dark current should match the dark current from the *nipi* SL, and the experimental dark current is dominated by the trap states at the epitaxial regrowth interface which was not accounted for in the simulation. The assumption that the dark current is dominated by regrowth interface was corroborated when dark current was plotted normalized to the regrowth interface area instead of the total active area, shown in Figure 8.1 (b). When dark current is analyzed as a function of regrowth interface area the dark currents are very closely matched.

Given the correlation between regrowth interface area and total dark current for the device, it provides an opportunity for reducing dark current by reducing the regrowth interface area. The mask design that has been used for the *nipi* development to date is depicted in Figure 8.2 (a) with etched v-grooves that run the length of the solar cell. If instead of grooves that run the length of the solar cell we use a polka-dot design shown in Figure 8.2 (b) where contact holes are etched into the *nipi* SL the regrowth interface area could be significantly reduced. For this design the cathode would be on the back side with an ohmic contact to the *n-type* regrowth, and the anode would be on the top side with the metalization contacting along the top of each *p-type* regrowth in a row.

Approximations of the effect of modifying the mask design with a polka-dot structure are shown in

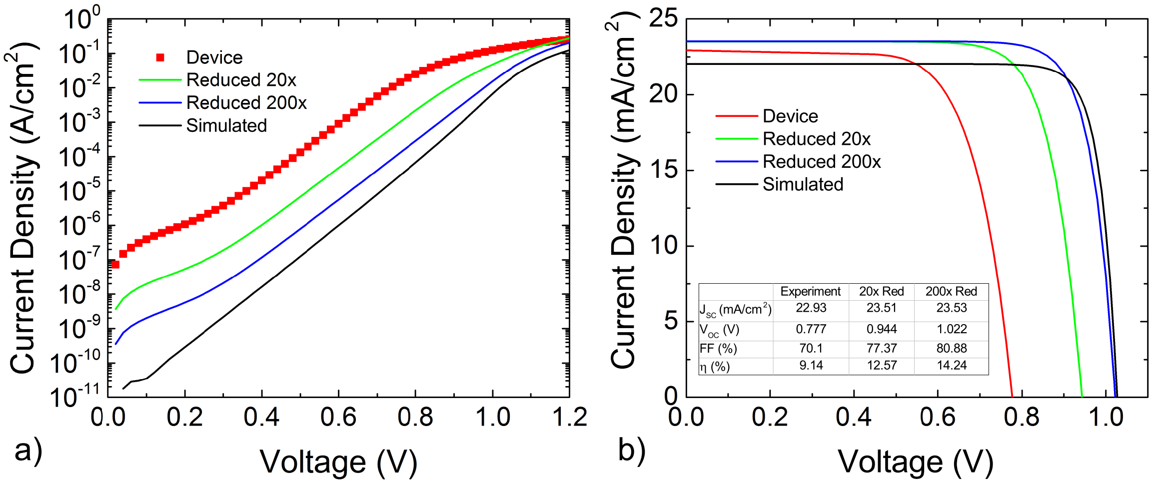

	Experiment	20x Red	200x Red
J_{SC} (mA/cm^2)	22.93	23.51	23.53
V_{OC} (V)	0.777	0.944	1.022
FF (%)	70.1	77.37	80.88
η (%)	9.14	12.57	14.24

Figure 8.3: Projections of (a) dark current and (b) one-sun AM0 I-V curves for the polka-dot design with a 20 and 200x reduction in regrowth interface area compared to experimental and simulated results.

Figure 8.3. Dark current was projected by reducing the measured dark current by a factor of 20 and 200 times, then adding it to the simulated dark current which was assumed to be the minimum dark current contributed by the *nipi* SL. Calculated dark current is shown in Figure 8.3 (a), with the dark current trending towards the simulated curve. One-sun AM0 I-V curves in Figure 8.3 (b) were calculated from the dark current projections by subtracting the dark current from J_{SC}. Due to the expected reduction in shadowing the J_{SC} was modified and increased from 22.93 mA/cm^2 for the experimental measurement to 23.53 mA/cm^2 for the projection with 200x reduction in interface area. This corresponds to a reduction in shadowing from 10.5% to 4.9% with the polka-dot design. The reduction in dark current improves V_{OC} from 0.777 V for the experimental measurement up to 1.022 V for the 200x reduced interface area which approaches the simulated V_{OC}. Efficiency without an ARC is projected to reach 14.24%, and would be expected to exceed 20% with an AR coating.

Changing the mask set to reduce regrowth interface area is not something that could be done with a trivial change, but would require a concerted development effort. As was discussed in Section 4.1, changing the selective regrowth area will change the growth rate enhancement, and the required growth time to achieve a desired material thickness. Growth rate enhancement would be expected to increase

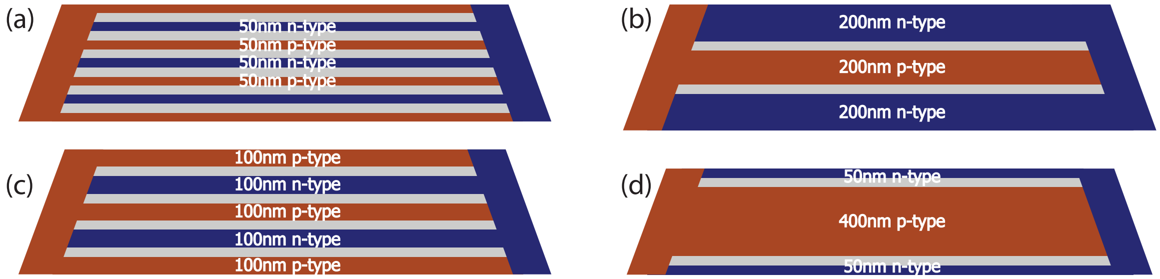

Figure 8.4: Depictions of the *nipi* SL designs for radiation hardness with (a) 50 nm, (b) 100 nm, (c) 200 nm and (d) matched resistivity doped layers.

significantly if the regrowth area were reduced by a factor of 200, and would have to be accounted for. Further, the contact spacing would have to be carefully evaluated to ensure that increased series resistance effects would not be introduced. For the present design current needs only travel to in one dimension to the contact, and in the proposed alternate design current would have to travel in both x and y dimensions, possibly increasing path length and resistance by a factor of $\sqrt{2}$.

8.2.2 Alternative Designs for Increased Radiation Tolerance

In order to improve the radiation tolerance of a *nipi* design, an evaluation of the SL design must be taken into consideration. It is apparent that having a total of 25 parallel diodes in a design results in a steady decline in V_{OC} and a cross-over efficiency versus a *pin* design at a relatively high fluence. Multiple alternative designs with fewer parallel diodes have also been evaluated under simulation to characterize the effect of device design on radiation tolerance.

Three designs have been proposed along with the design discussed in Section 7.2 where the doped layer thickness was 50 nm. For the alternate designs the doped layer thicknesses were increased to 100 and 200 nm, along with a design that worked to match the resistivity in the *n-* and *p-type* regions with the respective thicknesses being 50 and 400 nm. Each of the designs is depicted in Figure 8.4. By increasing the thickness of the doped layers and keeping the entire active region thickness close to 2.5 μm, the number of parallel connected diodes is reduced. The baseline structure with 50 nm layers has 25 diodes in parallel, which is reduced to 17 for 100 nm layers and 9 for both the 200 nm doped layers and the matched resistivity design. As a result of the reduction in number of diodes from 25 to 9 the dark current should be reduced by nearly a factor of three, resulting in an improvement in V_{OC}.

Each of the designs were simulated at electron fluences from 1x10^{13} to 1x10^{16} e^{-}/cm^{2} and compared to the baseline 50 nm layer *nipi* design as well as a conventional *pin* design. The AM0 one-sun simulation metrics of J_{SC}, V_{OC}, FF and efficiency are plotted in Figure 8.5.

Trends with respect to current follow the expected trend where the devices with the thickest layers have the largest drop in J_{SC} while the devices with thinner layers have little to no reduction in J_{SC} with respect to fluence. The *pin* device has a 2 μm base and a 500 nm emitter regions over which minority carriers must diffuse. The reduction in carrier diffusion length results in the loss of J_{SC} from a BOL value of 22.89 to 12.81 mA/cm^{2} at end of life (EOL). Although the material parameters are the same for the *nipi* devices, the longest distance a carrier is required to diffuse would be 400 nm in the matched resistivity device which only resulted in a drop of 4.64 mA/cm^{2} over a dose of 1x10^{16} e^{-}/cm^{2}. The effect of increasing the thickness of the doped layers is evident as the device with 50 nm doped layers has a reduction in J_{SC} of only 0.04 mA/cm^{2} at EOL.

Beginning of life V_{OC} values are approximately the same for each of the different devices, with the voltage increasing slightly as the number of parallel diodes is decreased. The 50 nm layer has a BOL V_{OC} of 1.036 V increasing to 1.041 V for the device with 100 nm layers, followed by the device with matched resistivity at 1.042 V and finally the 200 nm layer device with a V_{OC} of 1.048 V which is only slightly below the 1.057 V value for the *pin* design. As the radiation dose is increased the difference between each device is increased as can be seen in Figure 8.5, while the *pin* design always has a higher V_{OC}. The rate of decay in V_{OC} is directly related to the number of parallel diodes in the device, which is evident from the 200 nm layer and matched resistivity devices having identical decay rates versus fluence, both of which have 9 parallel diodes.

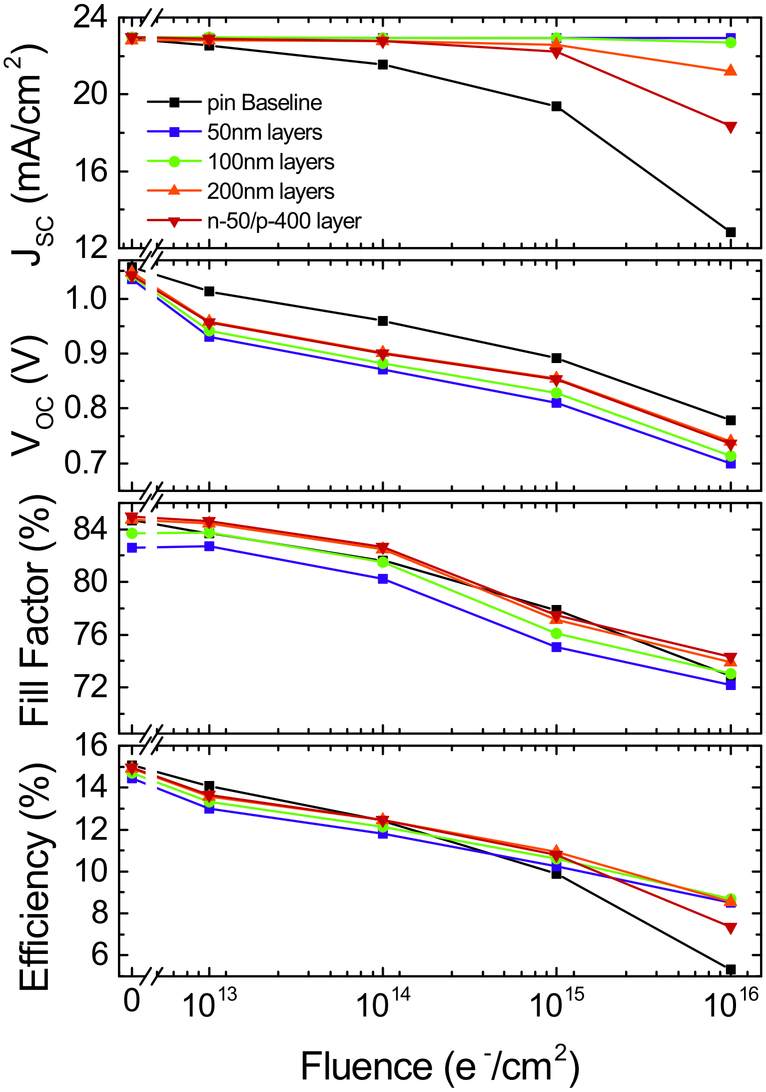

Figure 8.5: Plots of J_{SC}, V_{OC}, fill factor and efficiency for four *nipi* designs and a conventional *pin* design versus radiation fluence from 1x10^{13} to 1x10^{16} e$^-$/cm^2.

Fill factor for the *nipi* devices is largely driven by the thickness of the doped layers. There is a slight improvement in absolute FF versus design resulting in a slight 1.5% boost in FF for the matched resistivity design over the thin 50 nm design through dose. The remaining factor versus fluence is relatively constant for each design.

Due to the relationship between the number of parallel diodes in a device and the degradation rate in V_{OC} there is a motivation to reduce the number of parallel diodes. This motivation however does come with a trade-off in J_{SC} which will degrade more rapidly as the thickness of the doped layers is increased. Design decisions must be made regarding the objectives of the solar cell in order to determine the optimal *nipi* structure. If high current maintenance is required a design with thin 50 nm doped layers is ideal; however, if high efficiency at 1x10^{16} e^{-}/cm^2 fluence levels is required then a thicker 100 or 200 nm doped layer thickness is more ideal. A final objective would be the lowest dose at which the *nipi* device surpasses the *pin* design, which would be 1x10^{14} e^{-}/cm^2 for both the 200 nm layer and matched resistivity designs.

8.2.3 Additional Future Work

The TEM analysis that was completed in Section 5.1.5 indicated that the use of InGaP for a BSF layer may be resulting in dislocations forming on the InGaP surface, and possibly changing the InGaP into an InGaAsP or InGaAs composition resulting in strain. Moving to an AlGaAs BSF would eliminate the P to As transfer in the BSF material, likely eliminating the formation of dislocations at the regrowth interface.

In Section 5.1.6 preliminary experiments were completed to evaluate the use of alternate higher bandgap materials for the regrowth contact, using InGaP and AlGaAs. This would could be continued to further reduce the effect or influence of trap states at the interface. Analysis of the regrowth interface with the alternate materials is critical in order to characterize the current status, which would be done through TEM. The AlGaAs regrowth suffered from having a dopant concentration of approximately $3x10^{17}$ /cm^3 which likely lead to some of the problems with that device. Switching to the use of CCl_4 for a carbon *p-type* dopant and DETe for a tellurium *n-type* dopant would likely enable higher dopant concentrations. Given the improved dark current when using the InGaP regrowth there is significant motivation to continue down this path.

As stated in the abstract and introduction, the objective of this work was to develop the fabrication process for *nipi* solar cells, and a greater understanding of *nipi* SLs towards the objective of a QD-*nipi* based IBSC. A greater understanding of QD-*nipi* SLs has been developed in Chapter 6, which demonstrates some of the effects of putting QDs into *nipi* layers. With the improvements demonstrated in the fabrication of *nipi* solar cells it is now possible to grow QD-*nipi* devices and have a reasonable comparison between the baseline and QD solar cell (QDSC).

Next steps for the development of a QD-*nipi* based IBSC would include the growth and fabrication of QD-*nipi* solar cells. Upon fabrication, testing is required to characterize the possible formation of an IBSC. Pump-probe spectral response measurement techniques can be used to determine if any two-photon absorption occurs in the device, which is a primary requirement for the IBSC.

Further modification to the QD-*nipi* SL would also be necessary. The ability of placing QDs within one of the heavily doped regions of a *nipi* SL has yet to be studied, and could be evaluated by placing QDs in both the *n-* and *p-type* regions. There is increased interest for placing QDs in the *n-type* region because it places the QD states near to the Fermi level, which allows the QD state to be half filled.

Conventional solar cells have been grown with two, three and even more junctions in series with each other to reduce transmission and thermallization losses for many years. Upon initial inspection this could be difficult for a *nipi* solar cell; however, a route to a dual-junction device is possible. The use of a *nipi* SL in a dual-junction design could help mitigate the impact of radiation on the junction with the lowest radiation hardness, thereby hardening the multi-junction device.

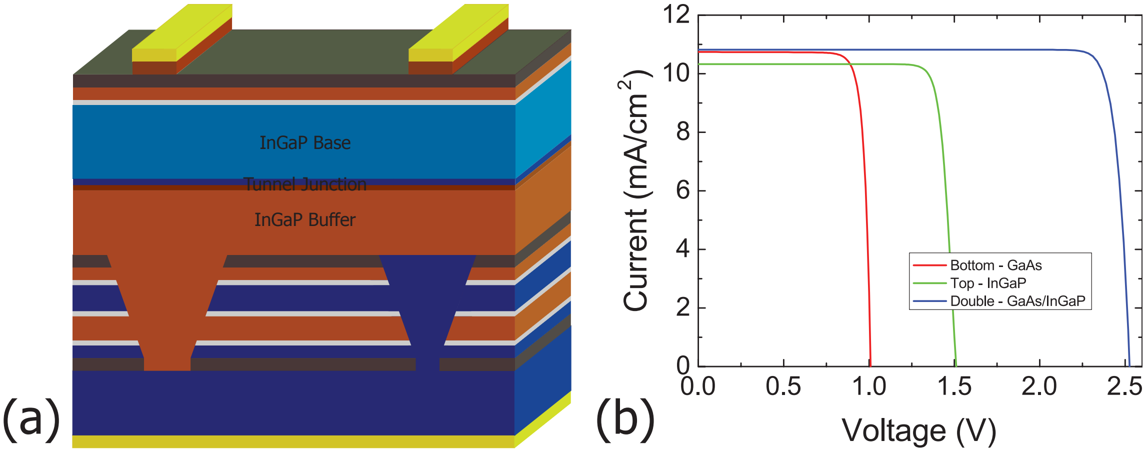

Figure 8.6: (a) Cross sectional schematic of a dual junction *nipi* solar cell with a GaAs *nipi* lower junction and a InGaP *pin* top junction, and (b) one sun AM0 I-V simulation of a the dual junction design along with each isotype

Initial simulation work has been completed with a *nipi* solar cell combined in a dual-junction orientation with a conventional *pin* junction. The design chosen was with a GaAs *nipi* junction beneath an InGaP *pin* junction as depicted in Figure 8.6(a). A 1 μm buffer layer was used between the two junctions which is assumed to be sufficient to allow planarization of the surface following etch and regrowth in v-grooves. For simulation the buffer layer was chosen to be InGaP which resulted in a current loss if current matching between the two junctions was achieved.

Simulations were completed with no ARC. AM0 illumination at one-sun and the results are shown in Figure 8.6(b). Some inconsistencies in the isotype simulations lead to a lower current in the InGaP junction than the GaAs *nipi* and dual-junction simulations, with the dual-junction current simulated at 10.82 mA/cm2. The voltage of each of the component cells was 1.009V and 1.511V for the GaAs and InGaP cells, respectively, resulting in a dual junction voltage of 2.526V. Fill factor for the dual junction design was 89.58% which resulted in an efficiency of 18% for the dual junction design. Efficiency can be improved by using a higher bandgap buffer layer to eliminate parasitic absorption, and by including an ARC.

The dual-junction device could be fabricated by initially growing and fabricating a *nipi* solar cell through the two regrowth steps. Following the second regrowth and removal of the selection oxide layer the wafer would be returned to the reactor. Initially a 1 μm planarizing InGaP layer would be grown to return to a smooth (100) surface, followed by the growth of a tunnel junction and the InGaP solar cell. If the wafer were *n-type* doped the buffer layer would be *p-type*, making an ohmic contact to the *p-type nipi* regrowth, and rectifying to the *n-type* regrowth. The InGaP cell would then be grown in a *pin* configuration to have both diodes connected in series.

Development would be required to ensure that the buffer layer would sufficiently planarize the wafer from the surface morphology created by the v-groove etch and regrowth. Ideally the buffer layer would be a higher bandgap material than InGaP to eliminate any parasitic absorption that would result in a current loss in the GaAs junction. It is assumed that the rectifying junction between the *n-type nipi* regrowth and the *p-type* planarizing layer would be sufficient to not shunt the *nipi* layer, but this would require analysis.

Glossary

J_{SC} short-circuit current density. 38, 40, 43, 48, 66, 69, 71, 76, 77, 81, 84, 86, 87, 89, 96–98, 129, 131, 132, 142, 144, 146

V_{OC} open-circuit voltage. 32, 34, 38, 40–43, 47, 48, 66, 69, 71, 74, 77, 81, 84, 86–89, 94, 97, 98, 100–103, 117, 129, 131, 132, 134, 135, 137–139, 142–144, 146, 150

W_{OC} bandgap-V_{OC} offset. 89–91

nipi *n-type*/intrinsic/*p-type*/intrinsic. 3–7, 9, 11–15, 17, 18, 21–25, 27, 31–35, 38–41, 43, 44, 46–48, 50–53, 55, 62, 65, 66, 68, 70–72, 81, 84, 86–91, 100, 102–107, 109–115, 118–120, 124–132, 134–144, 146–149, 152

AM0 air-mass zero. 2, 37–39, 41, 68, 81, 86, 95, 96, 131, 132, 142, 144, 148

AM1.5G air-mass 1.5 (global). 7, 9, 47, 68

ARC anti-reflection coating. 36, 39, 48, 57, 64, 86–88, 102, 103, 128, 131, 137, 142, 148

AsH_3 arsine. 13, 53, 92

BOE buffered hydrofluoric acid. 53, 56, 61, 64

BOL beginning-of-life. 22, 129, 130, 132, 134, 137, 139, 144

BSF back surface field. 92–94, 103, 146

CB conduction band. 9–11, 16, 23, 25, 27–29, 105, 110, 115

DEZn diethylzinc. 53, 55

E_g bandgap energy. 2, 7, 10, 89

EDS energy dispersive spectroscopy. 93

EHP electron-hole pair. 33

EMA effective-mass approximation. 26, 28, 34

EOL end-of-life. 22, 126–129, 131, 139, 144

EQE external quantum efficiency. 11, 35–40, 96, 97, 101, 130

ESA European Space Agency. 127

F-K Franz-Keldysh. 26, 27, 30, 34, 111

FF fill factor. 38, 40–43, 48, 66, 71, 74, 88, 100, 131, 135, 138, 144, 146

FIB focused ion beam. 91

GEO geosynchronous equatorial orbit. 126

GRC Glenn Research Center. 14, 70, 74, 102

GRE growth-rate enhancement. 55, 56, 58, 59, 61, 67, 95

HR-TEM high resolution TEM. 91, 93

I-V current-voltage. 35–39, 42, 68, 69, 77, 81, 89, 90, 95, 98, 100, 131, 132, 142

IB intermediate band. 9–11, 105

IBSC intermediate band solar cell. 4, 6, 7, 9–11, 104, 105, 113, 114, 116, 121, 138, 147

IQE internal quantum efficiency. 11

IR infrared. 113, 121, 124

MBE molecular beam epitaxy. 52, 53, 66

MO metal-organic. 13

MOVPE metal-organic vapor phase epitaxy. 13, 14, 53, 58, 59, 70, 79, 81

NASA National Aeronautics and Space Administration. 14, 74, 102

OPA optical parametric amplifiers. 121

OSU Ohio State University. 91

PCD parallel-connected diode. 44, 46, 47

PECVD plasma enhanced chemical vapor deposition. 88

PH_3 phosphine. 13

PL photoluminescence. 106, 108, 114–117, 125, 152, 153

QCSE quantum confined Stark effect. 105, 113, 114, 118, 125

QD quantum dot. 4, 7, 10–12, 15, 104–109, 111–125, 139, 147, 152

QD-*nipi* quantum dot *nipi*. 7, 11, 15, 107, 108, 112, 114, 116–121, 124, 125, 138, 139, 147

QDs quantum dots. 4, 11, 12, 107, 113, 116, 147

QDSC QD solar cell. 147

QW quantum well. 3, 4, 16, 104, 109, 123

RIT Rochester Institute of Technology. 102

S-K Stranski-Krastanov. 106, 107

SEM scanning electron microscope. 56, 59, 79, 82

Si_2H_6 disilane. 53, 55

SIMS secondary ion mass spectrometry. 64, 66

SL superlattice. 3–5, 11, 14–18, 20, 23–27, 29–31, 34, 39, 41, 42, 44, 50–53, 59, 65–67, 70, 84, 87, 100, 103, 105–114, 116, 118–120, 124, 125, 132, 136, 138, 139, 141–143, 147

SLs superlattices. 3, 6, 16, 17, 25, 124, 136, 147

SOG spin-on glass. 52, 62, 63, 66, 98, 100, 101, 103

SPENVIS Space Environment Information System. 127

SRH Shockley-Read-Hall. 37, 38, 105, 127, 129

STEM scanning transmission electron microscope. 91, 93

TA transient absorption. 121–123, 125

TDPL temperature-dependent PL. 115, 139

TEM transmission electron microscope. 86, 91, 94, 103, 146, 147, 151

TEOS tetraethylorthosilicate. 53

TMAl trimethylaluminum. 13

TMGa trimethylgallium. 13, 53

TMIn trimethylindium. 13

TRPL time-resolved PL. 108, 117, 120, 121, 124, 125, 139

UID unintentionally doped. 36, 66, 79

V-W Volmer-Weber. 107

VB valence band. 9, 16, 23, 25, 27–29, 105, 110, 117

References

[1] G. W. Crabtree and N. S. Lewis. Solar energy conversion. *Physics Today*, 60(3):37–42, 2007.

[2] Joan M Ogden, Margaret M Steinbugler, and Thomas G Kreutz. A comparison of hydrogen, methanol and gasoline as fuels for fuel cell vehicles: implications for vehicle design and infrastructure development. *Journal of Power Sources*, 79(2):143–168, 1999.

[3] William Shockley and Hans J. Queisser. Detailed balance limit of efficiency of p-n junction solar cells. *Journal of Applied Physics*, 32(3):510–519, 1961.

[4] B.M. Kayes, Hui Nie, R. Twist, S.G. Spruytte, F. Reinhardt, I.C. Kizilyalli, and G.S. Higashi. 27.6% Conversion efficiency, a new record for single-junction solar cells under 1 sun illumination. In *2011 37th IEEE Photovoltaic Specialists Conference (PVSC)*, pages 000004–000008, 2011.

[5] L. Esaki and R. Tsu. Superlattice and negative differential conductivity in semiconductors. *IBM Journal of Research and Development*, 14(1):61–65, January 1970.

[6] C. Goradia, R. Clark, and D. Brinker. A proposed GaAs-based superlattice solar cell structure with high efficiency and high radiation tolerance. In *18th IEEE PVSC*, pages 776–781, Las Vegas, NV, 1985. IEEE.

[7] M. A. Slocum, D. V. Forbes, and S. M. Hubbard. Subbandgap current collection through the implementation of a doping superlattice solar cell. *Applied Physics Letters*, 101(7):073901–1–073901–4, 2012.

[8] M.A. Slocum, D.V. Forbes, P. Roland, R. Ellingson, and S.M. Hubbard. Characterization of a quantum dot nipi photovoltaic device. In *38th IEEE PVSC*, pages 002970 –002975, 2012.

[9] G. H. Döhler. Electron states in crystals with “nipi-superstructure”. *physica status solidi (b)*, 52(1):79–92, 1972.

[10] G. H. Döhler, H. Kunzel, D. Olego, K. Ploog, P. Ruden, H. J. Stolz, and G. Abstreiter. Observation of tunable band gap and two-dimensional subbands in a novel GaAs superlattice. *Physical Review Letters*, 47(12):864–867, 1981.

[11] G. H. Döhler and P. R. Ruden. Theory of absorption in doping superlattices. *Physical Review B*, 30(10):5932–5944, November 1984.

[12] K. Ploog and G. H. Döhler. Compositional and doping superlattices in III-V semiconductors. *Advances in Physics*, 32(3):285–359, 1983.

[13] G. Hasnain, C. J. Chang-Hasnain, G. H. DöHler, N. M. Johnson, D. Mars, J. N. Miller, and J. Whinnery. High quality selective contacts to n-i-p-i doping superlattices. *Le Journal de Physique Colloques*, 48(C5):C5–605–C5–609, November 1987.

[14] C. D. Cress, S. J. Polly, S. M. Hubbard, R. P. Raffaelle, and R. J. Walters. Demonstration of a nipi-diode photovoltaic. *Progress in Photovoltaics: Research and Applications*, 19(5):552–559, 2011.

[15] R. Clark, C. Goradia, and D. Brinker. Dependence of lifetime on design parameters of an nipi doping superlattice: Results of self-consistent calculations. *Superlattices and Microstructures*, 4:187–193, 1988.

[16] Fraunhofer ISE. New world record for solar cell efficiency at 46% (accessed at http://www.ise.fraunhofer.de/en/press-and-media/press-releases/press-releases-2014/new-world-record-for-solar-cell-efficiency-at-46-percent), 2014.

[17] A. W Bett. Multijunction concentrator solar cells. In A. L Luque and V. M Andreev, editors, *Concentrator Photovoltaics*, number 130 in Springer Series in Optical Sciences, pages 67–87. Springer Berlin Heidelberg, 2007.

[18] Sharp Corporation. Press release, (accessed at http://sharp-world.com/corporate/news/130614.html on 30 july 2013), 2013.

[19] J. F. Geisz, D. J. Friedman, J. S. Ward, A. Duda, W. J. Olavarria, T. E. Moriarty, J. T. Kiehl, M. J. Romero, A. G. Norman, and K. M. Jones. 40.8% efficient inverted triple-junction solar cell with two independently metamorphic junctions. *Applied Physics Letters*, 93:123505, 2008.

[20] W. Guter, J. Schone, S. P. Philipps, M. Steiner, G. Siefer, A. Wekkeli, E. Welser, E. Oliva, A. W. Bett, and F. Dimroth. Current-matched triple-junction solar cell reaching 41.1% conversion efficiency under concentrated sunlight. *Applied Physics Letters*, 94(22):223504–223504, 2009.

[21] R. R. King, D. Bhusari, A. Boca, D. Larrabee, X.-Q. Liu, W. Hong, C. M. Fetzer, D. C. Law, and N. H. Karam. Band gap-voltage offset and energy production in next-generation multijunction solar cells. *Progress in Photovoltaics: Research and Applications*, 19(7):797–812, 2011.

[22] A. Luque and A. Marti. Increasing the efficiency of ideal solar cells by photon induced transitions at intermediate levels. *Physical Review Letters*, 78:5014–5017, 1997. 26.

[23] Pablo G. Linares, Antonio Martí, Elisa Antolín, Corrie D. Farmer, Íñigo Ramiro, Colin R. Stanley, and Antonio Luque. Voltage recovery in intermediate band solar cells. *Solar Energy Materials and Solar Cells*, 98:240–244, 2012.

[24] M. Wolf. Limitations and possibilities for improvement of photovoltaic solar energy converters: Part i: Considerations for earth's surface operation. *Proceedings of the IRE*, 48(7):1246–1263, 1960.

[25] A. Martí, E. Antolín, P. García-Linares, I. Ramiro, I. Artacho, E. López, E. Hernández, M. J. Mendes, A. Mellor, I. Tobías, D. Fuertes Marrón, C. Tablero, A. B. Cristóbal, C. G. Bailey, M. Gonzalez, M. Yakes, M. P. Lumb, R. Walters, and A. Luque. Six not so easy pieces in intermediate band solar cell research. In *Proc. SPIE 8620*, volume 8620, pages 86200J–86200J–11, 2013.

[26] R. Strandberg and T. W. Reenaas. Photofilling of intermediate bands. *Journal of Applied Physics*, 105(12):124512–124512, 2009.

[27] C. G. Bailey, D. V. Forbes, R. P. Raffaelle, and S. M. Hubbard. Near 1 V open circuit voltage InAs/GaAs quantum dot solar cells. *Applied Physics Letters*, 98:163105, 2011.

[28] S. M. Hubbard, C. D. Cress, C. G. Bailey, R. P. Raffaelle, S. G. Bailey, and D. M. Wilt. Effect of strain compensation on quantum dot enhanced GaAs solar cells. *Appl. Phys. Lett.*, 92, 2008. 12.

[29] Christopher G. Bailey, David V. Forbes, Ryne P. Raffaelle, and Seth M. Hubbard. Investigation of spectral responsivity of InAs QD-embedded GaAs solar cells. In *Proc. SPIE 7933*, volume 7933, pages 793313–793313–7, 2011.

[30] C. G. Bailey, D. V. Forbes, S. J. Polly, Z. S. Bittner, Y. Dai, C. Mackos, R. P. Raffaelle, and S. M. Hubbard. Open-circuit voltage improvement of InAs/GaAs quantum-dot solar cells using reduced InAs coverage. *IEEE Journal of Photovoltaics*, 2(3):269–275, 2012.

[31] K.S. Krane. *Introductory Nuclear Physics*. John Wiley & Sons, New York, 1988.

[32] G. B. Stringfellow. *Organometallic Vapor-Phase Epitaxy*. Academic Press, 2nd edition, 1998.

[33] K. Byrappa and T. Ohachi. *Crystal growth technology*. William Andrew Pub. ; Springer, 2003.

[34] H. Ando, H. Iwamura, H. Oohashi, and H. Kanbe. Nonlinear absorption in n-i-p-i-MQW structures. *Quantum Electronics, IEEE Journal of*, 25(10):2135 –2141, 1989.

[35] H. Kobayashi, Y. Yamauchi, and H. Ando. Nonlinear optical absorption in an nInGaAsP/pInP heterodoping superlattice. *Applied Physics Letters*, 52(5):359–361, 1988.

[36] Alan R. Kost, Ron R. Carter, Elsa M. Garmire, and Thomas C. Hasenberg. Nonlinear optical properties of a hetero-nipi structure with coupled quantum wells. *Journal of Nonlinear Optical Physics & Materials*, 14(03):449–460, 2005.

[37] AE/AP trapped particle flux maps 1966-1980. *http://modelweb.gsfc.nasa.gov/magnetos/aeap.html*, Last accessed 8/19/2013.

[38] M. Yamaguchi, A. Khan, S.J. Taylor, M. Imaizumi, T. Hisamatsu, and S. Matsuda. A detailed model to improve the radiation-resistance of Si space solar cells. *IEEE Transactions on Electron Devices*, 46:2133–2138, 1999.

[39] KSA Butcher, D Alexiev, and TL Tansley. Minority carrier diffusion lengths for high purity liquid phase epitaxial GaAs. *Australian Journal of Physics*, 46(2):317–326, 1993.

[40] S. R Messenger, E. M Jackson, E. A Burke, R. J Walters, M. A Xapsos, and G. P Summers. Structural changes in InP/Si solar cells following irradiation with protons to very high fluences. *Journal of Applied Physics*, 86(3):1230–1235, 1999.

[41] G. H. Döhler. n-i-p-i doping superlattices—metastable semiconductors with tunable properties. *Journal of Vacuum Science & Technology B: Microelectronics and Nanometer Structures*, 1:278–284, 1983.

[42] W. Rehm, H. Kunzel, G. H. Döhler, K. Ploog, and P. Ruden. Time resolved luminescence in n-i-p-i doping superlattices. *Physica B+C*, 117-118, Part 2:732–734, March 1983.

[43] G. H. Döhler, H. Kunzel, and K. Ploog. Tunable absorption coefficient in GaAs doping superlattices. *Physical Review B*, 25(4):2616–2626, 1982.

[44] Synopsys sentaurus. *http://www.synopsys.com/Tools/TCAD/Solutions/Pages/default.aspx*, Last accessed 8/20/2013.

[45] M. E. Levinshteĭn, S. L Rumyantsev, and Michael Shur. *Handbook series on semiconductor parameters*, volume 1. World Scientific, Singapore, 1996.

[46] I. Garcia, I. Rey-Stolle, C. Algora, W. Stolz, and K. Volz. Influence of GaInP ordering on the electronic quality of concentrator solar cells. *Journal of Crystal Growth*, 310(23):5209–5213, 2008.

[47] D.E. Aspnes. Recombination at semiconductor surfaces and interfaces. *Surface Science*, 132(1–3):406–421, 1983.

[48] D. S. L. Mui, T. A. Strand, B. J. Thibeault, L. A. Coldren, P. M. Petroff, and E. L. Hu. Characteristics of insitu cl2 etched/regrown GaAs/GaAs interfaces. *Journal of Vacuum Science & Technology B*, 11(6):2266–2269, 1993.

[49] Chih-Tang Sah, R.N. Noyce, and W. Shockley. Carrier generation and recombination in p-n junctions and p-n junction characteristics. *Proceedings of the IRE*, 45(9):1228 –1243, 1957.

[50] S. C. Choo. Carrier generation-recombination in the space-charge region of an asymmetrical p-n junction. *Solid-State Electronics*, 11(11):1069–1077, 1968.

[51] W. Shockley and W. T. Read. Statistics of the recombinations of holes and electrons. *Physical Review*, 87(5):835–842, 1952.

[52] J. S. Blakemore. *Semiconductor Statistics*. Pergamon Press, 1962.

[53] D. Brancus and V. Dolocan. On the carrier generation-recombination in the space-charge region of a p-n junction. *International Journal of Electronics*, 32(2):137–146, 1972.

[54] S. Mazzucato, B. Royall, R. Ketlhwaafetse, N. Balkan, J. Salmi, J. Puustinen, M. Guina, A. Smith, and R. Gwilliam. Dilute nitride and GaAs n-i-p-i solar cells. *Nanoscale Research Letters*, 7(1):631, 2012.

[55] G. H Döhler, G. Hasnain, and J. N Miller. In situ grown-in selective contacts to n-i-p-i doping superlattice crystals using molecular beam epitaxial growth through a shadow mask. *Applied Physics Letters*, 49(12):704–706, 1986.

[56] S.J. Pearton. Ion implantation for isolation of III-V semiconductors. *Materials Science Reports*, 4(6):313–363, 1990.

[57] R. Williams. *Modern GaAs processing methods*. Artech House, Boston, 1990.

[58] K. Yamaguchi, K. Okamoto, and T. Imai. Selective epitaxial-growth of GaAs by metalorganic vapor deposition. *Jpn. J. Appl. Phs.*, 24:1666–1671, 1985.

[59] Rajaram Bhat. Current status of selective area epitaxy by OMCVD. *Journal of Crystal Growth*, 120(1–4):362–368, 1992.

[60] D. M. Hansen. An AFM study of $\mathrm{Si_xN_y}$ vs $\mathrm{SiO_2}$ selective growth barriers, 2009.

[61] N. Arnold, R. Schmitt, and K. Heime. Diffusion in III-V semiconductors from spin-on-film sources. *Journal of Physics D: Applied Physics*, 17(3):443–474, 1984.

[62] Y. I. Nissim, J. F. Gibbons, and R. B. Gold. Nonalloyed ohmic contacts to n-GaAs by CW laser-assisted diffusion from a $\mathrm{SnO_2/SiO_2}$ source. *Electron Devices, IEEE Transactions on*, 28(5):607–609, 1981.

[63] R. Jett Field and Sorab K. Ghandhi. An Open-Tube method for diffusion of zinc into GaAs. *Journal of The Electrochemical Society*, 129(7):1567–1570, 1982.

[64] B. W. Liang and C. W. Tu. A study of group-V desorption from GaAs and GaP by reflection high-energy electron diffraction in gas-source molecular beam epitaxy. *Journal of Applied Physics*, 72(7):2806–2809, 1992.

[65] Tatsuya Takamoto, Masafumi Yumaguchi, Eiji Ikeda, Takaaki Agui, Hiroshi Kurita, and Mowafak Al-Jassim. Mechanism of zn and si diffusion from a highly doped tunnel junction for InGaP/GaAs tandem solar cells. *Journal of Applied Physics*, 85(3):1481–1486, 1999.

[66] S. G. Ayling, A. C. Bryce, I. Gontijo, J. H. Marsh, and J. S. Roberts. A comparison of carbon and zinc doping in GaAs/AlGaAs lasers bandgap-tuned by impurity-free vacancy disordering. *Semiconductor Science and Technology*, 9(11):2149, 1994.

[67] S. Sze and K. Ng. *Physics of semiconductor devices*. John Wiley and Sons, 3rd edition, October 2006.

[68] J. Nishizawa. Stoichiometry control and point defects in compound semiconductors. *Mater. Chem. Phys.*, 64:93–115, 2000. 2.

[69] N. Furuhata and Y. Shiraishi. Improvement in electrical properties at an n-GaAs/n-GaAs regrown interface using ammonium sulfide treatment. *Jpn. J. Appl. Phys.*, 37:10–14, 1998.

[70] R. M. Lammert, T. M. Cockerill, D. V. Forbes, G. M. Smith, and J. J. Coleman. Submilliampere threshold buried-heterostructure InGaAs/GaAs single-quantum-well lasers grown by selective-area epitaxy. *IEEE Photonic Tech. L.*, 6:1073–1075, 1994.

[71] K. D. Jöns, P. Atkinson, M. Müller, M. Heldmaier, S. M. Ulrich, O. G. Schmidt, and P. Michler. Triggered indistinguishable single photons with narrow line widths from site-controlled quantum dots. *Nano Letters*, 13(1):126–130, 2013.

[72] D. Biswas, P. R. Berger, U. Das, J. E. Oh, and P. K. Bhattacharya. Investigation of the interface region produced by molecular beam epitaxial regrowth. *Journal of Electronic Materials*, 18(2):137–142, 1989.

[73] Shunro Fuek, Masasi Umemura, Naoshi Yamada, Kazuhiro Kuwahara, and Tetsuji Imai. Morphology of GaAs homoepitaxial layer grown on (111) a substrate planes by organometallic vapor phase deposition. *Journal of Applied Physics*, 68(1):97, 1990.

[74] Hsien-Chin Chiu, Yuan-Chang Huang, Chung-Wen Chen, and Liann-Be Chang. Electrical characteristics of passivated pseudomorphic HEMTs with pretreatment. *IEEE Transactions on Electron Devices*, 55(3):721–726, 2008.

[75] D.H. Reep and S.K. Ghandhi. Morphology of organometallic CVD grown GaAs epitaxial layers. *Journal of Crystal Growth*, 61(3):449–457, 1983.

[76] S. J. Bass and P. E. Oliver. Controlled doping of gallium arsenide produced by vapour epitaxy, using trimethylgallium and arsine. In *Institute of Physics Conference Series*, volume 33b, pages 1–10, 1977.

[77] H.Q. Hou, B.E. Hammons, and W.G. Breiland. In situ etching of GaAs by $AsCl_3$ for regrowth on AlGaAs in metalorganic vapor-phase epitaxy. *Journal of Crystal Growth*, 195(1-4):199–204, 1998.

[78] R. R. King, D. C. Law, K. M. Edmondson, C. M. Fetzer, G. S. Kinsey, H. Yoon, R. A. Sherif, and N. H. Karam. 40% efficient metamorphic GaInPGaInAsGe multijunction solar cells. *Appl. Phys. Lett.*, 90(18):183516, 2007.

[79] J. F. Kluender, A. M. Jones, R. M. Lammert, J. E. Baker, and J. J. Coleman. Growth, characterization and modeling of $\mathrm{in_x ga_{1\text{-}x} p}$ stripes by selective-area MOCVD. *Journal of Electronic Materials*, 25:1514–1520, 1996.

[80] E. Antolin, A. Marti, P. G. Linares, I. Ramiro, E. Hernández, C.D. Farmer, C.R. Stanley, and A. Luque. Advances in quantum dot intermediate band solar cells. In *2010 35th IEEE Photovoltaic Specialists Conference (PVSC)*, pages 000065–000070, 2010.

[81] A. Luque, A. Martí, N. Lopez, E. Antolin, E. Cánovas, C. Stanley, C. Farmer, L. J. Caballero, L. Cuadra, and J. L. Balenzategui. Experimental analysis of the quasi-fermi level split in quantum dot intermediate-band solar cells. *Applied Physics Letters*, 87(8):083505–083505, 2005.

[82] Antonio Martí, E. Antolín, P. G. Linares, and A. Luque. Understanding experimental characterization of intermediate band solar cells. *Journal of Materials Chemistry*, 22(43):22832–22839, 2012.

[83] M. Sugiyama, Y. Wang, K. Watanabe, T. Morioka, Y. Okada, and Y. Nakano. Photocurrent generation by two-step photon absorption with quantum-well superlattice cell. *IEEE Journal of Photovoltaics*, 2(3):298 –302, 2012.

[84] A. Marti, L. Cuadra, and A. Luque. Partial filling of a quantum dot intermediate band for solar cells. *IEEE Transactions on Electron Devices*, 48(10):2394–2399, 2001.

[85] D. A. B. Miller, D. S. Chemla, T. C. Damen, A. C. Gossard, W. Wiegmann, T. H. Wood, and C. A. Burrus. Electric field dependence of optical absorption near the band gap of quantum-well structures. *Physical Review B*, 32(2):1043–1060, 1985.

[86] S. Li and J. Xia. Quantum-confined stark effects of InAs/GaAs self-assembled quantum dot. *Journal of Applied Physics*, 88(12):7171–7174, December 2000.

[87] E. Antolín, A. Martí, C. D Farmer, P. G Linares, E. Hernández, A. M Sánchez, T. Ben, S. I Molina, C. R Stanley, and A. Luque. Reducing carrier escape in the InAs/GaAs quantum dot intermediate band solar cell. *Journal of Applied Physics*, 108(6):064513–064513–7, 2010.

[88] F. Y. Tsai and C. P. Lee. InGaAs/GaAs quantum dots on (111)B GaAs substrates. *Journal of Applied Physics*, 84(5):2624–2627, September 1998.

[89] C. M. A. Kapteyn, F. Heinrichsdorff, O. Stier, R. Heitz, M. Grundmann, N. D. Zakharov, D. Bimberg, and P. Werner. Electron escape from InAs quantum dots. *Physical Review B*, 60(20):14265–14268, 1999.

[90] X. L Zhou, Y. H Chen, H. Y Zhang, G. Y Zhou, T. F Li, J. Q Liu, X. L Ye, Bo Xu, and Z. G Wang. Carrier tunneling effects on the temperature dependent photoluminescence of InAs/GaAs quantum dot: Simulation and experiment. *Journal of Applied Physics*, 109(8):083501–083501–7, 2011.

[91] M. Colocci, A. Vinattieri, L. Lippi, F. Bogani, M. Rosa-Clot, S. Taddei, A. Bosacchi, S. Franchi, and P. Frigeri. Controlled tuning of the radiative lifetime in InAs self-assembled quantum dots through vertical ordering. *Applied Physics Letters*, 74(4):564–566, 1999.

[92] F. Adler, M. Geiger, A. Bauknecht, F. Scholz, H. Schweizer, M. H. Pilkuhn, B. Ohnesorge, and A. Forchel. Optical transitions and carrier relaxation in self assembled InAs/GaAs quantum dots. *Journal of Applied Physics*, 80(7):4019–4026, 1996.

[93] R. Heitz, A. Kalburge, Q. Xie, M. Grundmann, P. Chen, A. Hoffmann, A. Madhukar, and D. Bimberg. Excited states and energy relaxation in stacked InAs/GaAs quantum dots. *Phys. Rev. B*, 57(15):9050–9060, 1998.

[94] H. J. Polland, L. Schultheis, J. Kuhl, E. O. Göbel, and C. W. Tu. Lifetime enhancement of two-dimensional excitons by the quantum-confined stark effect. *Physical Review Letters*, 55(23):2610–2613, December 1985.

[95] P Harrison. *Wiley: Quantum Wells, Wires and Dots: Theoretical and Computational Physics of Semiconductor Nanostructures*. Wiley-Interscience, 3rd edition, 2010.

[96] A. Alemu and A. Freundlich. Improving photo-generated carrier escape in quantum well solar cells. In *Proc. SPIE 8256*, volume 8256, pages 82560B–82560B–7, 2012.

[97] B. E. Anspaugh. GaAs Solar Cell Radiation Handbook. Technical report, NASA, 1996.

[98] H. Y. Tada, J. R. Carter, B. E. Anspaugh, and R. G. Downing. Solar cell radiation handbook. Technical report, NASA, 1982.

[99] S. Sato, T. Ohshima, and M. Imaizumi. Modeling of degradation behavior of InGaP/GaAs/Ge triple-junction space solar cell exposed to charged particles. *Journal of Applied Physics*, 105:044504, 2009.